A Study of the Top Quark Production Threshold at a Future Electron-Positron Linear Collider

Filimon Gournaris

Department of Physics and Astronomy
University College London

A thesis submitted for the degree of Doctor of Philosophy
of University College London

September 2009

DECLARATION

I confirm that the work presented in this Thesis is my own. Where information has been derived from other sources, I confirm that it has been indicated in the document.

Filimon Gournaris

Αφιερωμὲνο στη μητὲρα μου.

"The mystery of the scientist is the same as the mystery of the artist.
So is the misery..."
Jean-Luc Godard

Abstract

One of the most important physics targets for any future electron positron linear collider will be the precision measurements of the top quark properties, and especially the top quark mass. Top-antitop production at threshold provides the ideal environment for making such measurements but is complicated by the machine's luminosity spectrum and thus needs to be carefully studied to understand the constraints involved and the potential precision reach. This thesis presents developments in both the understanding of the luminosity spectrum and the top quark production threshold by the means of new simulation tools and simulation results of systematic and statistical uncertainties in the measurements of the luminosity spectrum and the top quark parameters by the use of a threshold scan.

The luminosity spectrum is studied by employing a new parametrization method that takes into account the beam energy spread in the fit parameters, and detailed simulation studies of the measurement of the luminosity spectrum by the use of Bhabha scattering events. A detailed account is given of the possible systematic uncertainties arising due to beam-beam and detector induced effects influencing the luminosity measurement, by looking at the different luminosity spectra of the International Linear Collider (ILC) Reference Design Report (RDR) accelerator parameter plane.

A new simulation tool for the top quark production threshold is presented, in the form of a new fully differential Monte Carlo event generator using a state-of-the-art next-to-next-to leading order (NNLO) QCD calculation of the top quark production threshold in order to describe the total and differential distributions that can be used in the top threshold measurements, by including a full description of the luminosity spectrum.

Finally, a study of how the uncertainties of the luminosity spectrum measurement can affect the top quark threshold measurements is presented, by examining simulated threshold scan measurements for the different luminosity spectra of the ILC RDR accelerator parameter plane.

Acknowledgements

Unlike most other thesis, the people who actively helped me in the science aspect of this thesis were very few, and especially in this last year, I would say, none. However, the people who helped me shape my views on physics (computing, and.. drinking activities therein) are numerous, and so I will try to do justice and mention as many of them as I can (and I apologise apriori for the ones I forgot).

First of all I would like to thank the UCL HEP group for their hospitality over the years, for putting up with both my uber excitement and extreme misery (according to circumstance), and for being the best (and coolest) place I know so far for doing particle physics.

I would like to thank Matthew Wing for always being willingly available to help with any issue I had in the best way he could, for all the funding he found for me over the years (such that I didn't starve while trying to do this thesis), for reading this manuscript over and over, and for giving me the final corrections in a very fast and professional way.

I would also like to thank Mark Lancaster, for being such a briliant and cool physicist that he is, and for always supporting me, in the pub and at his office.

Stewart Boogert's contribution to this thesis must also be mentioned, since he was the initiator of the various projects that I dealt with over the years, and most of the ideas therein, and for that I thank him. I would also like to thank David Miller, for taking me as a project student, and for introducing me to the world of the ILC.

In the work aspect of this thesis, Thomas Teubner and Philip Bambade must be mentioned. Thomas for providing me with his `TOPPIK` code, and for many discussions of the internal workings of the code and general theoretical aspects of this work, and Philip for his kind hospitality during a briliant and very productive month I spent in Paris, for showing me how physics should be done, and for offering me a job afterwards, eventhough it didn't work out at the end.

Also, I feel I should mention the names of Dr. Statiris and Dr. Tsokos, who were my physics teachers at school, and who triggered my curiosity about the weird world of physics in the first place.

I made many good friends while exploring this weird world of physics, and so, just to mention a few, I would like to thank Bino for being the 'Chuck' that he is, Sarah `sboutle` for all the nice times we had in London and Hamburg, and for hanging around to submit (almost) as late as I did, Lily for being wild but briliant, JohnL for being the best soul out there, and all the rest of the people I spent time with while at UCL, LAL, SLAC and other assorted physics travels.

Alexey Lyapin definately deserves a mention here, for liking coffee breaks as much as I do, for always being a good friend, and for always trying to support me with clear thought, in the good times and (most importantly) in the bad...

Since there is also life outside of the physics bubble, I would like to thank some old (and new) non-physics friends who helped me stay sane during my physics adventures. Luca for being a really good friend and for always joining me in the various impulsive ideas that I have from time to time, George for following parallel paths with me for the past 10 years, Doreta and Iraklis for making my troubled times in London to be fun, Joanna for putting up with me for a year at good old Brixton and for loving to talk about civil engineering (and pretty much everything else), and some more recent friends like the crowd at 113 and Elena Theou, for helping me realize that London is not that bad after all.

For my newest best friend, Zoe, I would like to say that after what we have been through together over the last few months, there is no limit to what we can do... Thank you for making me smile everyday!

Finally, and most importantly, I would like to thank my mother, to whom this thesis is dedicated to, for raising me the way she did, and for always believing in me and always supporting me, no matter what...

Filimon Gournaris

Contents

1. Introduction **10**

2. Motivation **12**

2.1 The Standard Model of Particle Physics 12

2.1.1 Overview of the Standard Model 12

2.1.2 Problems with the Standard Model 15

2.1.3 Beyond the Standard Model 17

2.2 The Top Quark in the Standard Model 18

2.3 The Top Quark Beyond the Standard Model 21

2.4 Motivation for a Linear Collider 22

2.5 The Top Quark at a Linear Collider 25

2.5.1 Threshold Scan 26

2.5.2 Direct Reconstruction in the Continuum 27

3. The International Linear Collider **28**

3.1 The Accelerator 28

3.1.1 Particle Sources 30

3.1.2 Damping Rings 30

3.1.3 Main Linac 30

3.1.4 Beam Delivery System 31

3.1.5 Interaction Region 31

3.1.6 Extraction Line 32

3.1.7 Operational Parameter Plane 32

3.1.8 Alternative Projects: CLIC 33

3.2 The Detector(s) 34

3.2.1 Detector Requirements 34

3.2.2 Detector Concepts 36

4. The Luminosity Spectrum **39**
4.1 Luminosity . . . 40
4.1.1 Measuring the Luminosity: LumiCal . . . 41
4.2 Absolute Beam Energy . . . 43
4.2.1 Measuring the Beam Energy: Energy Spectrometer . . . 43
4.2.2 Measuring the Beam Energy: Other Methods . . . 45
4.3 Luminosity Spectrum Explained . . . 45
4.3.1 Simulating the Luminosity Spectrum . . . 47
4.3.2 Beamstrahlung Parameterization and Fitting . . . 50
4.4 Measuring the Luminosity Spectrum . . . 53
4.4.1 Bhabha Scattering . . . 53
4.4.2 Simulation Method . . . 56
4.5 Luminosity Spectrum Measurement Systematics . . . 61
4.5.1 Detector Resolution Effects . . . 61
4.5.2 Beam-Beam Effects . . . 63
4.5.3 Conclusion . . . 70
4.6 Summary . . . 72

5. The Top Quark Threshold **73**
5.1 Introduction . . . 73
5.2 Green Functions, Cross-Sections and Distributions . . . 74
5.2.1 Non-Relativistic QCD . . . 75
5.2.2 Green Functions and the Schrödinger Equation . . . 77
5.2.3 Total Cross-Section and Momentum Distributions . . . 79
5.2.4 Mass Definition . . . 81
5.2.5 Numerical Implementation: `TOPPIK` . . . 82
5.3 Observables at the $t\bar{t}$ Threshold . . . 83
5.4 Luminosity Spectrum Effects . . . 88
5.5 Summary . . . 90

6. Monte Carlo Event Generator for $t\bar{t}$ Production at Threshold **91**
6.1 Introduction . . . 91
6.2 The Monte Carlo Method . . . 92
6.3 Existing Generators . . . 94
6.4 A New $t\bar{t}$ Threshold Generator : `ttbarMC` . . . 95
6.4.1 Generator Layout : Using `TOPPIK` . . . 95
6.4.2 Interpolation . . . 97

6.4.3 Phase Space Integration . . . 101
6.4.4 Generation Kinematics . . . 103
6.4.5 Parton Level Comparison with TOPPIK Calculations . . . 109
6.5 ttbarMC Interface to Hadronization . . . 110
6.5.1 $t\bar{t}$ Decay Channels . . . 110
6.5.2 Interface to Pythia . . . 113
6.5.3 Hadron Level Events . . . 113
6.6 Summary . . . 115

7. Measurement of Top Quark Properties by a Threshold Scan 117
7.1 Observables and Multi-Parameter Fits . . . 118
7.1.1 Threshold Scan . . . 119
7.1.2 $\sigma_{tot}^{t\bar{t}}$ Lineshape . . . 119
7.1.3 P_{peak} and A_{FB} . . . 122
7.2 Impact of the Luminosity Spectrum on the $t\bar{t}$ Threshold Measurements . 124
7.2.1 Statistical Uncertainty on M_t and α_s . . . 126
7.2.2 Systematic Shifts on M_t and α_s . . . 128
7.3 Summary . . . 130

8. Summary and Outlook 131

List of Figures 134

List of Tables 139

References 142

Chapter 1

Introduction

Most discoveries in particle physics over the last half century, leading to what is now widely accepted as the underlying theory of subatomic particles, the Standard Model of particle physics, were primarily based in laboratory experiments using accelerators. The experience gained in these last 50 or so years of experimentation has also shown that the complementarity of using both hadron and lepton colliders in accelerator experiments is fundamental for a better understanding of the experiments themselves, and the theories they are intended to test.

In such a manner, the International Linear Collider (ILC) project is the natural progression of the field of collider particle physics after the currently built Large Hadron Collider (LHC) experiment at the CERN laboratory near Geneva. One of the important questions that the ILC will be used to answer, is the precise nature of the top quark, nature's heaviest observed fundamental particle. The top quark is also the least well measured fundamental particle in the Standard Model, with many theories implying that a better undestanding of the top quark properties could shed light on some of the current open questions in particle physics.

The purpose of this thesis is to examine the feasibility of making precise measurements of the top quark properties at the ILC by using the method of a threshold scan. In the top quark threshold scan at the ILC, one of the most important sources of experimental uncertainties is thought to come from the collider's luminosity spectrum. Hence, in this context, the feasibility and mechanics of the top quark measurements are mainly examined in the context of the machine's luminosity spectrum.

The organization of this thesis is the following:

In **Chapter 2**, a brief description of the theoretical framework of the Standard Model of particle physics is given, together with an outline of its problems and possible

extensions. Then the top quark is described in the context of the Standard Model, with a focus on how the top quark measurements can act as a motivation for a linear collider. **Chapter 3** acts as an introduction to the ILC project, describing most of its important accelerator components, and the various possibilities for its detectors.

In **Chapter 4**, the concepts of energy and luminosity are discussed, and a detailed description of the luminosity spectrum at a linear collider is given. A method for the parametrization of the luminosity spectrum is developed, and expanding on the work of (Mönig, 2000) where Bhabha events are used, a more detailed study of the measurement of the luminosity spectrum is performed, including many of the possible systematic effects that could influence its accuracy.

In the first part of **Chapter 5**, an introduction to the theoretical framework behind the top quark threshold is given (following the work of Hoang and Teubner, 1999), outlining the complicated QCD dynamics and the challenges of the theoretical calculation. The second part of the chapter looks at the numerical implementation of the QCD calculation, the behaviour of the main top quark observables at the threshold region, and describes the challenge of including the luminosity spectrum in the threshold simulation.

Chapter 6 discusses the shortcomings of existing Monte Carlo event generators in describing the complicated QCD dynamics of the top quark threshold, and presents a new event generator, based on the calculations of (Hoang and Teubner, 1999) described in Chapter 5, specifically written for the top quark production threshold. It presents a detailed description of the generation process, from the basics of using the numerical calculations of (Hoang and Teubner, 1999) to the inclusion of the luminosity spectrum in the phase space integration, the details of the kinematics used, and the interface to the hadronization machinery of `Pythia` for arriving at hadron level events.

The next chapter, **Chapter 7**, looks in more detail at the details of the top quark measurement by a threshold scan, by discussing how the different observables can be used in multiparameter fits in order to extract the top quark parameters from the threshold scan. The new event generator described in Chapter 6 is used to simulate the threshold, together with the results of Chapter 4 on the measurement of the luminosity spectrum, in order to give an estimate of the possible uncertainties of the threshold observables arising from the uncertainties in the luminosity spectrum.

Finally, **Chapter 8** summarizes the work of this thesis, by looking at the conclusions of each chapter, and outlines the future directions for a complete analysis of the top quark threshold, based on the machinery developed in this work.

Chapter 2

Motivation

2.1 The Standard Model of Particle Physics

2.1.1 Overview of the Standard Model

The Standard Model (SM) of particle physics is our most successful theory to date describing nature at its most fundamental level, the elementary particles and their interactions [1]. Formed mainly in the 1960's and 1970's, it gives a consistent and well verified description of three of the four fundamental forces of nature, namely the electromagnetic, the weak and the strong nuclear force, and their interaction with matter particles.

The particle content of the SM can be divided in two categories, spin-$\frac{1}{2}$ particles called fermions, which make up all of the visible matter in the universe, and spin-1 particles, called bosons, which are the force carriers for the fundamental interactions of nature. The fermions, consisting of leptons and quarks, are divided into three generations of increasing mass, with each generation consisting of two leptons and two quarks. The particle content of the SM is depicted in figure 2.1. A detailed description of all fundamental particles and their properties can be found in [2].

The fermions of the first generation, the electron and up and down quarks, suffice to explain all ordinary matter that we experience in every day life. There are however two further generations of fermions, with similar properties and interactions, that mainly differ in their mass. The fermions of the second and third generations are unstable and eventually decay into those from the first generation.

Each generation of fermions consists of a charged lepton and a neutral neutrino, and two quarks. Until recently the neutrino was thought to be massless, but recent

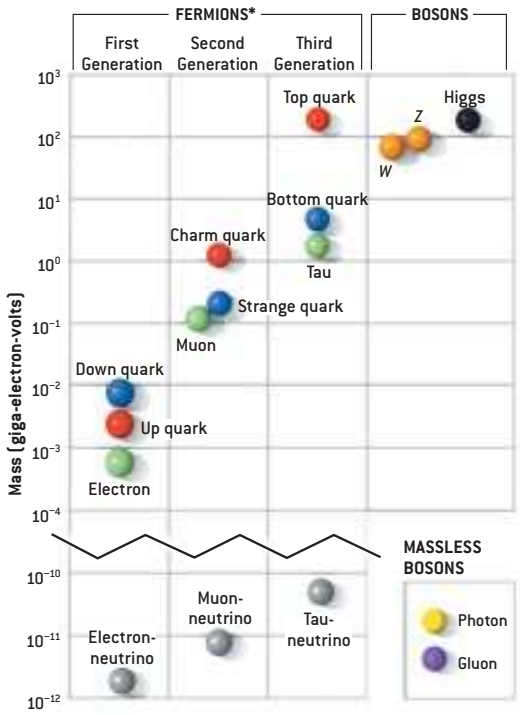

Figure 2.1: Diagram [3] of the SM fermions (divided into the three generations) and bosons, with the Higgs particle being the only particle yet to be discovered. The masses of the neutrinos are upper limits.

experiments indicated that the neutrino must have (albeit very small) mass [4, 5].

Leptons can be distinguished from quarks mainly in two ways. Firstly, leptons carry integer electric charge while quarks carry fractional charge, and secondly the quarks are the only fermions that experience the strong nuclear force (see below), which results from them having an additional quantum number, known as colour charge.

The same properties hold for the counter-parts of the fermions, their antiparticles, which differ only in some of their quantum numbers like the electric charge.

The interactions between the fermions in the SM are explained through the existence of the force carrying particles, the gauge bosons. In quantum field theory (QFT), the mathematical formulation of the SM, the interactions between different particles (fields) are derived under the principle of local gauge invariance. The SM Lagrangian, which contains all the dynamics of the theory, must preserve the symmetry structure of the gauge group $\mathrm{SU}(3)_C \times \mathrm{SU}(2)_L \times \mathrm{U}(1)_Y$, the underlying internal symmetry that essentially defines the SM. The symmetry group $\mathrm{SU}(3)_C$ is the gauge group defining the underlying properties of Quantum Chromodynamics (QCD), the theory of the strong interactions, while the symmetry group $\mathrm{SU}(2)_L \times \mathrm{U}(1)_Y$ defines the structure of the electroweak theory, also known as Glashow-Weinberg-Salam theory

[6], that provides a unified description of the electromagnetic and weak interactions.

Under this symmetry structure, the fundamental forces of the SM are described by the couplings of the gauge bosons to matter particles (and in some cases, to each other). The electromagnetic force is mediated by the photon γ, which couples to particles with electric charge. The weak force is mediated by the charged $W^{\pm}$ and the neutral Z bosons, which couple to all matter particles and to each other, and the strong nuclear force is mediated by the gluon. Similar to the photon, which couples to particles carrying electric charge, the gluon couples to particles carrying colour charge, but unlike the photon, which is electrically neutral, gluons carry colour charge themselves, which means that they can couple to each other. This leads to some unique properties of the strong interaction. Two such properties, that distinguishes the strong interaction from the other two fundamental forces of the SM, are the properties of asymptotic freedom and colour confinement.

Asymptotic freedom is the property of QCD in which the strength of the interaction between coloured particles becomes weaker at short distances, and stronger at long distances, i.e. the strength of the interaction scales asymptotically with distance. This leads to some interesting properties of coloured particles, such as the fact that at high energies (short distances), the quarks inside partons, like the proton and the neutron, can be treated as free particles.

Colour confinement leads to the fact that coloured objects cannot appear isolated in nature and hence cannot be directly observed in experiments. It is a consequence of both quarks and gluons carrying colour charge. Since the strong force is asymptotically free, when one tries to separate coloured objects from each other (e.g. separate a quark from its parent hadron, in analogy to an electron becoming unbound from a nucleus), a strong colour field consisting of gluons develops between them. As the distance between the coloured objects increases, the strength of the coloured field (also known as colour string) also increases, which makes it more energetically favourable for a quark anti-quark pair to be created out of the vacuum rather than the distance between the coloured objects to increase further. Through this process, known as hadronization or string fragmentation, coloured objects cannot be observed isolated in experiments, instead only clustered cascades of colour neutral particles (mesons and baryons) are observed, also known as jets. String fragmentation is one of the least well understood properties of QCD as it cannot be calculated explicitly, and hence one has to rely on phenomenological models of how the process unravels.

As a last fundamental feature of the SM, local gauge invariance requires that all the force carrying particles, the gauge bosons, are massless. However, a wealth of data from measurements of the $W^{\pm}$ and Z bosons, with the first made at CERN, show

that the force carriers of the weak interaction are actually rather massive. To solve this problem, an additional scalar field needs to be introduced, the Higgs field, which breaks the symmetry of the electroweak interaction and gives mass to the $W^{\pm}$ and Z bosons. This mechanism, known as the Higgs mechanism, leading to the spontaneous symmetry breaking of the electroweak interaction, requires that one more particle must exist, the Higgs boson [7].

Although it has been the subject of extensive searches at colliders, the Higgs boson has yet to be discovered. Recent experiments at the LEP collider gave a lower limit on its mass from direct searches to be $M_H \geq 114.4$ GeV [8]. The search for the Higgs boson is one of the main objectives of current and future collider experiments.

2.1.2 Problems with the Standard Model

Despite its many successes, the SM also has some problems in explaining the fundamental forces of nature, making it incomplete as a conclusive theory of the elementary particles and their interactions. The main open issues are [9] :

- **Origin of Mass**

  Within the SM, the origin of mass is explained through the Higgs mechanism. However, this has yet to be confirmed experimentally as the Higgs particle still remains undiscovered. For the SM to hold, the Higgs particle must be discovered and its properties must be confirmed to be those predicted by the theory.

  With the LHC experiments due to start taking data in 2009, the question about the existence of the Higgs should be settled soon. However, for precision measurements of all the Higgs properties, the experimental environment of the LHC could prove limiting, leading to the need for a high precision electron-positron linear collider (see section 2.4 and [10]).

- **Neutrino Masses**

  In the SM, because of lepton number conservation, the neutrinos are supposed to be massless. Recent experimental evidence [4, 5] show that neutrinos can oscillate by changing their flavour eigenstate. This leads to a mixing of the mass and flavour eigenstates implying that the neutrinos have mass. The question of how neutrinos acquire mass has not yet been answered conclusively.

- **Three Generations**

  Even though the description of fermionic matter in three generations, with the particles of each generation differing only in mass is very successful, there is no

satisfying explanation about the relationship of the three generations and their vastly different masses.

Furthermore, there is no clear explanation on the origin of the gauge group $\mathrm{SU}(3)_C \times \mathrm{SU}(2)_L \times \mathrm{U}(1)_Y$ and why the SM fermions occur as representations of this group.

- **Gravity**

  The SM, although successfully describing three of the four fundamental forces of nature, fails to incorporate gravity in its description. Currently there is no satisfactory way of combining the quantum field theory that the SM is based on with the theory of general relativity which is the best theory describing gravity.

  The unification of quantum mechanics with a theory of gravity is one of the major challenges of theoretical physics, seeking to provide a unified theory of the fundamental forces of nature.

- **Hierarchy Problem**

  The hierarchy problem of the SM arises from the question of why the weak force appears to be some 10^{32} times stronger than gravity, and is manifested for example in the huge separation between the scale of electroweak symmetry breaking $\mathcal{O}(10^2)$ GeV, and the Planck scale $\mathcal{O}(10^{19})$ GeV, at which quantum effects of gravity are expected to become important.

  Because the Higgs boson mass is so much lighter than the Planck mass, extensive fine-tuning (through renormalization) is required in SM calculations in order to cancel the very large radiative corrections to the Higgs bare mass and get sensible predictions.

  For the hierarchy problem to be solved, new physics must be present at the TeV energy scale [11].

- **Matter-Antimatter Asymmetry in the Early Universe**

  Current models of the Big Bang indicate that in the early Universe there existed equal amounts of matter and antimatter. The observable Universe however is made entirely of matter, indicating that there was a matter-antimatter asymmetry in the early Universe. The original matter and antimatter just after the Big Bang should have annihilated, leaving only photons in the background, but due to the matter-antimatter asymmetry one matter particle per billion or so must have survived, leading to what we see as matter in the observable Universe today.

This asymmetry can be explained through a property known as charge-parity ($\mathcal{CP}$) violation, which implies that the laws of nature are slightly different for a particle and its anti-particle.

Although $\mathcal{CP}$ violation is a well known property of the electroweak sector of the SM, and has been repeatedly measured in experiments [12, 13], the observed amount is not enough to explain the matter-antimatter asymmetry in the Universe, and hence a better explanation is needed.

- **Dark Matter and Dark Energy**

  The particles described by the SM can only explain 4% of the matter in the Universe. The remaining energy density, according to observations made with the WMAP mission [14] consists of about 73% of dark energy and 23% of dark matter. Dark matter does not interact with the electromagnetic force and hence its presence is implied through gravitational effects on ordinary matter [15]. Dark energy is a form of relic energy, hypothesized in order to explain the observations of an expanding Universe [16]. Currently there is no explanation for dark matter or dark energy within the SM.

2.1.3 Beyond the Standard Model

In an attempt to solve the problems outlined in the previous section, many theories have been proposed as extensions or alternatives to the SM, the most popular of which is Supersymmetry (SUSY).

In SUSY models, an additional symmetry is postulated between fermions and bosons, where each fermion has a bosonic supersymmetric partner and vice versa. SUSY also postulates that supersymmetric particles must be produced in pairs [17]. In this way, the lightest SUSY particle would provide a candidate for dark matter, the fine-tuning problem would be resolved through the cancellation of fermionic and bosonic contributions in loop corrections, and even gravity could be incorporated in some versions of SUSY models (e.g. Minimal Supergravity (mSUGRA) [18]).

The problem with SUSY models, is that they require a large number of additional free parameters in the theory, making the particle spectrum much more complicated than it already is. For example, SUSY in its most simple manifestation, the model called Minimal Supersymmetric Standard Model (MSSM), requires an extra 105 parameters in addition to those in the SM [17], compromising the elegance of the solution it offers.

There are many alternative theories to SUSY for physics beyond the SM, with

the most pronounced being theories of extra dimensions or string theories, trying to incorporate the effects of gravity in a theory that would eventually lead to what physicists call the Theory of Everything, a unified theory of all four fundamental forces of nature.

One of the most important goals of current and future experiments at particle colliders is to explore the TeV energy scale, verify or reject the proposed theories for physics beyond the SM, and gather the evidence required to guide theorists in the correct direction such that they will be able to compose what is being called the Theory of Everything.

2.2 The Top Quark in the Standard Model

The top quark is the heaviest elementary particle discovered so far. The latest direct measurements from the Tevatron collider at Fermilab give a world average for the top quark mass of [19]:

$$M_t = 172.4 \pm 1.2 \text{ GeV} \tag{2.1}$$

A summary plot of the latest top quark mass measurements can be seen in figure 2.2.

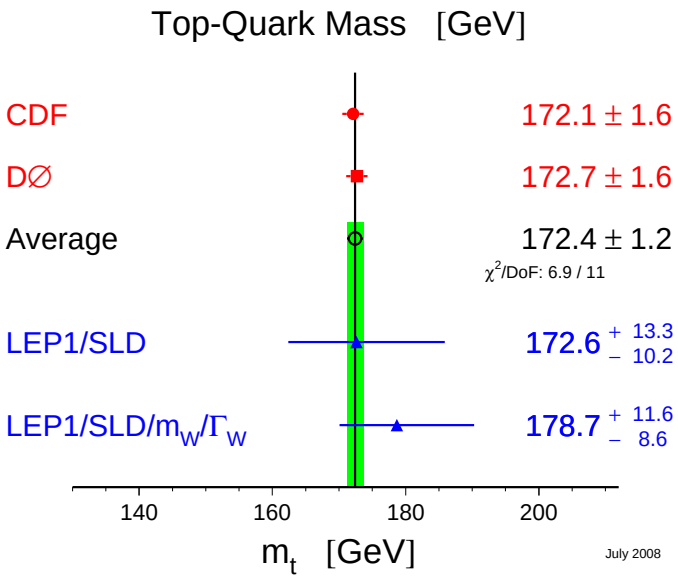

Figure 2.2: Summary plot of the latest measured values (July 2008) and the world average for the top quark mass [20].

Due to its very large mass, the top quark plays an important role in the SM, and especially in the electroweak sector since its mass is very near the electroweak symmetry breaking scale. Therefore, in many SM calculations the top quark mass enters as a parameter contributing to the radiative corrections of the calculations.

An example of this is the calculation of the W boson mass.

At tree level, the SM prediction for the W boson mass can be written as [21]

$$M_W^2 = \frac{\pi\alpha}{\sqrt{2}G_F \sin^2\theta_W} \tag{2.2}$$

where α is the fine structure constant, G_F is the Fermi constant, and θ_W is the Weinberg angle.

Now, the same expression including higher order corrections is given by

$$M_W^2 = \frac{\pi\alpha}{\sqrt{2}G_F \sin^2\theta_W} \cdot \frac{1}{1-\Delta r} \tag{2.3}$$

where Δr contains the contribution from radiative corrections.

The radiative corrections arising from the top quark are given by [21]

$$(\Delta r)_{\mathrm{t}} \approx -\frac{3G_F M_t^2}{8\sqrt{2}\pi^2} \cdot \frac{1}{\tan^2\theta_W} \tag{2.4}$$

where the dominant uncertainty in this expression comes from the top quark mass term, which has a quadratic contribution. The Feynman diagrams showing the contribution of the top quark to the W and Z boson mass can be seen in figure 2.3.

Figure 2.3: One-loop radiative corrections to the W and Z boson masses due to the top quark.

The Higgs boson also contributes to the calculation of the W boson mass via radiative corrections. The expression for the Higgs contribution is given by

$$(\Delta r)_H \approx \frac{11G_F M_Z^2 \cos^2\theta_W}{24\sqrt{2}\pi^2} \ln\left(\frac{M_H^2}{M_Z^2}\right) \tag{2.5}$$

where M_Z is the Z boson mass and M_H the Higgs mass. The Feynman diagrams showing the Higgs contribution can be seen in figure 2.4.

From the above expressions it can be seen that the contribution to the W boson mass from the top quark mass has a quadratic dependence while the contribution from the Higgs mass has only a logarithmic dependence, indicating the strong dependence of the electroweak sector on the top quark mass.

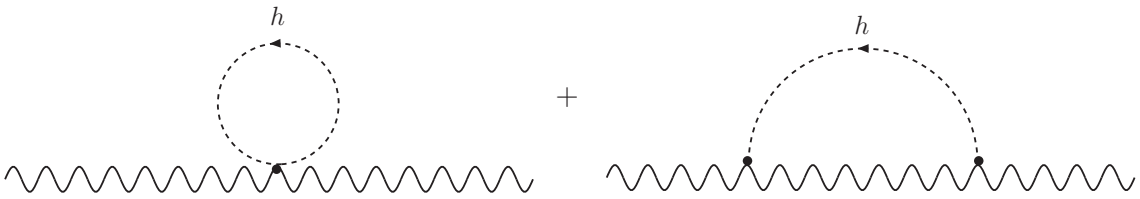

Figure 2.4: Virtual Higgs boson loops contributing to the W and Z boson masses.

Since the top quark and W boson have both been discovered and measured in experiments, and the Higgs still remains undetected, one can turn the above argument around and obtain a prediction for the Higgs boson mass from the measured values of the top quark and W boson masses. The plots of figure 2.5 show predictions for the Higgs boson mass from global fits to electroweak data, as a function of the W boson and top quark masses.

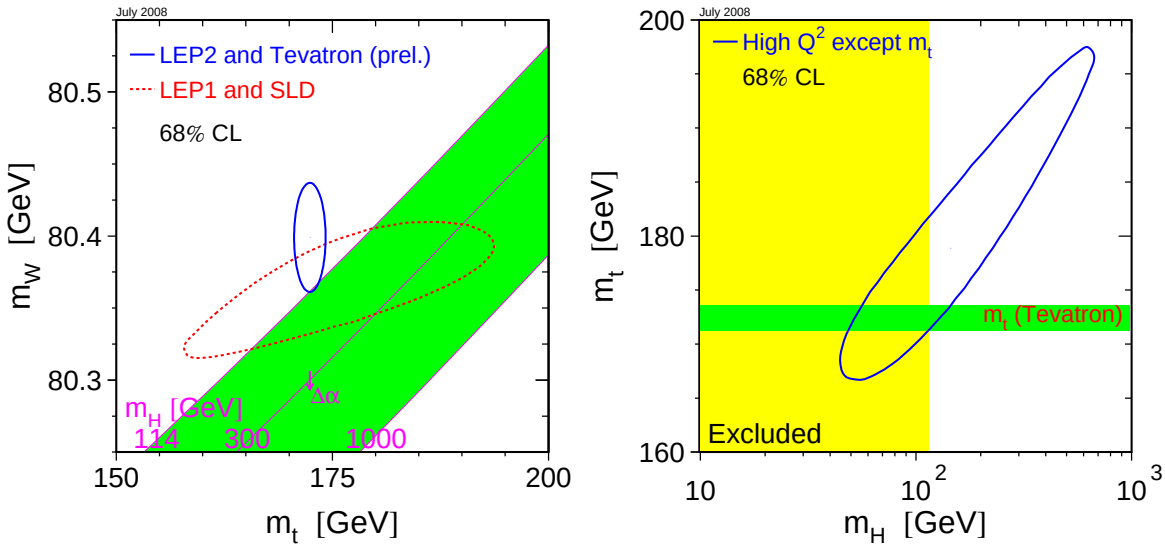

Figure 2.5: *Left:* Contour plot of the dependence of the Higgs mass prediction on the measured values of the top quark and W boson mass. *Right:* Plot of the dependence of the top quark mass on the Higgs mass with the yellow area being excluded from direct searches at LEP, and the blue ellipse indicating the best fit to all electroweak data. Both from [20].

The plot on the left of figure 2.5 shows the dependence of the Higgs mass prediction on the values of the top quark and W boson masses, with the contours representing the current experimental precision, and the constant lines indicating different Higgs masses. The plot on the right of figure 2.5 shows the dependence of the top quark mass versus the Higgs mass, with the yellow shaded area indicating the Higgs mass range currently excluded from direct searches at LEP, and the solid blue ellipse indicating

the best fit prediction from global fits to electroweak data.

It can be seen from these plots that an increased precision in the top quark mass can lead to more powerful constraints for the predictions of the Higgs mass and can provide rigorous tests of the SM.

2.3 The Top Quark Beyond the Standard Model

As is suggested by the arguments of section 2.1.3, the SM must be an effective theory describing the interactions of elementary particles in the energy range currently accessible by experiments, but for a more complete description of the fundamental phenomena of nature, physics beyond the SM must be present.

Due to its large mass, the top quark plays an important role in such theories. For example in the MSSM, the top quark provides the main contribution in loop diagrams for the cancellation of the quadratic terms in the renormalization of the Higgs boson mass (which is a consequence of the Hierarchy problem), thereby solving the fine-tuning problem. The Feynman diagrams with the fermionic top quark loop and the bosonic supersymmetric partner of the top, the stop quark, leading to the cancellation of the quadratic terms in the Higgs boson mass, can be seen in figure 2.6.

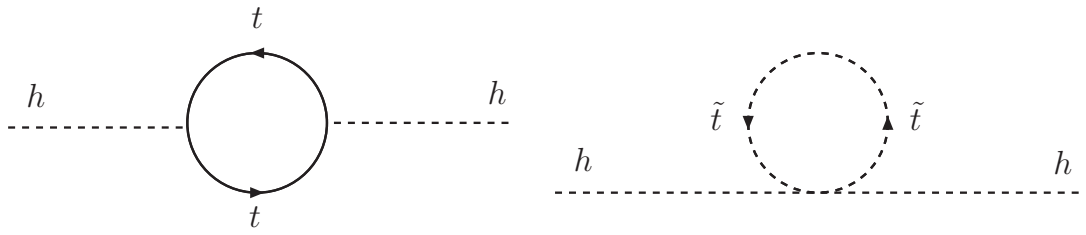

Figure 2.6: Feynman diagrams contributing to the cancellation of the quadratic terms in the renormalization of the Higgs boson mass between a fermionic top quark loop and a bosonic stop quark loop.

The radiative corrections to the Higgs boson mass in the context of the MSSM are given by [22]

$$\Delta M_H^2 = \frac{3G_F M_t^4}{\sqrt{2}\pi^2 \sin^2\beta} \ln\left(\frac{M_{\tilde{t}}}{M_t}\right) \tag{2.6}$$

where $M_{\tilde{t}}$ is the mass of the top quark's supersymmetric partner, the stop quark, and $\tan\beta = \frac{\nu_2}{\nu_1}$ is the ratio of the vacuum expectation values for the two Higgs fields present in the MSSM.

The plot of figure 2.7 shows the dependence of the Higgs mass in different SUSY models on the top quark and W boson masses, with the different ellipses representing

the current and projected experimental uncertainties in present and future colliders. It can be seen in this plot that an increased precision in the top quark mass can lead

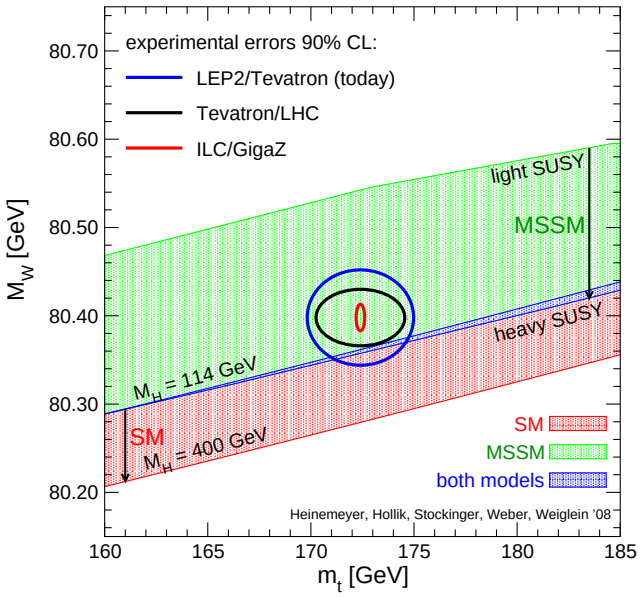

Figure 2.7: Contour plot of the dependence of different SUSY models on the measured values of the top quark and W boson at current and future collider experiments. Updated from [22].

to a better separation between the different SUSY scenarios.

In addition, increased precision in the top quark mass can lead to a better determination of the parameters of the stop sector in the MSSM, such as the stop mixing angle and stop trilinear coupling [23]. In scenarios of mSUGRA models, it has been shown [22] that the uncertainty on the predictions of the neutralino and chargino masses scales directly with the uncertainty on the top quark mass. From these, and more detailed arguments given in [22, 23], it can be understood that the large value of the top quark mass has a big impact on different supersymmetric models, and hence a precise knowledge of M_t is required for detailed studies of the validity and self-consistency of these models.

2.4 Motivation for a Linear Collider

Over the years, many particle accelerators have been constructed and operated successfully, contributing to our understanding of the SM. Most of these machines can be separated in two categories, hadron colliders (e.g. ISR, SPS, Tevatron) and lepton colliders (e.g. PETRA, LEP, SLC), each of which has different advantages and disadvantages in the experimental environment they offer.

Hadron colliders have historically preceded lepton colliders in their energy reach, being characterized as discovery machines where new particles are first discovered, while lepton colliders can be characterized as precision machines, being able to measure many of the properties of the discovered particles with very high precision. For example the W and Z bosons were first discovered at the SPS collider at CERN, but it took the LEP collider to make precision measurements of their properties leading to important discoveries about the nature of the SM (such as confirming that there are only three generations of neutrinos from precision measurements of the Z lineshape).

The main problems of hadron colliders, compromising their precision are:

- Due to the constituent nature of the hadrons (typically protons) being collided in hadron colliders, only a fraction of the available centre-of-mass energy is utilized in each collision, and it differs on an event-by-event basis. In addition, the initial state of the interaction is not well defined, since the type and fraction of energy of the particle involved in the hard process is unknown, leading to the statistical interpretation of the initial state (using parton distribution functions). Also complications in the reconstruction of the final state of an event exist, such as being limited to mainly use variables in the transverse plane for the analysis of data.

- The total cross-section for proton-proton scattering is very large, but is hugely dominated by QCD backgrounds, with the interesting processes usually being many orders of magnitude less than the total proton-proton cross-section. Even though signal event rates are reasonably high, this makes the use of highly sophisticated trigger systems in hadron colliders mandatory, such that the experiments can select the interesting events from the pool of backgrounds.

- In order to discriminate the signal events from the QCD backgrounds, physics channels with high energy leptons or photons in the final state are usually chosen, restricting the available range and type of processes that can be studied, and also limiting the available statistics for a particular process.

- Another problem related to the large scattering cross-section at hadron colliders is the problem of pile-up of events. For every hard interaction there are many soft interactions, which together with with the parton remnant create many tracks and different signatures in the detector, which must be separated with sophisticated event reconstruction and pattern recognition algorithms before the events can be used for physics analysis.

For the above reasons, it is clear that while a hadron collider is an excellent tool for discovery physics, due to its high energy reach, it offers a hostile experimental environment compromising the precision at which physics studies can be made.

Lepton colliders solve most of the above problems and that is why they are preferred as machines for precision studies. The main characteristics of the experimental environment of lepton colliders are:

- Lepton colliders collide elementary particles, giving a well defined initial state in the interaction, such that events can be fully reconstructed in the detector. In addition, the full available centre-of-mass energy of the colliding particles contributes to the hard process.

- The total cross-section for e^+e^- scattering is much lower than that of proton-proton scattering, but the interesting processes are potentially only one or two orders of magnitude lower than the total cross-section, giving a good signal to background ratio.

  Since the total event rate is generally low, the requirements for the trigger systems are much lower than those of hadron colliders, and are often not needed thereby not rejecting signal events at the trigger level.

- Due to the low event rate at lepton colliders, with low occupancy and particle multiplicities per bunch crossing, there are no problems with pile-up of events, making the requirements for reconstruction and event selection looser. Because of this, lepton collider detectors can be designed to be more precision oriented.

- In lepton colliders, the centre-of-mass energy of the collision, and the polarization of the beams (if available) can be tuned in such a way to make studies dependent on these parameters, such as threshold scans or spin-dependent studies of the weak interaction, significantly enhancing the precision at which these physics studies can be made.

The Large Hadron Collider (LHC) at CERN, anticipated to start collisions in 2009 with a centre-of-mass energy of 14 TeV, is very likely to discover the Higgs boson (if it exists), and give evidence for physics beyond the SM. However, for detailed studies of the Higgs boson, such as precision measurements of its mass, spin and couplings, and precision studies of physics beyond the SM, a lepton collider will be needed operating at the energy range of 0.5 - 1 TeV [10].

The highest energy lepton collider ever built was the LEP collider at CERN, which operated from 1989–2000. LEP was a circular machine colliding electrons with positrons and it attained a maximum centre-of-mass energy of collisions of 209 GeV.

The next generation of an e^+e^- collider needs to be able to attain centre-of-mass energies in the range of 0.5–1 TeV. This cannot be achieved in a (realistic) circular machine because of energy loss due to synchrotron radiation.

When electrons are bent in a ring, they lose energy via synchrotron radiation. The energy loss per revolution is approximately given by

$$\Delta E \propto \frac{1}{R}\left(\frac{E}{m}\right)^4 \tag{2.7}$$

where E is the energy of the particle, m is its mass and R is the bending radius. Since the energy loss per revolution scales as the fourth power of the beam energy, the energy losses per turn for a 250 GeV beam in a LEP-sized ring would be unacceptably large (LEP lost about 2.5% of its beam energy per turn). The alternative is to increase the radius of the collider in order to compensate for the energy loss, which would give an unrealistically large (and expensive) collider. Therefore, the only realistic solution is to make the collider linear.

Over the last 20 years there have been many studies for the physics case and accelerator design of a future linear collider, with the most notable being the TESLA project being mainly supported by Europe [24], the NLC project being mainly supported by the US [25], and the JLC/GLC project being mainly supported by Asia [26]. In 2004, these three collaborations joined forces in a single project for the proposed future linear collider, now known as the International Linear Collider (ILC) [27]. The details about the accelerator and detector designs for the ILC are discussed in chapter 3.

2.5 The Top Quark at a Linear Collider

The measurement of the top quark properties will be one of the most important physics goals of a future linear collider. Due to the clean experimental environment with well understood backgrounds, and the ability to have centre-of-mass energy and beam polarization tuning, the top quark parameters can be measured with unprecedented precision [27].

At the ILC, top quarks will be primarily produced in pairs via the reaction $e^+e^- \rightarrow \gamma, Z^* \rightarrow t\bar{t}$, as can be seen in the Feynman diagram of figure 2.8.

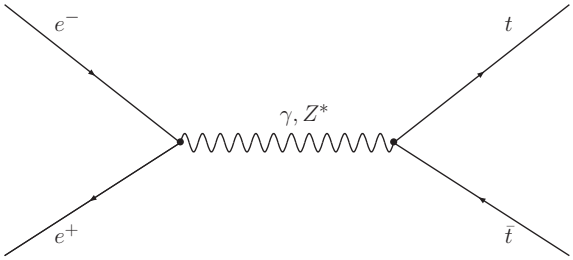

Figure 2.8: Feynman diagram for $t\bar{t}$ production at a linear collider.

2.5.1 Threshold Scan

The production of top quarks at the ILC starts at centre-of-mass energies around the $t\bar{t}$ production threshold of $\sqrt{s} \approx 2M_t$. The energy dependence of the cross-section at the threshold region, and the fact that due to its large width $\Gamma_t \approx 1.4$ GeV, the top quark decays before it can hadronize, allowing reliable perturbative predictions of its cross-section lineshape, allows for precision top quark measurements using the threshold scan method. In a threshold scan, the cross-section for $t\bar{t}$ production is measured in the threshold region by varying the centre-of-mass energy of collisions and measuring the rate of colour singlet top quark events. From the location and rise of the cross-section lineshape, one can precisely extract the top quark mass, while the shape and normalization yields information about the top quark width Γ_t and the strong coupling constant α_s. The energy dependence of the total cross-section for $t\bar{t}$ production at threshold can be seen in figure 2.9

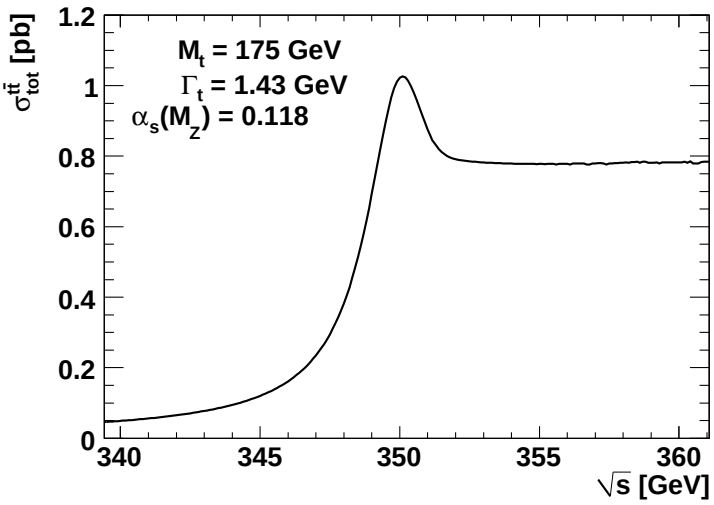

Figure 2.9: Energy dependence of the $t\bar{t}$ production cross-section in the threshold region (with no experimental effects applied).

The top threshold scan is unaffected from systematic uncertainties arising from

event reconstruction in a detector since the identification and counting of colour singlet top quarks suffices for the cross-section measurement.

Many studies have been done over the years [28, 29, 30, 31] on the possibility of the threshold scan measurement, identifying that the most important systematic effect is likely going to be from uncertainties in the knowledge of the collision centre-of-mass energy and the shape of the luminosity spectrum $d\mathcal{L}/dE$ (see chapter 4).

2.5.2 Direct Reconstruction in the Continuum

The top quark mass can also be measured via direct reconstruction in the continuum (at nominal ILC energies of 500 GeV), following similar methods to those employed at the Tevatron and the LHC [32]. The expected precision from these machines is likely to be ~ 1 GeV, limited by systematic uncertainties.

One could (a-priori) hope that the cleaner environment at the ILC would lead to smaller systematic uncertainties and thus improve upon the measurement from the hadron colliders.

Preliminary studies [33] have shown that a statistical uncertainty of $(\Delta M_t)_{\text{stat}} \sim 100$ MeV could be achieved at $\sqrt{s} = 500$ GeV with an integrated luminosity of 300 fb^{-1}, considering only the fully hadronic decay channel. The statistical uncertainty in the semileptonic decay channel would likely be of the same order.

However, like at hadron colliders, systematic uncertainties are expected again to be the limiting factor. The expected uncertainty due to the fragmentation and hadronization modelling is ~ 250 (400) MeV in case of the semileptonic (fully hadronic) decay channel [34]. Preliminary studies suggest that Bose-Einstein correlations could contribute an uncertainty of $\sim 100 - 250$ MeV [34], while colour reconnection effects could also lead to an uncertainty of $\mathcal{O}(100)$ MeV [35]. Finally, for the direct reconstruction method it is not known how the maximum in the invariant mass distribution is related to the mass parameter in the QCD Lagrangian. One might argue that the maximum is related to the top quark pole mass. However, the pole mass has an intrinsic theoretical ambiguity of $\mathcal{O}(\Lambda_{\text{QCD}})$ [36, 37]. Taking into account all these contributions, and the fact that we have not considered experimental systematic uncertainties (e.g. jet energy calibration), it is difficult to imagine that the total systematic uncertainty would be less than $(\Delta m_t)_{\text{syst}} \sim 500$ MeV, therefore completely dominating this measurement.

Chapter 3

The International Linear Collider

It is widely accepted in the particle physics community that the next major project in the high energy frontier should be a high luminosity electron-positron linear collider operating in the TeV energy range. In 2004, in a worldwide consensus, the International Committee for Future Accelerators (ICFA) recommended that the future linear collider should be based on a design using superconducting accelerating cavities [38], leading to the International Linear Collider (ILC) project [27].

In this chapter the basic components of the accelerator as well as the requirements for the detector are discussed.

3.1 The Accelerator

The accelerator layout for the ILC is subject to constant changes and improvements. The worldwide effort for the design of the accelerator, managed through the Global Design Effort (GDE) committee [39], has produced a Reference Design Report (RDR) [27], which serves as the first detailed technical report defining the parameters and components of the accelerator. The RDR describes the current status of R&D for each accelerator subsystem, with preliminary cost estimates, and provides the direction to the research community for the challenges that need to be solved for the project to be realized. The next major milestone for the ILC will be the Technical Design Report (TDR), envisioned to be ready by 2012, which will provide the final technical report including all engineering details and is intended to serve as the final document to be submitted to funding agencies for project approval and construction.

The baseline design for the ILC, as outlined in the RDR, has been developed in order to achieve a continuous operational energy range of $\sqrt{s}$ 200–500 GeV, with

a peak luminosity of 2×10^{34} cm^{-2}s^{-1}, and an availability of $\geq 75\%$, such that the accelerator can deliver 500 fb^{-1} in the first four years of operation. Finally, the machine must be upgradable to a $\sqrt{s}$ of 1 TeV.

Table 3.1 summarizes the basic design parameters for the baseline machine, as given in the RDR.

Table 3.1: Basic design parameters for the ILC with 500 GeV centre-of-mass energy [27].

Parameter	Unit	
Centre-of-mass energy	GeV	200 – 500
Peak luminosity	cm^{-2}s^{-1}	2×10^{34}
Average beam current in pulse	mA	9.0
Pulse rate	Hz	5.0
Pulse length (beam)	ms	~ 1
Number of bunches per pulse		1000 – 5400
Charge per bunch	nC	1.6 – 3.2
Accelerating gradient	MV/m	31.5
RF pulse length	ms	1.6
Beam power (per beam)	MW	10.8
Typical beam size at IP ($h \times v$)	nm	640 × 5.7
Total AC Power consumption	MW	230

The baseline design is based on 1.3 GHz superconducting radio-frequency (SCRF) accelerating cavities designed to deliver an average accelerating gradient of 31.5 MV/m, which together with the Beam Delivery System (BDS) leads to a total machine length in excess of 30 km. The current status of the accelerator layout indicating the location of all major subsystems can be seen in figure 3.1.

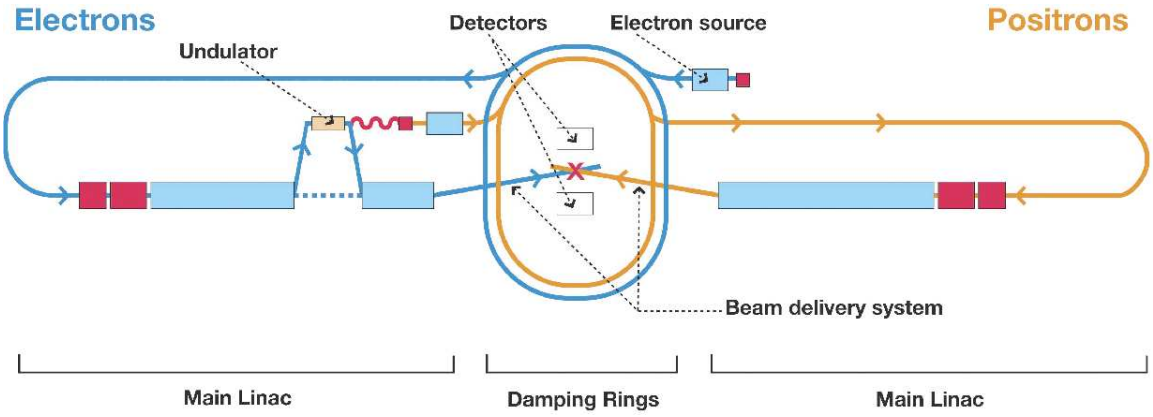

Figure 3.1: Schematic diagram of the current baseline design for the ILC corresponding to a machine with 500 GeV centre-of-mass energy [40].

In the following, a short overview of the major subsystems of the ILC machine is

given.

3.1.1 Particle Sources

The first step in the accelerator chain is to generate the particles to be accelerated. The requirements for the particle sources are to produce a large amount of particles ($2{\cdot}10^{10}$ per bunch) with a low emittance such that they can be captured and controlled by the beam optics. Furthermore, the electron beam must be able to achieve 80% polarization.

This is achieved for the electrons by using a laser driven photoinjector, which uses circularly polarized photons from the laser illuminating a photocathode (typically GaAs or Cs_2Te) such that electrons are produced via the photoelectric effect.

The positron source is located in the middle of the electron linac, and uses the electron beam (already at 150 GeV) to create positrons via pair production. The electron beam is passed through a helical undulator producing photons ($\sim$10 MeV) which are in turn fired into a target in order to produce e^+e^- pairs. The positrons are then separated by a magnetic field before being pre-accelerated and injected into the damping rings. Even though not in the baseline design parameters, the use of the undulator allows the production of polarized positrons with a polarization of 30 – 60%.

3.1.2 Damping Rings

After the beams have been pre-accelerated to 5 GeV, they enter the damping rings (DR) located in the centre of the ILC accelerator complex. In the damping rings the particles are made to emit synchrotron radiation by the use of bending dipole and wiggler magnets, while any energy loss is restored through additional accelerating cavities. This causes the particles to lose transverse momentum while their longitudinal momentum remains constant (since they experience only the restoring longitudinal acceleration) thereby reducing the overall phase space volume of each bunch, corresponding to reducing the beam emittance.

Both the electron and positron damping rings will be placed in the same tunnel, located in the centre of the ILC site, with a total circumference of 6.7 km.

3.1.3 Main Linac

After damping, the beams will be inserted in the ring to main linac (RTML) transfer line, where they will be collimated and undergo bunch compression in order to reduce

the RMS bunch length. The beam energy in the RTML line will be increased to 15 GeV to increase the fractional energy spread associated with bunch compression and bring the beams in the design energy for injection in the linacs.

When injected in the linacs, the beams will be accelerated to their full energy of 250 GeV using superconducting niobium cavities operating at a radiofrequency of 1.3 GHz. For an average accelerating gradient of 31.5 MV/m, and including focusing quadrupoles and diagnostic sections, the combined length for both linacs will be 23 km.

The main functional requirements of the linac systems are to preserve the small bunch emittances without introducing significant beam jitter. Furthermore, the beam energy spread must be maintained within the design requirement of 0.1% at the interaction point (IP).

3.1.4 Beam Delivery System

After acceleration, the beams enter the beam delivery system that transports them from the linacs to the IP and prepares them for collision. The BDS is required to measure the beams in diagnostic sections and match the beam optics to the final focus system, protect the machine and detector from errant beams from the main linacs, collimate any beam halo in order to minimize backgrounds in the detectors and finally perform the beam energy and polarization measurements before and after the IP.

The final element of the BDS is the final focus system bringing the beam into the tiny beam spots required at the IP in order to achieve the design luminosity.

The total length of the beam delivery system is approximately 4.5 km.

3.1.5 Interaction Region

The interaction region refers to the point of collision of the two beams, and the detector surrounding it. In the ILC design the two beams do not collide head-on but rather with a crossing angle of 14 mrad in the horizontal plane.

Due to the elongated shape of the ILC bunches (cf. Table 3.2), this would decrease the effective overlap area of the bunches which would decrease luminosity. For this reason crab cavities are used, which rotate the bunches in the horizontal plane just before the collision in order to make them collide head-on and hence recover the luminosity.

In previous designs the ILC had two separate interaction regions in order to accommodate two different detectors. Due to cost considerations arising from the need

for two separate beam delivery systems in the two IR design, the RDR employed a design with a single IR and two detectors sharing it. In this so-called 'push-pull' configuration, the two detectors would be 'pushed' and 'pulled' interchangeably from the IR (with a period of weeks or months) thereby sharing the luminosity between them.

3.1.6 Extraction Line

After collision, the beams need to be transported to the beam dumps. Considering that the bunches are deformed from the beam-beam interactions at the IP (cf. chapter 4), and that they have about 10 MW of power each, their safe extraction and disposal is a delicate operation. The extraction line consists of additional optics in order to restore the bunches to their trajectory, diagnostic devices to measure the post-IP energy and polarization, and finally the beam dumps, which are cylindrical stainless steel high pressure water vessels capable of absorbing up to 18 MW of power per bunch.

3.1.7 Operational Parameter Plane

The ILC design goal of achieving a peak luminosity of 2×10^{34} cm^{-2}s^{-1} at a centre-of-mass energy of collisions of 500 GeV depends on a number of beam parameters, such as the number of particles in a bunch, the number of bunches per train as well as the beta functions and RMS beam sizes at the IP. The values of these parameters depend on the performance of several of the above subsystems. For this reason it was decided that rather than designing the ILC for a fixed set of beam parameters, an operational parameter plane would allow greater flexibility for the machine reaching its design luminosity and would mitigate the risk of under-performance of a subsystem through trade-offs in the parameter plane.

The four main parameter sets representing different scenarios of the accelerator and beam parameters are :

Nominal The reference parameter set in which all parameters are at their nominal values.

Low Charge (Low N) The high bunch charge of $2 \cdot 10^{10}$ can lead to problems such as space charge effects in the damping rings, emittance dilution due to wakefield effects in the main linacs or high disruption at the IP. In this case the bunch charge can be halved while the number of bunches is doubled in order to maintain the same luminosity. This scenario would lead to a lower beamstrahlung

and lower detector backgrounds at the IP but would put stringent requirements in the damping rings and bunch compressor.

Large Y Emittance (Large Y) The Large Y parameter set refers to the situation where the very low vertical emittance at the IP cannot be achieved due to tuning problems at the damping rings or BDS. It assumes a vertical emittance that is twice the design value leading to a larger beam size at the IP. In this case the luminosity is recovered by tighter focusing at the IP while the bunch length is increased in order to reduce beamstrahlung and detector backgrounds.

Low Power (Low P) The Low P parameter set refers to the situation where the nominal beam power or beam current cannot be used due to problems in the injector systems, the damping rings, the main linacs or the BDS. In this case the Low P parameter set assumes that only half the nominal beam power is used and the beam current is reduced by 30%. The luminosity is then recovered by stronger focusing at the IP leading to an increased amount of beamstrahlung.

Table 3.2 summarizes the main parameters for the four different parameter sets mentioned above. Each parameter set is formed in order to achieve the design luminosity of 2×10^{34} cm^{-2}s^{-1}.

Table 3.2: Beam and IP parameter plane for a 500GeV machine [27]

Parameter	Symbol/Unit	**Nominal**	**LowN**	**LargeY**	**LowP**
Particles per bunch	N (10^{10})	2	1	2	2
Bunches per train	n_b	2625	5120	2625	1320
Beta function at IP	β_x^* (mm)	20	11	11	11
Beta function at IP	β_y^* (mm)	0.4	0.2	0.6	0.2
RMS beam size at IP	σ_x^* (nm)	639	474	474	474
RMS beam size at IP	σ_y^* (nm)	5.7	3.5	9.9	3.8
RMS bunch length	σ_z (μm)	300	200	500	200

3.1.8 Alternative Projects: CLIC

The ILC is not the only proposed option for a future e^+e^- linear collider. The most prominent of the alternative options for a linear collider is the Compact LInear Collider (CLIC) project being currently pursued primarily at CERN.

The CLIC project aims to achieve a centre-of-mass energy of collisions of 3–5 TeV by using a novel design where the primary beam is accelerated using a so-called

secondary 'drive beam' with relatively low energy but very high intensity. The acceleration will be achieved by transferring energy from the secondary drive beam to the primary beam by the drive beam induced wakefields. This design hopes to achieve accelerating gradients of about 100 MV/m in conventional room temperature copper accelerating structures.

This very promising method would achieve about an order of magnitude more acceleration per metre of accelerator thereby either significantly increasing the energy of an ILC length accelerator, or significantly reducing the length (and thus the cost), but the exact design and large scale applicability of the method are still to be proven.

3.2 The Detector(s)

With a clean experimental environment, a well defined initial state, a low event rate and essentially a triggerless operation, the precision of the physics results will be largely constrained by the detector performance.

For this reason, the detectors need to be designed to deliver excellent performance across the whole energy range of the ILC, with many design parameters requiring an improvement of an order of magnitude in comparison to the detectors used at LEP.

In the following, the main design requirements for the ILC detectors are discussed and the proposed designs are briefly described.

3.2.1 Detector Requirements

The main requirements for the ILC detectors are [27, 41]:

Tracking The benchmark process for the tracking system is the recoil mass measurement of the Higgs boson in Higgsstrahlung production via $e^+e^- \to Z^* \to ZH \to \mu^+\mu^- X$ where X denotes the decay products of the Higgs. This channel allows a model independent measurement of the Higgs mass by measuring the two muons from the recoil Z decay, without making any assumptions for the Higgs decay. For this measurement to take place the momentum resolution of the tracker in the central region needs to be better than $\Delta(1/p_t) = 5 \cdot 10^{-5}$ GeV^{-1}, an order of magnitude improvement over what was achieved in the LEP detectors.

Furthermore, high resolution forward tracking is important for the measurement of the luminosity spectrum using Bhabha events (see chapter 4).

Calorimetry and Particle Flow Physics processes with many jets in the final state are going to be increasingly important at the ILC, especially those originating

from Higgs, top quark and W and Z decays. The ILC detector must be able to separate and reconstruct the invariant masses of such decay products with high precision.

The goal for the calorimeter of the ILC detector is to be able to distinguish between $W \to q\bar{q}$ and $Z \to q\bar{q}$ decays, i.e. have a dijet invariant mass resolution comparable to the natural width of the particles $\sigma_m/m \sim \Gamma_W/m_W \sim \Gamma_Z/m_Z$. This requires a high granularity calorimeter and a jet energy resolution better than $\sigma_E = 30\%/\sqrt{E}$, a factor of two improvement over the jet energy resolution achieved at the LEP detectors [42].

One of the proposed ways for achieving this is the method of particle flow [43, 44]. Particle flow algorithms (PFA) reconstruct the four-vectors for all visible particles in an event by combining information from the tracker and calorimeter systems.

From measurements of jet fragmentation at LEP [45], approximately 60% of the visible energy of a typical jet is attributed to charged particles, 30% of the energy is attributed to photons and the remaining 10% is carried away by long-lived neutral hadrons.

At ILC energies, the momenta of charged particles are best measured in the tracker, photons and neutral pions are best measured in the electromagnetic calorimeter (ECAL) while other neutral hadrons are measured in the hadronic calorimeter (HCAL). Since the tracker and the ECAL typically have much better momentum and energy resolution than the HCAL, the idea of PFA is to use these measurements when available and discard information in the HCAL [44].

The challenge for PFA algorithms to work is to be able to separate particle showers in the calorimeter clusters in order to avoid confusion in associating calorimeter hits with tracks and minimize double counting. Therefore the key parameter of the calorimeter systems is high granularity rather than intrinsic energy resolution.

Vertexing The vertex detector (VTX) needs to be able to efficiently identify secondary vertices for tagging beauty and charm quarks, that are fundamental for a precision measurement of the Higgs branching fractions in $H \to b\bar{b}$ and $H \to c\bar{c}$ decays.

In addition, precise identification of the tagged quark charge can provide valuable information for the measurements of $q\bar{q}$ asymmetries (including $t\bar{t}$ forward-backward asymmetry, see chapter 5), top quark polarization, W helicity or

searches for Wtb anomalous couplings [46].

Hermiticity The measurement of missing energy is one of the most promising signatures for detecting SUSY particles, and so excellent detector hermiticity is needed. In particular, the forward region of the ILC detectors has a very important role due to the increased importance of t-channel processes, and the dependence of PFAs on a hermetic calorimeter.

Low Mass Tracker The ILC detector must have a low mass budget, especially in the tracking systems, in order to minimize unwanted interactions with the detector material which would compromise the resolution of the calorimetric systems and PFA algorithms.

3.2.2 Detector Concepts

For the ILC detectors to meet the desired design requirements, four different groups have been formed pursuing different approaches to the detector design. These detector designs, called detector 'concepts' are :

- LDC: Large Detector Concept[1] [48].
- GLD: Global Large Detector[1] [49]
- SiD: Silicon Detector [50]
- 4th: The 4th Concept [51]

The first three of these concept detectors are designed around the concept of particle flow, by employing high granularity calorimeters and a precision tracker. Their main differences come in the tracker, with the LDC and GLD concepts using a time projection chamber (TPC) while the SiD concept uses a silicon strip based tracker, and the magnetic field configuration (which affects the inner radius of the detector), with SiD opting for a large field of 5 T, LDC for 4 T and GLD for 3–4 T. The 4th concept design is based on a dual readout sampling calorimeter with a TPC or an ultra low mass drift chamber for tracking and an iron free magnet in which the magnetic flux from the inner solenoid is returned by an outer solenoid, giving superb muon identification and coverage.

A comparison of the four detector concepts, indicating their differences and similarities can be seen in figure 3.2.

[1]Due to their similarities, it was decided that the LDC and GLD concepts should be merged in a single detector concept called the International Large Detector (ILD), the detailed specifications of which are still under discussion. More details can be found in [47]

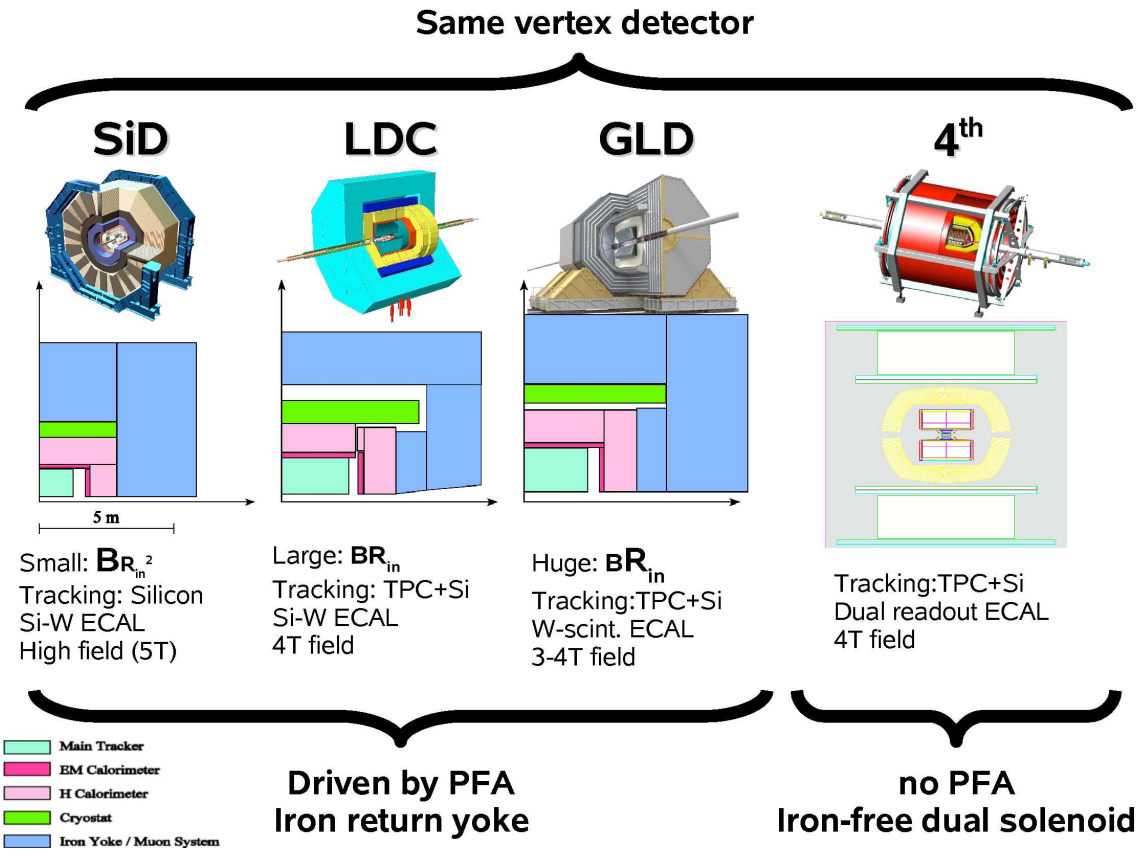

Figure 3.2: A comparison of the four detector concepts, indicating the main differences and similarities between the different designs. Adapted from [52].

It should be noted that currently all detector concepts are subject to extensive R&D, with their detailed specifications rapidly changing. The next step in the development phase is for each detector concept to produce detailed simulation studies of detector performance against benchmark physics processes providing a common ground for comparison and optimization between the different designs.

Chapter 4

The Luminosity Spectrum

In collider particle physics, the two most important parameters of a collider are the centre-of-mass energy of collisions and the luminosity. The centre-of-mass energy defines the available energy at the interaction point (IP) for producing new particles and the luminosity of the collider defines the rate at which new particles can be produced.

The particles in the colliding beams can lose some of their energy at/before the IP due to various energy loss mechanisms. This effectively reduces the centre-of-mass energy of the collision by creating a centre-of-mass energy distribution. The particles in this distribution that contribute to the luminosity of the machine form the so-called luminosity spectrum.

The ILC is intended to be a high precision collider. For precision physics it is important that all these parameters are measured accurately, but in a high energy high luminosity collider, measuring the absolute centre-of-mass energy of collisions, the luminosity and the luminosity spectrum to a high precision can prove a challenging task.

In this chapter, issues related to the measurement of these parameters will be discussed, all of which are very important for precision measurements of the $t\bar{t}$ threshold.

4.1 Luminosity

Luminosity is a measure of the number of particles per unit area per unit time multiplied by the opacity of the target (in our case the opposing beam). In a collider it can be defined as the 4-dimensional overlap integral of the two colliding bunches. For ultra-relativistic beams, this is given by

$$\mathcal{L} = f_c \int\int\int\int_{-\infty}^{+\infty} \rho^+(x,y,s+ct)\rho^-(x,y,s-ct)2c\ dt\ ds\ dx\ dy \tag{4.1}$$

with ρ^+ and ρ^- being the particle charge distributions of the bunches, and f_c the bunch collision frequency.

For bunches with 3-dimensional Gaussian charge distributions, we can write

$$\rho^{\pm}(x,y,s\pm ct) = \frac{N^{\pm}}{(2\pi)^{3/2}\sigma_x(s)\sigma_y(s)\sigma_s} e^{-\frac{(x\pm s\theta)^2}{2\sigma_x(s)^2} - \frac{y^2}{2\sigma_y(s)^2} - \frac{(s\pm ct)^2}{2\sigma_s^2}} \tag{4.2}$$

where N is the number of particles in the bunch, θ is the crossing angle and $\sigma_{x,y,s}(s)$ are the RMS beam sizes along the accelerator axis s. These can be defined as

$$\sigma_{x,y} = \sigma^*_{x,y}\sqrt{1+\left(\frac{s}{\beta^*_{x,y}}\right)^2} \tag{4.3}$$

with $\sigma^*_{x,y}$ the RMS beam size at the collision point and $\beta^*_{x,y}$ the beta function at the IP ($s=0$).

If we perform the integral of eq. 4.1 by using eq. 4.2 and 4.3, and by assuming symmetric beams, we arrive at the standard expression for luminosity

$$\mathcal{L} = f_c \frac{N^+N^-}{4\pi\sigma^*_x\sigma^*_y} S \tag{4.4}$$

with S being the luminosity suppression factor, describing the luminosity loss due to the 'hour-glass' effect [53]. For normal Gaussian bunches colliding head-on, $S = 1$.

The hour-glass effect is a consequence of the tight focusing of the bunches at the IP. To achieve very small beam sizes at the IP, the bunches need to be tightly focused before being brought into collision. This leads to a hour-glass bunch shape, reducing the effective area of overlap of the two bunches and hence reducing luminosity.

Contributing to the hour-glass bunch shape, but enhancing the luminosity, is the 'pinch' effect. This is the mutual self-focusing of the two bunches at the IP due to the attractive forces between their opposite charge. It results in each bunch acting as a thin focusing lens, inducing a stronger focusing of the bunches which enhances

luminosity [54].

Both these effects lead to what is called the disruption of the beam at the IP. This is the bending of the particle trajectories as they are brought into collision with respect to their nominal trajectory. Disruption effects in the x and y directions respectively can be described by the dimensionless disruption parameter [55]

$$\mathcal{D}_{x,y} = \frac{2Nr_e\sigma_z}{\gamma\sigma^*_{x,y}(\sigma^*_x + \sigma^*_y)} \tag{4.5}$$

where $\sigma_{x,y,z}$ are the beam sizes in the x, y and z axis respectively, N is the number of electrons in the bunch, γ is the relativistic Lorentz factor and r_e is the classical electron radius.

For high disruption beams, when $\mathcal{D} > 1$, the particle dynamics at the IP become non-linear, with the two bunches oscillating during collision, leading to an increase of their effective overlap area which enhances luminosity. The explicit calculation of the amount of luminosity enhancement for high disruption beams is a challenging task, with no analytic expression accurately describing the effect, making computer simulations an indispensable tool [54].

Equation 4.4 describes the instantaneous luminosity of the collider and is expressed in units of $\mathrm{cm}^{-2}\mathrm{s}^{-1}$. This can be related to the event rate by using the expression

$$\frac{dN}{dt} = \mathcal{L} \times \sigma \tag{4.6}$$

with σ the cross-section for a given process.

In collider experiments, one measures the number of events observed for a given time of the collider running. Over that time, the collider will deliver a given luminosity to the collision point, the integrated luminosity over a given time.

The relationship between the number of events observed and a cross-section measurement is given by

$$\sigma = \frac{1}{\int \mathcal{L}\ dt} \times N\ . \tag{4.7}$$

Hence, any uncertainty in the value of $\mathcal{L}$ corresponds directly to an uncertainty in the measured σ, and so the luminosity must be measured precisely.

4.1.1 Measuring the Luminosity: LumiCal

The luminosity at the ILC will be measured by using forward calorimetry to detect small-angle Bhabha scattering events. The basic principle of this method is using a

rearranged version of eq. 4.7,

$$\int \mathcal{L}\, dt = \frac{N_{\text{obs}}}{\sigma_{\text{th}}} \tag{4.8}$$

where by having a known cross-section σ_{th} and measuring the event rate N_{obs}, the luminosity of the collider can be measured. This is a well known method and was also used for luminosity measurement at the LEP experiments [56].

The choice of using Bhabha events for the luminosity measurement is mainly driven by

- The Bhabha scattering process is a well known QED process that can be calculated to high precision.
- The cross-section is large ($\mathcal{O}(1\text{ nb})$) with the differential cross-section increasing at small-angles, hence large statistics can be accumulated.
- There are well known backgrounds and the detection technique is simple, mainly using forward calorimetry to identify Bhabha events. In the case of the ILC this will be done in the LumiCal.

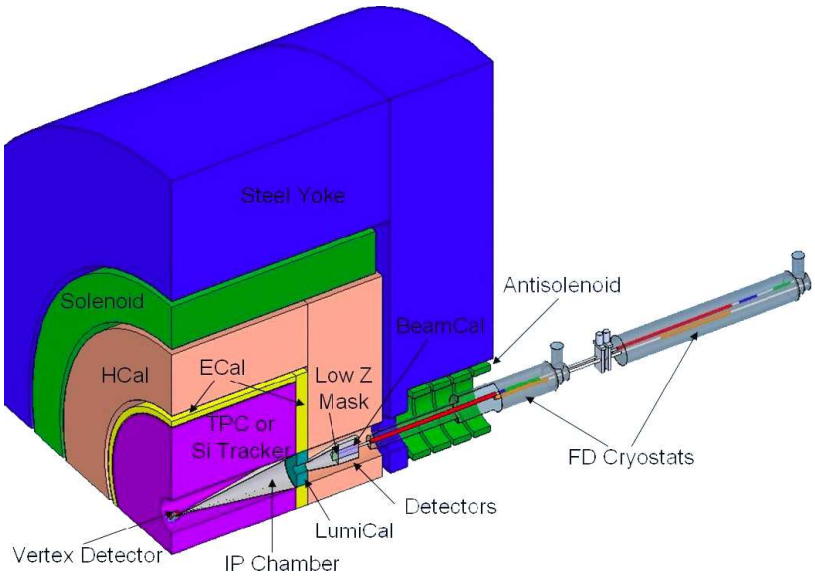

Figure 4.1: Diagram showing the cross-section of a generic ILC detector, with the LumiCal in the forward region.

The LumiCal will be a forward calorimeter positioned approximately 2 m from the IP. It will be a Si/W sandwich calorimeter consisting of 30 disks with an inner radius of 80 mm and outer radius of 190 mm. A diagram of a generic ILC detector with the LumiCal sitting in the forward region, between the tracker and the hadronic calorimeter, can be seen in figure 4.1. The proposed angular acceptance, is from

30 mrad to 90 mrad with an angular resolution in θ of about 2.2×10^{-2} mrad and an energy resolution of $21\%/\sqrt{E_{\text{beam}}}$ [57, 27].

It is designed to deliver a luminosity measurement with precision of $\frac{\Delta\mathcal{L}}{L} < 10^{-3}$ with recent studies showing that the current design will be able to provide a luminosity measurement for $500\,\text{fb}^{-1}$ with relative error $\frac{\Delta\mathcal{L}}{L} = (1.5 \oplus 4) \times 10^{-5}(\text{stat})$ where the theoretical uncertainty on the Bhabha cross-section is expected to be $\sim 2 \times 10^{-4}$ [57].

4.2 Absolute Beam Energy

It is important that the absolute centre-of-mass energy of collisions is precisely known, especially for measurements performed via threshold scans and for the reconstruction of particle resonances.

The nominal centre-of-mass energy of collisions, assuming ideal conditions with no energy losses, is given by (from eq. 4.21)

$$\sqrt{s} = 2\sqrt{E_e E_p} \tag{4.9}$$

where E_e and E_p are the energies of the electron and positron beams respectively. Hence to precisely measure the centre-of-mass energy, a precise measurement of the incoming beam energies is required.

Furthermore, the measurement of the luminosity spectrum, as it will be described in the following section, measures the fractional centre-of-mass energy $x = \frac{\sqrt{s'}}{\sqrt{s}}$, with $\sqrt{s}$ being the nominal and $\sqrt{s'}$ the actual centre-of-mass energy. Therefore, for the measured luminosity spectrum to accurately describe the energy of the collisions, a precise knowledge of $\sqrt{s}$ is needed.

In order to measure the top quark mass via a threshold scan with a precision of $\mathcal{O}$(50–100 MeV), the absolute centre-of-mass energy of the collisions needs to be known with a precision at the ≤ 50 MeV level. To do this, the absolute beam energy of the incoming beams must be measured with a fractional uncertainty better than 10^{-4}. At the ILC this will be done with an upstream energy spectrometer based on beam position monitors (BPMs).

4.2.1 Measuring the Beam Energy: Energy Spectrometer

When a charged particle of charge q passes through a magnetic field B, it is deflected by an angle θ which is inversely proportional to its energy E. The amount of deflection

is given by

$$\theta = \frac{cq}{E} \int B \cdot dl \tag{4.10}$$

where c is the speed of light and dl is the path length through the magnetic field that the particle travels. Therefore, by bending a particle beam by a known magnetic field and measuring the amount of deflection, a measurement of the beam energy can be obtained.

At the ILC, this concept will be implemented in the form of an upstream magnetic spectrometer. The spectrometer will use a four magnet chicane in order to deflect the beam and beam BPMs that will measure the amount of deflection. A schematic diagram of this arrangement can be seen in figure 4.2.

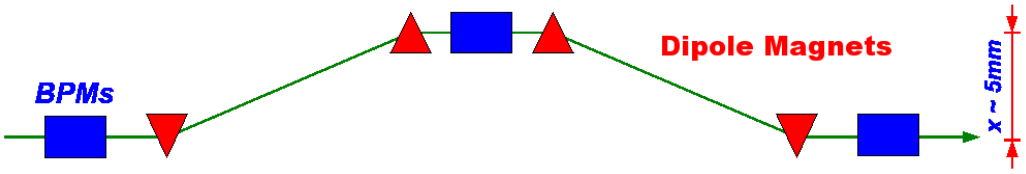

Figure 4.2: Schematic of the magnetic chicane for the ILC upstream energy spectrometer [58].

The precision of the energy measurement depends on the knowledge of the amount of deflection. This is governed by the integral bending field of the magnets and the accuracy of the beam position measurement from the BPMs.

In the current ILC spectrometer design, the amount of deflection in the spectrometer chicane is limited to $x \leq 5$ mm, leading to a total chicane length of ~ 50 m. A larger deflection would induce an unacceptable amount of emittance growth in the beam due to synchrotron radiation at the bends. This restriction creates the condition that the precision of the energy measurement depends on the precision of the BPMs, given by $\delta E/E \sim \sigma_{\mathrm{BPM}}/5$ mm, with σ_{BPM} being the single bunch position measurement resolution of the BPMs. To achieve the required energy measurement precision, BPMs with a resolution better than 500 nm will be needed. This resolution on a single bunch measurement can be easily achieved with current cavity BPM designs [59].

The major challenge in the operation of the energy spectrometer will be the stability of the measurement over long periods. In order to avoid extensive re-calibrations of the spectrometer, and the consequent loss of luminosity, the system must be stable at the 500 nm level over many hours. Initial studies show that this is possible [58], but high resolution cavity BPMs will be needed in order to identify and correlate systematic effects across the whole spectrometer system.

Finally, the last key point in the beam energy measurement is the energy loss of the beam from the spectrometer to the IP. The spectrometer in the current ILC design will be positioned in the beam delivery system, approximately 700 m upstream of the IP [27]. It is therefore important that the energy losses of the beam from the spectrometer position to the IP are well understood.

4.2.2 Measuring the Beam Energy: Other Methods

The upstream energy spectrometer is not the only method to measure the beam energy at the ILC. Alternatives include both beam-based methods, such as the downstream synchrotron stripe energy spectrometer, and using physics reference channels such as utilizing the information from final state muon pairs resonant with the known Z mass.

The downstream energy spectrometer will be placed in the extraction line, and will measure the distance between two synchrotron stripes created by a vertical bend (using an analysing dipole magnet) in the trajectory of the spent beam. It is anticipated that the downstream energy spectrometer will be able to provide an energy measurement on the spent beam with an accuracy of 10^{-4} [60].

Other beam-based methods being currently investigated include the Compton backstattering method which uses the centroid of Compton photons and the kinematic edge of Compton electrons to obtain a measurement of the incident beam energy [61]. Also, methods using synchrotron radiation from the upstream spectrometer dipole magnets [62] and methods based on resonant absorbtion of light by the beam particles [63] are also under investigation.

4.3 Luminosity Spectrum Explained

The centre-of-mass energy of collisions at any high energy collider will have deviations from its nominal value. There are various energy loss mechanisms contributing to the smearing of the nominal energy, from accelerator based effects during acceleration and transportation of the beams, to electromagnetic and QED based effects at the collision point. At high energy linear colliders such as the ILC, the major energy loss mechanisms are :

Initial State Radiation (ISR) is the QED process in which the electrons (positrons) can emit incoherent collinear radiation before the collision. The emitted photons will carry some of the electron's momentum thereby reducing its effective

energy. At ILC energies it accounts for approximately a 5% reduction in the average CMS of collisions, making it the largest energy loss contribution. ISR is calculable to 1% precision in QED [64].

Beam Energy Spread (BES) is the intrinsic energy spread of the particles within the bunches due to their interaction with the various accelerator elements from the source to the IP. The main contributions come from the bunch compressor (at 4.8 GeV) before entering the main linac, where the energy spread is increased from 0.15% to 1.5%, and from wakefield effects in the main linac. During acceleration in the linacs, the absolute beam energy spread stays approximately constant while the relative energy spread decreases roughly as E_0/E, with E being the beam energy after acceleration and E_0 the initial beam energy injected in the main linacs. The electron beam can further increase its energy spread by passing through the undulator to produce positrons, and so it is possible to have asymmetric energy spread between the two beams. At exit from the main linacs the fractional energy spreads are expected to be 0.14% for the e^- beam and 0.1% for the e^+ beam. Through energy collimation at the beam delivery system, the ILC design goal is to deliver a Gaussian distributed energy spread of 0.1% at the IP [27].

Beamstrahlung (BS) is a type of electromagnetic radiation that occurs when two high energy high current bunches interact with each other. It is a direct consequence of the high disruption at the IP. Disruption causes the colliding particles to deviate from their nominal trajectory, and beamstrahlung is the radiation resulting from this change in trajectory.

It is similar to synchrotron radiation, the radiation emitted when a charged particle is bent by an external magnetic field. In the case of beamstrahlung, the particles of one bunch experience the coherent field of the opposing bunch, causing them to deviate from their nominal trajectory and hence emit beamstrahlung radiation.

Beamstrahlung is usually described by the beamstrahlung parameter Υ, which gives a measure of the field strength as seen in the electron's rest frame. For beams with a Gaussian charge distribution, the average value of Υ is given by [65]:

$$\langle \Upsilon \rangle = \frac{5}{6} \frac{N r_e^2 \gamma}{\alpha(\sigma_x^* + \sigma_y^*)\sigma_z^*} \tag{4.11}$$

where α is the electromagnetic coupling constant.

The average energy loss due to beamstrahlung is approximately given by [55]:

$$\delta_{BS} \propto \frac{N^2 \epsilon_y}{(\sigma_x^* \sigma_y^*)^2} \tag{4.12}$$

for $\sigma_y^* << \sigma_x^*$, with ϵ_y being the beam emittance in the y axis. For the nominal ILC machine δ_{BS} is expected to be 2.4% [27].

The energy distribution of colliding particles having undergone the above energy losses forms what is called the luminosity spectrum $d\mathcal{L}/d\sqrt{s}$. The plot of figure 4.3 shows the three components of the luminosity spectrum for a $\sqrt{s} = 350$ GeV, calculated using the methods described in the following section.

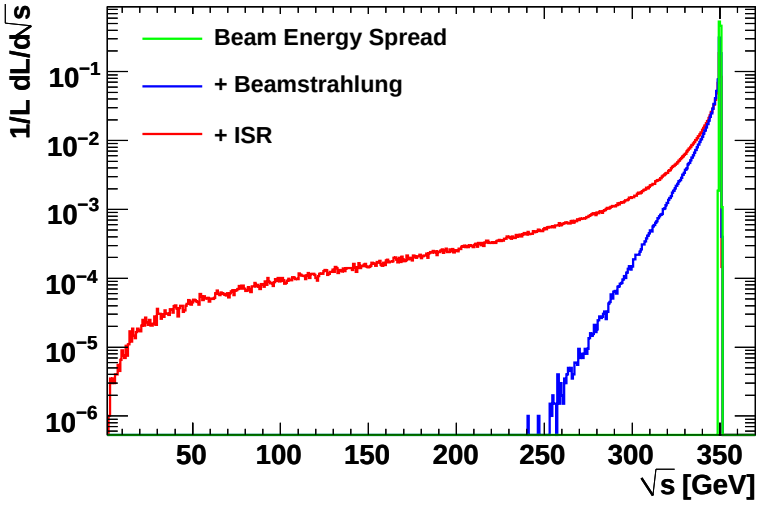

Figure 4.3: The three components of the luminosity spectrum for a centre-of-mass energy of 350 GeV, including a BES of 0.1%.

4.3.1 Simulating the Luminosity Spectrum

Realistic physics studies at the ILC require an accurate description of the luminosity spectrum. The luminosity spectrum is modelled by using the combined effect of three calculations, one for each component of the spectrum, which are described in the following section.

Initial State Radiation

Initial state radiation is calculated by using the `Pandora` Monte Carlo [66], which treats the electron energy distribution $f_{isr}(x)$ in a similar way to parton densities.

The probability of the initial state e^+e^- to emit collinear photons is much greater than the electromagnetic coupling constant α due to singularities in the Feynman integral. One solution is to treat the energy distribution of the electron emitting photons as a parton distribution. Fadin and Kuraev [67] suggested this method by solving for the distribution function by an expansion in

$$\beta = \frac{2\alpha}{\pi}\left(2\log\frac{2E_b}{m_e} - 1\right) \tag{4.13}$$

where E_b is the beam energy and m_e the rest mass of the electron.
`Pandora` uses the Skrzypek-Jadach approximation [64] which approximates the distribution function by

$$\begin{aligned} f_{isr}(x) \quad &= \frac{1}{2}\eta\left(1-x\right)^{\eta/2-1} \cdot \\ &\left(1+\frac{1}{2}\eta\right) e^{-\left(\eta+\left(\pi^2/6-1\right)\eta^2\right)/8}\left[\frac{1}{2}\left(1+x^2\right) - \frac{\eta}{8}\left(\frac{1}{2}\left(1+3x^2\right)\log x + \left(1-x\right)^2\right)\right] \end{aligned} \tag{4.14}$$

with

$$\eta = -6\log\left(1-\frac{1}{6}\beta\right), \tag{4.15}$$

where $f_{isr}(x)\,dx$ is the probability that an electron will have energy xE after initial state radiation. The Skrzypek-Jadach approximation is accurate to about 1%.

Beamstrahlung

The explicit calculation of beamstrahlung is very challenging, especially in high disruption colliders such as the ILC, due to the complicated multi-particle dynamics that occur when the bunches collide at the IP. It is therefore necessary to use simulation codes such as `Guinea-Pig++` [68] that compute the fields created at the IP due to the geometry and charge distribution of the bunches, and carry out tracking of the interacting particles to predict final state electron and photon energy distributions, energy loss distributions, backgrounds produced such as pair production and deflections of final state particles due to the fields of the interacting bunches at the IP.

`Guinea-Pig++` uses accelerator parameters, such as the β functions and RMS beam sizes at the IP, the number of particles per bunch and the energy spread of the beam, in order to compute the beamstrahlung spectrum of the particles producing luminosity.

It uses a macro-particle description of the bunch, by replacing the bunch particles (typically $\mathcal{O}(10^{10})$) with a smaller number of macro-particles (typically $\mathcal{O}(10^5)$). It

then divides the beams into slices, with each slice containing a number of macro-particles. The two bunches are brought together so that slices can sequentially interact. Only slices being at the same z-position interact with each other. For each interaction the fields of the beams are calculated, and the effects applied to the particles in that slice. After the interaction occurs, slices are moved forward to interact with the next slice. To calculate the fields, the slices are divided transversely into a grid of cells, and the fields are computed numerically by solving Poisson's equation for the potential at the grid points. The forces on the particles within the slices are computed according to the potential at the grid points. In this way, `Guinea-Pig++` simulates the dynamics of the collision by explicitly tracking particles through the bunch fields during collision, and applying energy loss due to beamstrahlung accordingly.

Figure 4.4 shows the beamstrahlung spectrum for the four different settings of the ILC operational parameter plane. It can be seen in this plot that different accelerator parameter settings give different beamstrahlung spectra, with the LowP and LargeY machine options exhibiting a much larger beamstrahlung than the Nominal and LowN options. A beam energy spread of 0.1% is included in the `Guinea-Pig++` calculation of all four beamstrahlung spectra.

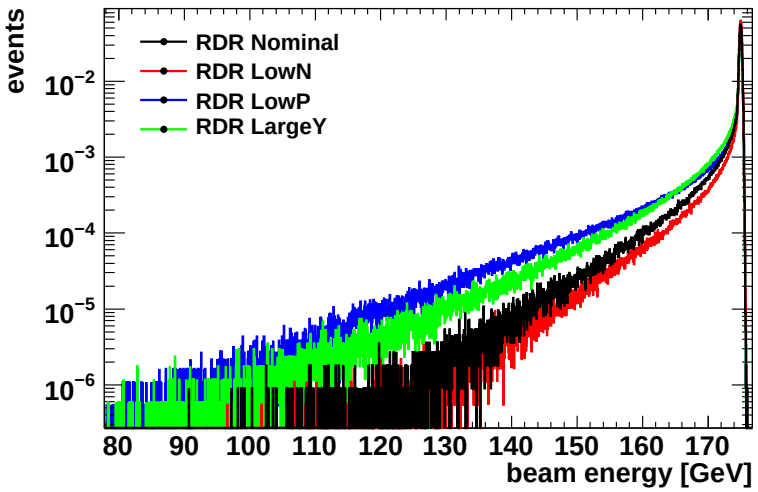

Figure 4.4: The beamstrahlung spectra, as computed with `Guinea-Pig++`, for the four different accelerator parameter settings defined in the ILC RDR operational parameter plane [27] (summarised in table 4.1). All spectra include a 0.1% beam energy spread and each spectrum corresponds to the amount of beamstrahlung averaged over 10 `Guinea-Pig++` runs with identical initial conditions.

Table 4.1 shows the parameters for the four different accelerator settings which mainly influence the amount of beamstrahlung radiation.

Table 4.1: Beam and IP parameters for the different settings of the ILC RDR operational parameter plane [27] that are related to beamstrahlung. Based on accelerator parameters of table 3.2.

Parameter	Symbol/Units	Nominal	Low-N	Large-Y	Low-P
Particles per bunch	N (10^{10})	2	1	2	2
Bunches per pulse	n_b	2625	5120	2625	1320
Beta function at IP	β_x^* (mm)	20	11	11	11
Beta function at IP	β_y^* (mm)	0.4	0.2	0.6	0.2
RMS beam size at IP	σ_x^* (nm)	639	474	474	474
RMS beam size at IP	σ_y^* (nm)	5.7	3.5	9.9	3.8
RMS bunch length	σ_z (μm)	300	200	500	200
Disruption parameter (x)	$\mathcal{D}_x$	0.17	0.11	0.52	0.21
Disruption parameter (y)	$\mathcal{D}_y$	19.4	14.6	24.9	26.1
Beamstrahlung parameter	$\langle\Upsilon\rangle$	0.048	0.050	0.038	0.097
Beamstrahlung energy loss	δ_{BS}	0.024	0.017	0.027	0.055

4.3.2 Beamstrahlung Parameterization and Fitting

The computation of beamstrahlung by `Guinea-Pig++` is very CPU and memory intensive, with its direct use proving inefficient for event generation and simulation studies. A parameterization of the `Guinea-Pig++` output is therefore needed in order to overcome these problems.

The beamstrahlung spectrum can be accurately described by using a parameterization of the form [69]

$$D_{e^\pm}(x) = a_0\delta(1-x) + a_1 x^{a_2}(1-x)^{a3} \tag{4.16}$$

where $D_{e^\pm}$ is the energy probability distribution with the Dirac $\delta-$function part representing the particles that have not radiated, and the second part of the function parameterizing the shape of the energy loss distribution by using a β-distribution functional form. The parameter x is defined as the fraction of a particle's energy over the nominal energy by using the transformation $x = E_b/E_n$ where E_b is the actual particle energy after radiation and E_n is its nominal energy. The free parameters for eq. 4.16 are a_0 describing the relative amount of particles that have not radiated, and a_2 and a_3 describing the shape of the energy loss. The parameter a_1 is a normalization condition such that the integral of eq. 4.16 equals 1. This is the formalism that was developed in the `Circe` code for parameterizing beam spectra [69].

However, this parameterization does not account for beam energy spread, which can significantly modify the peak position and shape of the beamstrahlung spectrum.

Furthermore, when fitting the beamstrahlung spectrum, `Circe` employs the mapping $x \to (1-x)^{1/5}$ to avoid the singularity in the β-function. BES on unradiated particles can lead to $x > 1$ values, making the mapping divergent.

To overcome these problems, a modified version of eq. 4.16 is used, by convoluting the original beamstrahlung function with a beamspread function such that

$$D^*_{e^\pm}(x) = a_0 BES(1,\sigma) + a_1 \int_0^{x_{max}} BES(x,\sigma) \cdot x^{a_2}(1-x)^{a3}\, dx \tag{4.17}$$

where x_{max} is the maximum fractional beam energy, σ is the amount and $BES(x,\sigma)$ the distribution of beam energy spread. For the purpose of this thesis beam energy spread is assumed to follow a Gaussian distribution **??**.

The integral of eq. 4.17 cannot be performed analytically because of the singularity in the β- distribution. Therefore numerical integration techniques must be used in the calculation of eq. 4.17. This is done by using Simpson's rule for numerical quadrature, by calculating 101 convolution steps, extending to $\pm 5\sigma$ of the energy spread width, for each value of x.

Now that the modified beamstrahlung function includes beam energy spread, it can be fitted to the `Guinea-Pig++` output in order to obtain a parameterization of the spectrum. The fitting is performed by using the fitting package `RooFit` [70]. This uses χ^2 minimization of the functional form of eq. 4.17 against the beamstrahlung spectrum histogram as generated by `Guinea-Pig++`. The fit is stable and converges quickly with a $\chi^2 \sim 1$ per degree of freedom. An example of the fitting function plotted over the beamstrahlung spectrum can be seen in the plot of figure 4.5.
Table 4.2 shows the beamstrahlung parameters extracted from fitting the distributions of figure 4.4 for the different ILC accelerator configurations. It also includes the average pre-collision beam energy, $\langle E \rangle$, to give an estimate of the actual energy loss due to beamstrahlung.

Table 4.2: Beamstrahlung fit parameters, for the ILC RDR parameter plane spectra of figure 4.4.

	Nominal	**Low-N**	**Large-Y**	**Low-P**
a_0	0.606	0.705	0.445	0.531
a_2	15.340	15.869	11.192	8.026
a_3	–0.708	–0.744	–0.690	–0.642
σ_E [GeV]	0.175	0.175	0.174	0.176
$\langle E \rangle$ [GeV]	173.58	174.05	172.26	171.62

To generate the beamstrahlung and beamspread distributions according to the

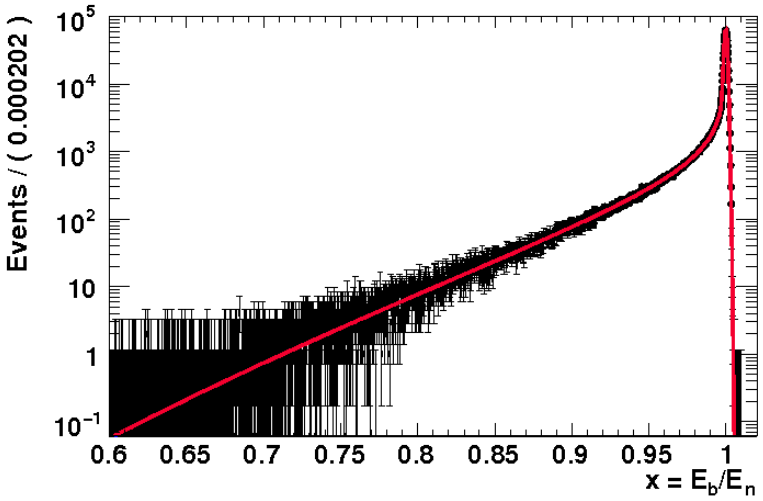

Figure 4.5: A sample fit of the function of eq. 4.17 to a `Guinea-Pig++` beamstrahlung spectrum including a Gaussian distributed beam energy spread with a σ of 0.1%. The histogram corresponds to the beamstrahlung spectrum for 10 `Guinea-Pig++` runs with identical initial conditions.

above parameterization, random number distributions from the GNU Scientific Library [71] are used. Using the GSL random number distributions for the generation of the β- function and the Gaussian distribution, with the set of beamstrahlung parameters as extracted from the fits, gives an accurate reproduction of the beamstrahlung spectrum. Figure 4.6 shows an example spectrum as calculated with `Guinea-Pig++` overlayed with a generated spectrum based on the parameterization of `Guinea-Pig++`. If the generated spectrum is fitted with the procedure described above, the fit extracts the same parameters as for the original `Guinea-Pig++` spectrum.

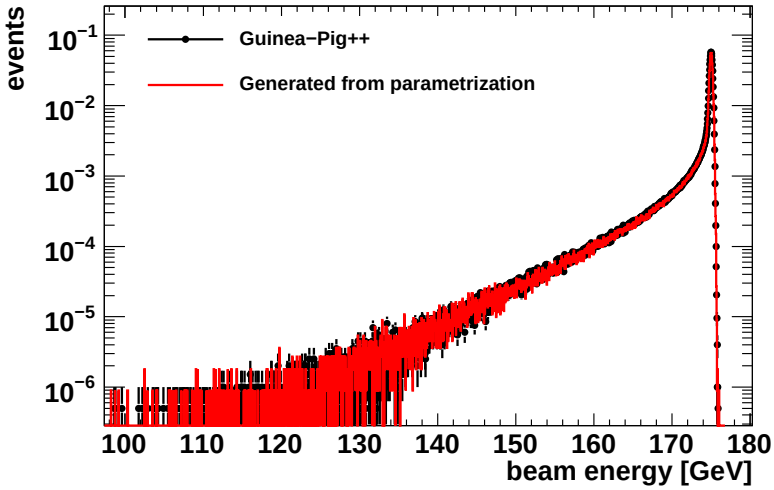

Figure 4.6: Plot showing a sample beamstrahlung spectrum as calculated from `Guinea-Pig++` overlayed with a generated spectrum based on the parameterization of the `Guinea-Pig++` simulation.

4.4 Measuring the Luminosity Spectrum

Simulation codes such as `Guinea-Pig++` alone cannot be relied upon for predictions of the beamstrahlung component of the luminosity spectrum. They must be verified against collision data. The luminosity spectrum can be measured by using the acollinearity of wide-angle Bhabha scattering events as measured in the detectors of the collider.

4.4.1 Bhabha Scattering

It has been long proposed that Bhabha scattering events can be used to extract the energy distribution of the colliding beams [72]. Bhabha scattering at lowest order takes place by s- and t-channel production. The tree-level Feynman diagrams for the two channels can be seen in figure 4.7. The t-channel diagram contribution scales as $d\sigma(e^+e^- \to e^+e^-)/d\cos\theta \propto 1/\theta^3$ which makes it divergent at zero angle but also enhances the cross-section significantly at low angles.

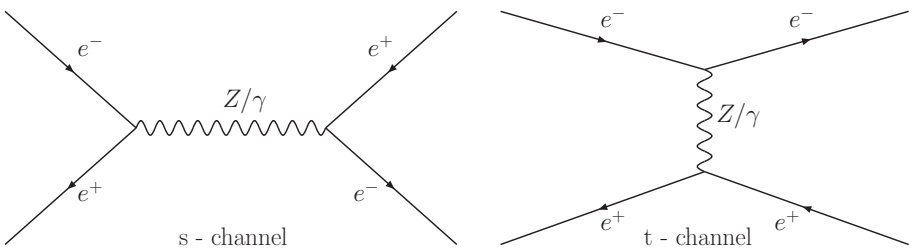

Figure 4.7: Lowest order Feynman diagrams for s- and t-channel Bhabha scattering.

The plot on the left of figure 4.8 shows the cross-section for Bhabha scattering as a function of centre-of-mass energy, with a minimum production angle of $\theta = 7°$ and the plot on the right of figure 4.8 shows the integrated cross-section at CMS of 350 GeV as a function of the minimum production angle.

By considering a reasonable low angle cut-off for the detector at $\theta > 7°$ due to tracker acceptance, the cross-section within the detector acceptance at $\sqrt{s}$= 350 GeV is 596 pb. This is about 600 times the $t\bar{t}$ cross-section, which is $\mathcal{O}$(1 pb), providing high statistics comparable to the signal process.

The method of measuring the luminosity spectrum from Bhabha scattering events uses the fact that in a two-fermion process, the mass of the system can be extracted with high precision just from the scattered fermion angles, given that only one beam has radiated collinear photons. This makes the system acollinear, and the mismatch in the momenta of the initial state particles can be calculated by using the acollinearity of the final state scattered particles.

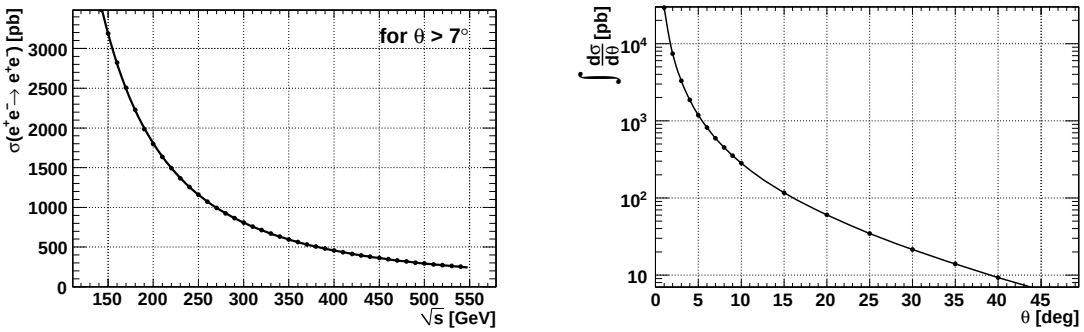

Figure 4.8: Total Bhabha scattering cross-section as a function of centre-of-mass energy (left), and integrated scattering cross-section at $\sqrt{s}$= 350 GeV as a function of scattering angle (right).

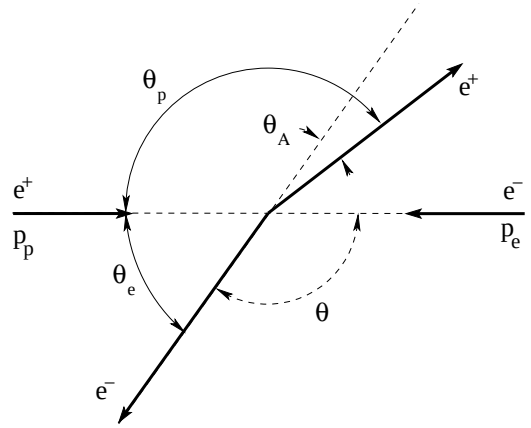

Figure 4.9: Schematic diagram of Bhabha scattering with single photon radiation. The scattering angles are defined as θ_e and θ_p and the acollinearity angle as θ_A.

To derive the formula for a variable sensitive to the centre-of-mass energy distribution based on outgoing fermion angles, we need to consider the diagram of figure 4.9. The centre-of-mass energy of a closed e^+e^- system can be defined as

$$s = |\mathbf{P_e} + \mathbf{P_p}|^2 = E_e^2 + E_p^2 + 2E_eE_p - p_e^2 - p_p^2 - 2\mathbf{p_e} \cdot \mathbf{p_p} \tag{4.18}$$

by neglecting the electron rest mass, we can write $E \approx p$, and so

$$s = 2E_eE_p - 2\mathbf{p_e} \cdot \mathbf{p_p} \tag{4.19}$$

$$= 2p_ep_p(1 - \hat{\mathbf{p_e}} \cdot \hat{\mathbf{p_p}}) \tag{4.20}$$

and in the approximation of symmetric collinear beams with no photons emitted, this becomes

$$\sqrt{s} = 2p_n \tag{4.21}$$

with p_n the nominal beam energy.

In the case of one beam emitting a collinear photon, using eq. 4.20, the effective centre-of-mass energy can be defined as

$$\sqrt{s'} = \sqrt{2p'_p p'_e(1-\cos(\theta_e+\theta_p))}, \tag{4.22}$$

with $p'_{e,p} = |\mathbf{p'_{e,p}}|$ the final state momenta of the electron and positron respectively. Therefore, an expression for the luminosity spectrum can be written using eq. 4.22 and 4.21 as

$$x = \frac{\sqrt{s'}}{\sqrt{s}} = \frac{\sqrt{2p'_p p'_e(1-\cos(\theta_e+\theta_p))}}{2p_n} \tag{4.23}$$

To express this only in terms of final state angles, let us consider the energy-momentum four-vector components of the entire e^+e^- system. With no photon emission these are given by

$$p_x = p_y = p_z = 0 \qquad E = 2p_n \tag{4.24}$$

These can be re-written in terms of final state four-vectors by using orthogonal components, and including single beam collinear photon emission, as

$$\begin{aligned}
p'_x &= p'_p\cos(\pi-\theta_P) - p_e\ \sin\left(\frac{\pi}{2}-\theta_e\right) - \Delta p \\
&= p'_p\cos\theta_e + p_e\ \cos\theta_p - \Delta p && (4.25)\\
p'_y &= p'_p\sin(\pi-\theta_p) - p_e\ \cos\left(\frac{\pi}{2}-\theta_e\right) \\
&= p'_p\sin\theta_p + p_e\ \sin\theta_e && (4.26)\\
p'_z &= 0 && (4.27)\\
E' &= p'_p + p'_e + \Delta p && (4.28)
\end{aligned}$$

with $\Delta p = |\Delta\mathbf{P}|$ the momentum carried away by the emitted photon(s).

Since the four-vector components of eqs. 4.24 to 4.28 are for the entire e^+e^- system including collinear photon(s), each component must conserve energy-momentum. Conservation of energy gives

$$2p_n = p'_p + p'_e + \Delta p \tag{4.29}$$

and conservation of momentum in the x and y directions respectively gives

$$\begin{aligned}
p'_p\cos\theta_p &+ p'_e\cos\theta_e - \Delta p = 0 && (4.30)\\
p'_p\sin\theta_p &+ p'_e\sin\theta_e = 0 && (4.31)
\end{aligned}$$

Using eqs. 4.29 to 4.31 we can re-arrange eq. 4.23 to be based solely on scattering angles, as

$$x = x_{\text{acol}} = \frac{\sqrt{2\sin\theta_e \sin\theta_p(1-\cos(\theta_e+\theta_p))}}{\sin\theta_p(1-\cos\theta_e)+\sin\theta_e(1-\cos\theta_p)} \tag{4.32}$$

Finally this can be simplified by using trigonometric identities to the standard expression for reconstructing the luminosity spectrum using only measured final state angles

$$x_{\text{acol}} = \sqrt{\cot\frac{\theta_e}{2}\cot\frac{\theta_p}{2}}\ . \tag{4.33}$$

Therefore, by precisely measuring the angles of the final state electron and positron in Bhabha scattering events, and provided that there is no multiple radiation from both the colliding electron and positron, one should be able to accurately extract the luminosity spectrum.

In the following sections we will discuss the simulation of this method with studies of possible systematic effects which could limit the accuracy of the measurement.

4.4.2 Simulation Method

Beamstrahlung and Bhabha Generation

To simulate Bhabha scattering, the `BHWIDE 1.04` Monte Carlo generator was used, which uses the YFS exponentiation technique to obtain $\mathcal{O}(\alpha)$ predictions of wide-angle Bhabha events with a precision of 1.5% [73]. A sample of 1788 k events was generated at a fixed centre-of-mass energy of 350 GeV, corresponding to approximately 3 fb^{-1} of luminosity, with a detector angular cut of $7^\circ < \theta_{e,p} < 173^\circ$. The cut-off angle is chosen as such for the events to be fully contained in the tracker of the detector. As a detector benchmark the TESLA detector [74] was used since the ILC detectors do not have finalized specifications for the forward tracking subsystems. In any case it is envisioned that forward tracking acceptance and resolution will be at least comparable, if not better, to the TESLA detector [75].

Beamstrahlung is included using the parameterization and generation procedure discussed in section 4.3.2. The Bhabha event total energy is scaled by $350/\sqrt{s'}$ and Lorentz boosted by $E_e - E_p$ to incorporate the effect of the luminosity spectrum. The events are weighted according to the variation of the cross-section with centre-of-mass energy. The angular and energy distributions of the events do not change significantly as a function of centre-of-mass energy, and so the assumption of generating the events at a fixed centre-of-mass energy and boosting/scaling by the luminosity spectrum is valid. This can be seen in the plots of figure 4.10 where the final state angular and

energy distributions of Bhabha events are shown as generated for three fixed centre-of-mass energies of 150, 250 and 350 GeV. It can be seen that there is no change in these distributions as a function of generation centre-of-mass energy.

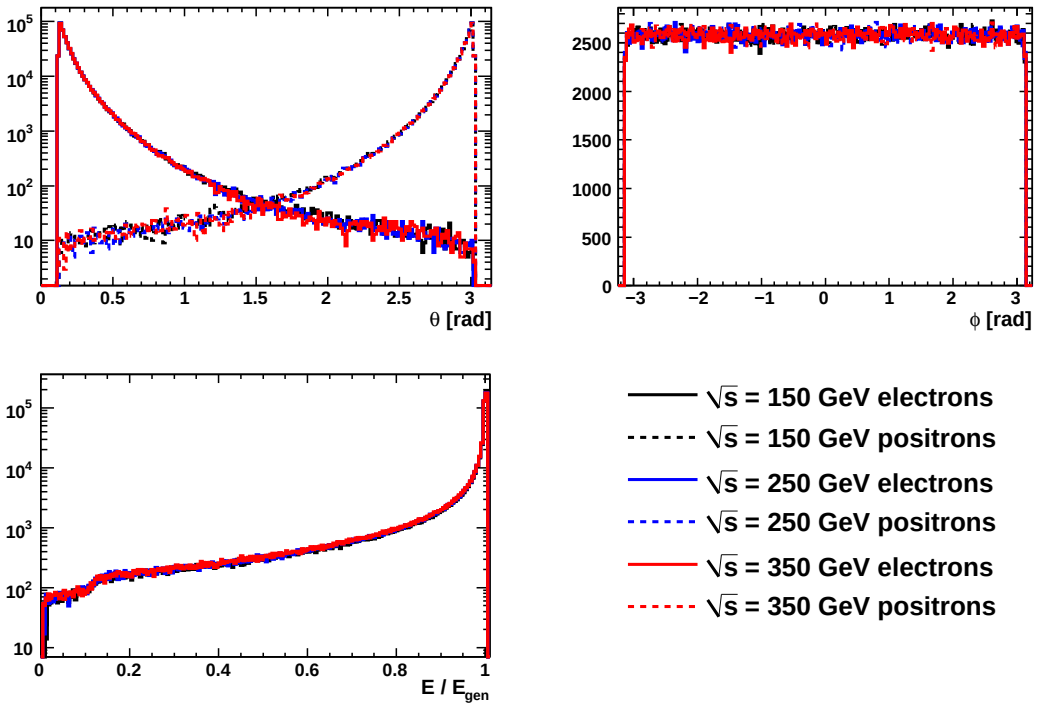

Figure 4.10: Final state distributions for scattering angles θ (top left) and ϕ (top right), and the scaled energy (bottom left) of Bhabha events generated at $\sqrt{s}$= 150, 250 and 350 GeV. The scaled energy E/E_{gen} is the energy of the final state particle divided by the beam energy used for the generation.

Fit Method

The extraction method is based on the fact that a good parameterization of the luminosity spectrum exists. By performing a fit of 'measured' x_{acol}^{meas} distribution and generated x_{acol}^{fit} distributions with variations in the beamstrahlung parameters ($a_0,\ a_2,\ a_3$), the 'measured' beamstrahlung parameters can be extracted [76]. For the generated distributions, it is assumed that the variation in beamstrahlung is linear in each bin of x for small variations around the default value of the beamstrahlung parameters ($a_0,\ a_2,\ a_3$), i.e. that linear interpolation between different bins can be used. Figure 4.11 shows the variation of the beamstrahlung spectrum with individual changes in the three a_i parameters.

The extraction method is complicated by the existence of beam energy spread. The assumption in eq. 4.33 is that by construction $\sqrt{s'} < \sqrt{s}$, however in the presence

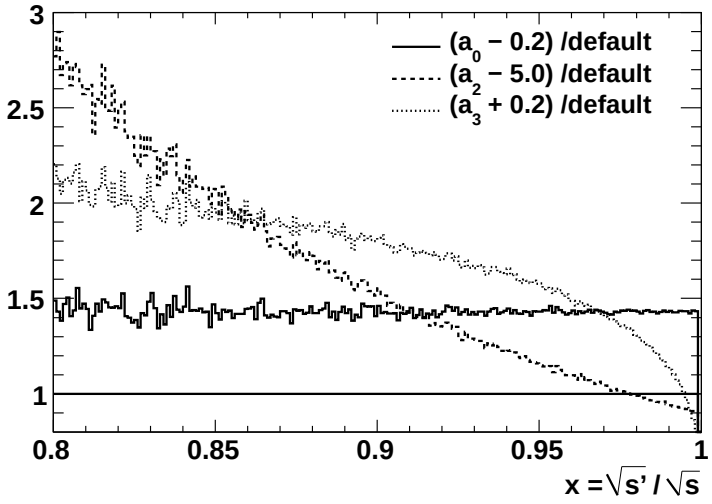

Figure 4.11: The variation of the beamstrahlung spectrum with respect to the default for individual changes in the three a_i parameters.

of beam energy spread if neither of the initial state particles have emitted hard radiation, the situation where $\sqrt{s'} > \sqrt{s}$ can arise. These events in the x_{acol} approximation will be folded around $\sqrt{s'}/\sqrt{s} = 1$ causing the effect seen in the plot of figure 4.12. It is impossible for this effect to be factorized out of the extraction, and so beam energy spread must be included in the fit.

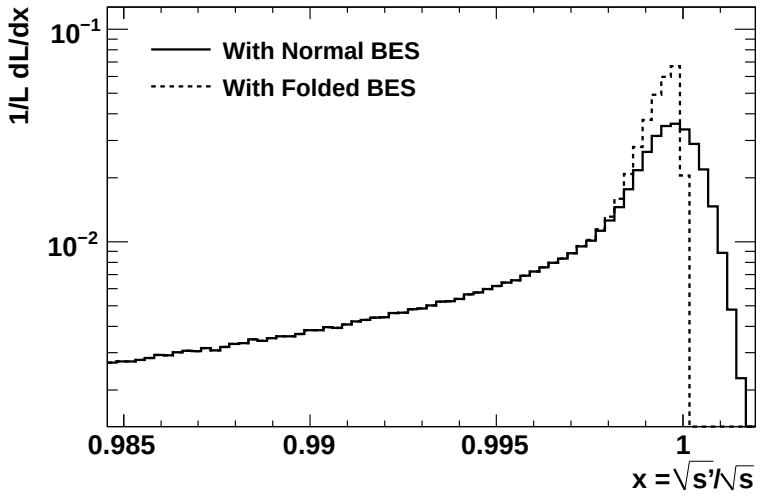

Figure 4.12: The effect of beam energy spread around the peak of the spectrum due to the folding caused by the reconstruction assumption $\sqrt{s'} < \sqrt{s}$.

Using the above assumptions, a collection of spectra with variations in the three a_i parameters and beam energy spread can be created, in order to form the fitting

function :

$$x_j^{fit}(a_0, a_2, a_3, a_\sigma) = x_j^0 + \sum_{i=0,2,3,\sigma} \frac{a_i - a_i^0}{\Delta a_i} \left(x_j^i - x_j^0\right) \tag{4.34}$$

with x^0 and a^0 the default parameters, and x and a the $x^0 + \Delta x$ and $a^0 + \Delta a$ respectively. The parameter a_σ is the amount of beam energy spread. Subscript j refers to a single bin of the beamstrahlung spectrum.

A standard χ^2 minimization between the data and the fit function is used :

$$\chi^2(a_0, a_2, a_3, a_\sigma) = \sum_{j=bins} \left(\frac{x_j^{meas} - x_j^{fit}(a_0, a_2, a_3, a_\sigma)}{\sigma_{meas}} \right)^2 . \tag{4.35}$$

If the fitting data are generated with the same parameters for 'measured' and fit spectra, then it has been verified that the fit returns the true values for a_i and a_σ for starting parameters several standard deviations away from the true value.

Table 4.3 summarizes the extracted fit values and associated statistical errors for a fit performed on a data sample of 1788k Bhabha events corresponding to 3 fb^{-1} of luminosity. The default beamstrahlung parameters for the Nominal ILC machine were used (see table 4.2), with the other three parameter sets giving similar statistical errors. The χ^2 in all the fits was ~ 1 per degree of freedom using uniformly binned histograms with 1000 bins each, indicating a good convergence of the fit function.

Table 4.3: Default fit parameters and associated statistical errors for a fit on a 1788 k Bhabha sample corresponding to 3 fb^{-1} of luminosity. The beamstrahlung spectrum used corresponds to the Nominal machine parameter set, with the other parameter sets giving similar results.

Parameter	**Default**	**Statistical Error**
a_0	0.606	0.081 %
a_2	15.340	0.087 %
a_3	-0.708	0.071 %
σ_x	0.001	0.180 %

The plots of figure 4.13 show the minimized fit function over the data and the χ^2 minimization for the three beamstrahlung parameters.

The results of the fit indicate that the fit method works well, with fast convergence in each of the fit parameters, and with the statistical error on the fit parameters being small (for the 3 fb^{-1} data sample).

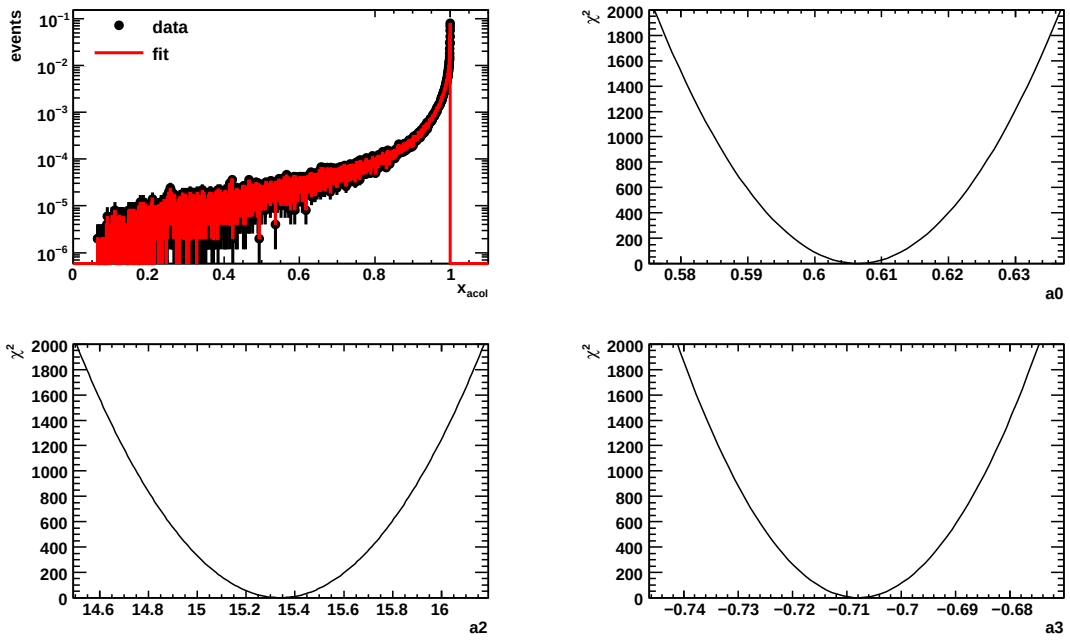

Figure 4.13: Minimized fit function (top left) and χ^2 minimization for the three beamstrahlung parameters.

The main assumptions of the extraction method are

- **No Correlations:** By using a parameterization to describe the beamstrahlung spectrum, it is assumed that there is no correlation in the energies of the colliding e^+ and e^-.

- **Symmetric Beams:** The beamstrahlung spectra of the two beams are assumed symmetric, with the same beamstrahlung parameters describing the shape of the spectra of both beams. This is because the acollinearity method can only extract one set of beamstrahlung parameters. Any difference in the beamstrahlung of the two beams will appear as a shift in the extracted beamstrahlung parameters.

- **Single Beam Radiation:** The assumption that only one beam has radiated one or more collinear photons is intrinsic to the acollinearity method. For high disruption colliders such as the ILC this assumption does not hold. The plot of figure 4.14 shows the x_{reco} reconstructed spectrum using the acollinearity method versus the x_{true} true spectrum[1] used to generate the events for reconstruction. It can be seen that there is a strong diagonal contribution, with a tail at $x_{\text{reco}} = 1$ arising from events where both beams have radiated. Even though

[1]The true x cannot be calculated unambiguously due to the overlap of initial state radiation (ISR) and final state radiation (FSR) computed in `BHWIDE`

most events are in the diagonal of the plot, there is some loss of information from the off-diagonal contributions.

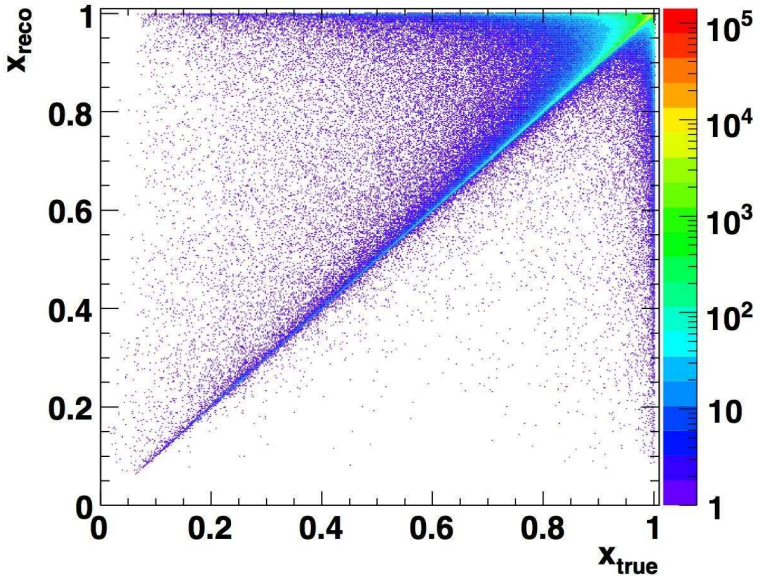

Figure 4.14: Reconstructed versus true x, for the Nominal ILC parameters.

4.5 Luminosity Spectrum Measurement Systematics

There are various systematic effects that can degrade the accuracy of the luminosity spectrum measurement. In this section, the effects of beam-beam interactions at the IP, and detector resolution will be examined to determine if they influence/limit the measurement accuracy.

4.5.1 Detector Resolution Effects

The main part of the detector influencing the accuracy of the Bhabha acollinearity measurement is the forward tracking subsystem. Its resolution directly affects the reconstruction of the scattering angles and hence the measured x_{acol} distribution.

The ILC detector forward tracking subsystems do not have finalized specifications yet, therefore the TESLA detector description is used as a benchmark for the tracking resolution needed. Figure 4.15 shows the forward tracking resolution of the TESLA detector as a function of angle, with an acceptance of $\theta > 7°$.

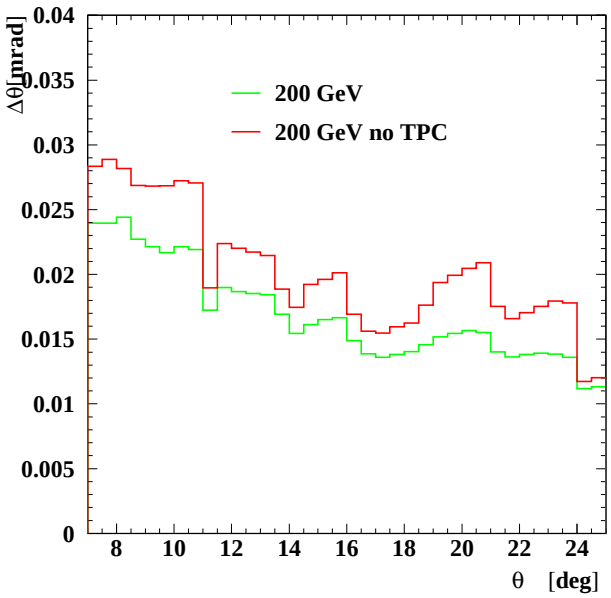

Figure 4.15: Polar angle resolution of the forward tracking system of the TESLA detector [76].

To study this effect in the simulation of the measurement, a Gaussian distributed smearing is applied to the scattering angles of the final state Bhabha events. To account for the worst case scenario in the tracking resolution of the detector, a smearing of $\sigma_{res} = 0.03$ mrad (from 4.15) was used in this study.

The shift in the extracted beamstrahlung parameters if the detector resolution smearing is included in the 'measured' data sample but not in the fit samples, indicating the maximum effect detector resolution could have, is shown in table 4.4.

Table 4.4: Systematic shift in beamstrahlung parameters due to smearing the 'measured' data sample with a Gaussian detector resolution of $\sigma = 0.03$ mrad. Default values and statistical errors are similar to table 4.3.

Detector Resolution Effect		
Parameter	**Shift**	**Percent Shift**
Δa_0	0.0025	0.4%
Δa_2	0.0636	0.4%
Δa_3	0.0017	0.2%
$\Delta \sigma_x$	$3 \cdot 10^{-5}$	3.0%
$\Delta \langle E \rangle$ [MeV]	6.8	0.004%

The systematic shift in the three beamstrahlung parameters is small with most of the effect of the detector resolution being absorbed in a shift in the fit value of beam energy spread since both these effects contribute as a Gaussian smearing.

This leads to a shift of the average beam energy $\langle E \rangle$ of 6.8 MeV in relation to the Nominal machine parameter set spectrum as listed in table 4.4. Detector resolution is independent of the amount of beamstrahlung and gives a similar effect for all four machine parameter settings.

The fit results of table 4.4 indicate a worst case scenario where the detector smearing is not taken into account at all in the fit function data samples. In reality it is anticipated that a goold description of the detector resolution (at the few percent level) will exist thus minimizing this effect.

4.5.2 Beam-Beam Effects

In high disruption colliders such as the ILC, beam-beam effects can significantly modify the final state angles of outgoing charged particles due to the strong magnetic fields developing when the two bunches interact. The diagram of figure 4.16 illustrates the effects of the bunch crossing on the outgoing final state fermions in a Bhabha scattering interaction.

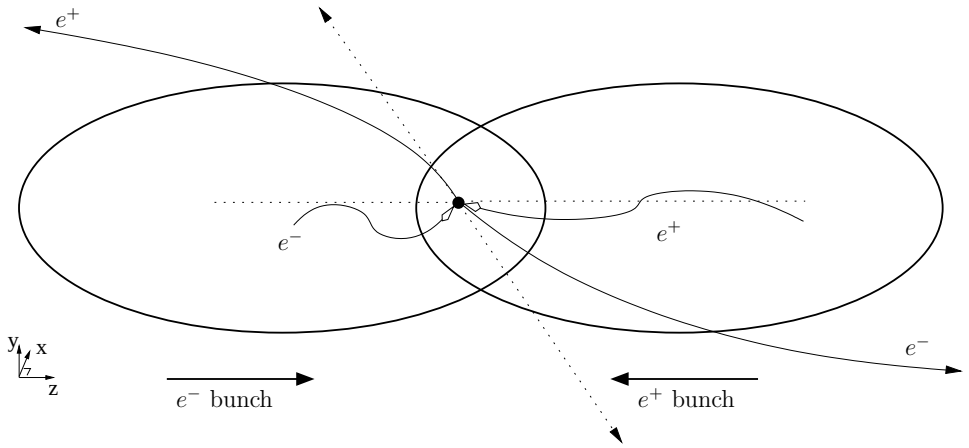

Figure 4.16: Schematic of the interaction of two bunches with a Bhabha scattering event produced. The dotted lines indicate the ideal initial and final state particles and the solid lines their path underlining the (magnified) effect due to the presence of the bunches.

Two major effects shown in this diagram are the transverse momenta of the initial state particles, and the change in trajectory of the final state particles, due to traversing the electromagnetic (EM) fields of the bunches.

To study beam-beam related systematic effects on the Bhabha acollinearity method, a full simulation of the bunch crossing and its effect on the Bhabha scatterers has to be used. To do this, a modified version of `Guinea-Pig++` is used where Bhabha events can be included in the bunch crossing simulation. `Guinea-Pig++` does this by randomly assigning Bhabha events in a macro-particle according to the calculated

luminosity and weighted probability of the Bhabha interaction occuring. It applies beamstrahlung and beamspread energy loss at the microscopic level and tracks the Bhabha events through the EM fields of the bunch. In this way, the effect of the bunch interaction on Bhabha scattering can be simulated at the microscopic level.

The beam-beam effects are studied by including them one by one in the simulation and examining the systematic shifts in the parameters of the measured beamstrahlung spectrum as extracted by the fit described in the previous section. This is done for all four accelerator parameter sets of table 4.1 in order to study how the beam parameters at the IP, and the different amounts of beamstrahlung radiation they produce, can influence the measurement of a physics process sensitive to the collision parameters.

Microscopic Beamstrahlung

One of the major effects of going from the simplified assumption of the parameterised beamstrahlung spectrum to a microscopic bunch crossing simulation for the 'measured' data, is that the assumption that beamstrahlung between the two beams is uncorrelated does not hold anymore.

Correlations should exist for at least two reasons [76] : The field experienced by a particle in the bunch depends on its transverse position within the bunch. For two particles to collide they should be in the same transverse position hence creating a correlation. In addition, particles colliding at the head of the bunch have had little chance of radiating while particles colliding at the tail of the bunch, having traversed the entire opposite bunch, have a higher probability of radiating. Thus the beamstrahlung spectrum should contain correlations in both the transverse and longitudinal planes.

The effect of using a parameterization of beamstrahlung versus the microscopic description can be studied by using the actual beamstrahlung spectrum as computed in `Guinea-Pig++` as the 'measured' data, and fitting it with the spectra computed by using the parameterized spectrum.

The results of the fits for the four accelerator parameter sets are summarized in table 4.5, where extracted values and shifts in the beamstrahlung parameters and average beam energy $\langle E \rangle$, relative to the default values of table 4.4, are shown. For the two low beamstrahlung cases of parameter sets Nominal and LowN, the shifts in the beamstrahlung parameters are small contributing a shift of a few MeV on the average beam energy, indicating that the Bhabha acollinearity method works well. In the high beamstrahlung cases of parameter sets LargeY and LowP, the shifts are much larger, with $\langle E \rangle$ shifts of 109.4 and 1070 MeV respectively. This shows

Table 4.5: Extracted values and shifts of the beamstrahlung parameters due to the effect of microscopic beamstrahlung on the 'measured' data sample. The shifts are relative to the default values of table 4.4.

Correlations Effect				
Parameter	**Nominal**	**LowN**	**LargeY**	**LowP**
a_0	0.623	0.712	0.463	0.597
a_2	15.669	16.347	11.549	8.257
a_3	-0.688	-0.727	-0.684	-0.717
σ_x	$1.0061 \cdot 10^{-3}$	$1.0001 \cdot 10^{-3}$	$1.0069 \cdot 10^{-3}$	$1.0080 \cdot 10^{-3}$
Δa_0	2.78%	2.25%	4.17%	12.40%
Δa_2	2.14%	3.01%	3.12%	2.87%
Δa_3	2.77%	2.18%	0.84%	-11.63%
$\Delta \sigma_x$	0.61%	0.01%	0.69%	0.80%
$\Delta \langle E \rangle$ [MeV]	-5.3	11.2	109.4	1070.0

the limitations imposed on the measurement of the luminosity spectrum due to the increased beamstrahlung, and is in accordance with the expectation expressed in the ILC RDR that these two machine parameter sets could potentially limit the physics performance of the collider [27].

The reason for the large shift in the high beamstrahlung scenario is attributed to the breakdown of the single beam radiation approximation of the acollinearity method. This is because in the high beamstrahlung cases it is more probable for particles in both beams to radiate photons leading to a bias of the extracted spectrum towards larger x_{acol} values. In the case of both beams radiating, the mismatch in the momentum of the final state Bhabha scatterers is smaller, causing them to be reconstructed at a larger x_{acol} value, as is shown in the plot of figure 4.14. This is in agreement with the results of table 4.5, where the larger the beamstrahlung, the larger the shift of the extracted spectrum towards large $\langle E \rangle$ values.

Final State EM Deflections

Another important effect is that of EM deflections on final state particles. After a Bhabha interaction has taken place, the final state particles need to traverse some of the bunch as they travel from their IP towards the detector. As they traverse the bunch, they will experience the bunch's EM fields and will be deflected from their nominal trajectory. The amount of deflection depends on the position the interaction takes place within the bunch and the production angle of the event. The more forward the event (θ approaching 0°), the more the deflection, because the final state particle

needs to traverse more of the bunch in order to exit the bunch and reach the detector.

Figure 4.17 shows the effect of EM deflections on Bhabha events produced with minimum cut-off angles of 1°, 4° and 7°. It can be seen that the more forward the events the larger the effect of the EM deflections on the final state scattering angles.

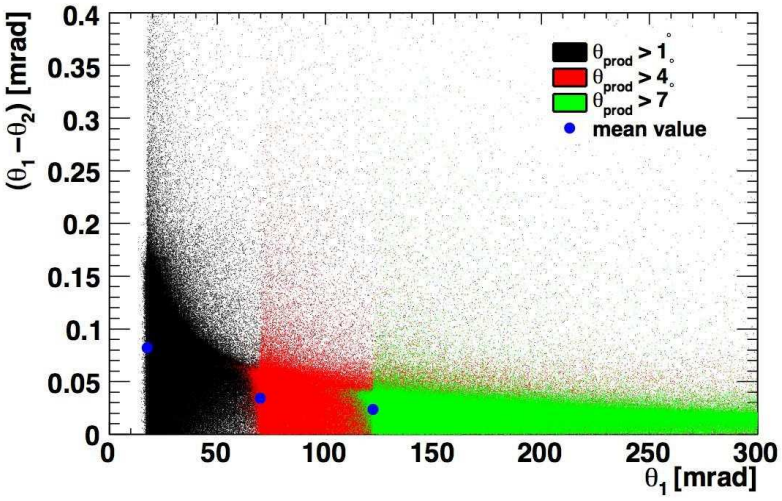

Figure 4.17: Plot of amount of deflection versus undeflected angles for different minimum Bhabha production angles. θ_2 is the scattering angle after deflection and θ_1 is before.

The field of the bunches causes a 'focusing' effect on the outgoing Bhabhas by causing a deflection of $\theta_2 < \theta_1$ to lower angles. The plot of figure 4.18 shows the distribution of the amount of deflection for Bhabhas produced at 7°. The amount of deflection is of the same order as the forward tracker resolution.

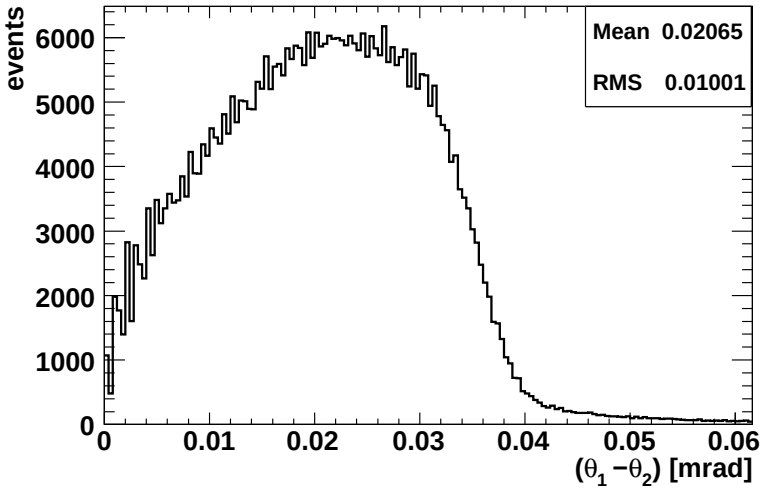

Figure 4.18: Distribution of the difference in the final state scattering angles due to the EM deflection effect for Bhabha events produced with a minimum angle of 7°.

The systematic shift in the beamstrahlung parameters due to EM deflections is shown in table 4.6. The 'measured' data for this were simulated using `Guinea-Pig++` (and hence with the correlation effect present) with only the EM deflections effect applied. It can be seen that the shifts in the beamstrahlung parameters are similar to the case above with just the correlations and hence final state EM deflections due to the fields developed at the IP do not significantly affect the luminosity spectrum measurement.

Table 4.6: Extracted values and shifts of the beamstrahlung parameters due to the effect of EM deflections on the final state Bhabha particles. The shifts are relative to the default values of table 4.4.

Final State EM Deflections Effect				
Parameter	**Nominal**	**LowN**	**LargeY**	**LowP**
a_0	0.623	0.721	0.463	0.597
a_2	15.657	16.352	11.535	8.256
a_3	-0.687	-0.727	-0.684	-0.717
σ_x	$1.0083 \cdot 10^{-3}$	$1.0001 \cdot 10^{-3}$	$1.0077 \cdot 10^{-3}$	$1.0083 \cdot 10^{-3}$
Δa_0	2.80%	2.25%	4.11%	12.27%
Δa_2	2.07%	3.04%	3.07%	2.86%
Δa_3	2.91%	2.21%	0.95%	-11.65%
$\Delta \sigma_x$	0.83%	0.01%	0.77%	0.83%
$\Delta \langle E \rangle$ [MeV]	-12.3	11.4	103.5	1083.9

Even though the EM deflections effect does not prove to be important in the case of measuring the luminosity spectrum using wide-angle Bhabha events, mainly due to the cut-off angle of 7° used, it could prove to have an effect on more forward events such as the low-angle Bhabha events used for the absolute luminosity measurement [77], the effect on increased deflection as a function of the minimum cut-off angle can be seen in the plot of figure 4.17.

Initial State Transverse Momentum

One of the assumptions leading to the derivation of the acollinearity formula of eq. 4.33 is that the initial state particles in the interaction have zero transverse momentum components ($p_x = p_y = 0$). However this is not the case in a realistic collision. Due to the interaction of the two bunches at the IP, the initial state e^+e^- can acquire transverse momentum components as they get tightly focused at the IP and traverse the opposing bunch before they collide. This is illustrated in the diagram of figure 4.16 by the curly lines showing the path of the initial state particles before the interaction.

This leads to a boost of the final state particles according to the transverse momentum (p_T) component of the initial state system which can change the final state acollinearity.

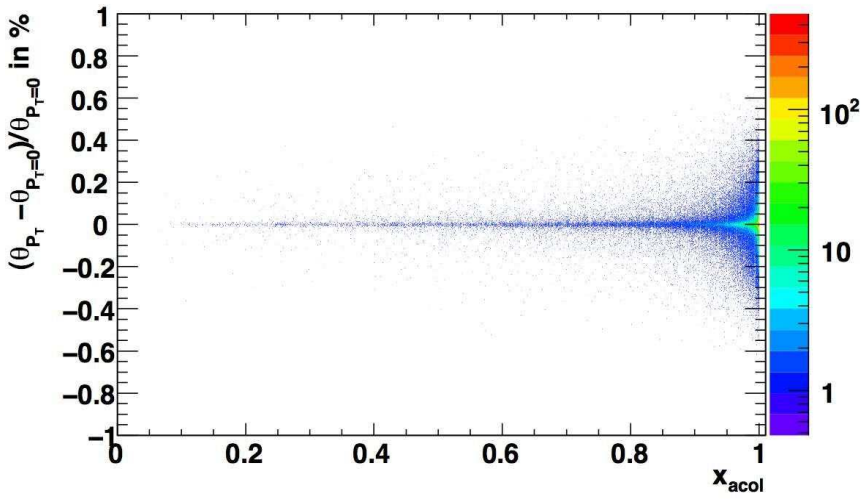

Figure 4.19: Difference in final state θ with and without the initial state transverse boost as a function of the acollinearity. θ_{P_T} are angles with transverse boost and $\theta_{P_T=0}$ are without.

The effect can be seen in the plot of figure 4.19 which shows the fractional change in the final state angles due to the transverse boost as a function of the acollinearity x_{acol}. In both cases the calculation is done using a modified version of `Guinea-Pig++` where the transverse boost effect was switched on and off. As expected, the fractional change in the final state angles gets larger at large x_{acol}, due to the smaller acollinearity there.

The plot of figure 4.20 shows the distribution of the difference in angles due to the transverse boost, and the plot of figure 4.21 shows the effect of the transverse boost on the reconstructed x_{acol}. The change in the final state scattering angles due to the transverse momentum components of the initial state system has a Lorentzian distribution shape with a RMS about 5 times larger than the detector resolution.

Table 4.7 shows the shifts in the beamstrahlung parameters due to the initial state transverse momentum effect. The 'measured' data samples used for the fits were calculated with `Guinea-Pig++` including the effect of microscopic beamstrahlung and initial state transverse boosts (but not final state EM deflections), and the 'fit' data samples used the standard parameterized luminosity spectrum description on the Bhabha samples.

For the Nominal, LowN and LargeY parameter sets, the shifts in the three beamstrahlung parameters a_0, a_2 and a_3 are comparable to those with only the microscopic

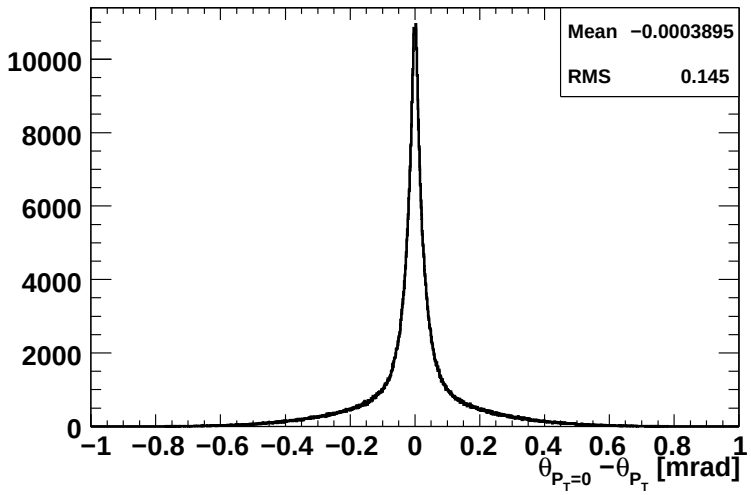

Figure 4.20: Distribution of the difference of the final state angles of Bhabha events due to the initial state transverse boost.

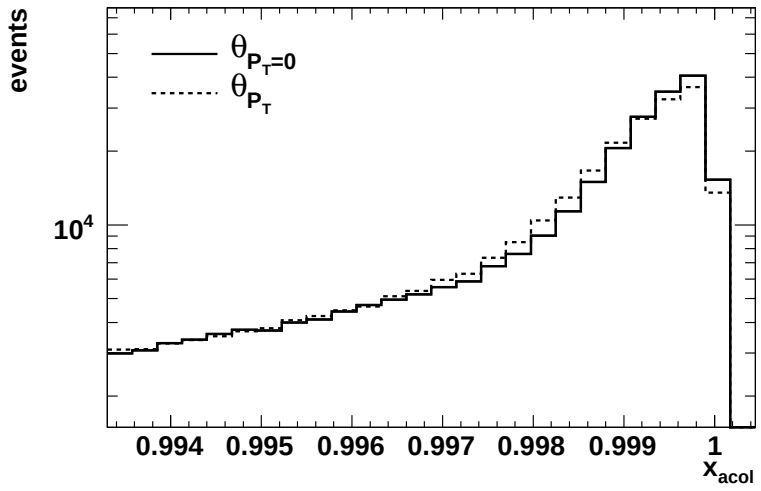

Figure 4.21: Transverse boost effect on the reconstructed x_{acol}.

beamstrahlung effect of table 4.5, indicating that the initial state transverse momentum does not significantly alter the shape of the measured luminosity spectrum. It does however alter the peak of the spectrum by shifting the fitted beam energy spread by a considerable amount (15–35%). This is because most of the change in acollinearity angles due to the transverse boosts is concentrated around the peak of the x_{acol} spectrum (as shown in figures 4.19 and 4.21) hence mainly influencing the extraction of beam energy spread.

Table 4.7: Extracted values and shifts in the beamstrahlung parameters due to the effect of the transverse momentum components of the initial state e^+e^-. The shifts are relative to the default values of table 4.4.

Initial State Transverse Momentum Effect				
Parameter	**Nominal**	**LowN**	**LargeY**	**LowP**
a_0	0.623	0.726	0.465	0.657
a_2	15.799	16.335	11.655	8.315
a_3	-0.685	-0.722	-0.683	-0.697
σ_x	$1.2503 \cdot 10^{-3}$	$1.1550 \cdot 10^{-3}$	$1.3400 \cdot 10^{-3}$	$1.3007 \cdot 10^{-3}$
Δa_0	2.71%	2.99%	4.61%	23.62%
Δa_2	2.99%	2.93%	4.14%	3.60%
Δa_3	3.28%	2.90%	1.08%	-8.60%
$\Delta \sigma_x$	25.03%	15.50%	34.00%	30.07%
$\Delta \langle E \rangle$ [MeV]	-7.5	7.8	124.5	1275.8

For the case of the LowP parameter set, representing the situation with the largest beamstrahlung, the fitted values show sizeable shifts relative to the case with only the microscopic beamstrahlung effect.

The average beam energy $\langle E \rangle$ shows small shifts of a few MeV compared to the default values of table 4.4 for the Nominal and LowN parameter sets. For the high beamstrahlung sets of LargeY and LowP parameter sets, the shifts are large, with 124.5 MeV for LargeY and 1275.8 MeV for LowP. This corresponds to a shift of about 25% relative to the case with only the microscopic beamstrahlung effect present (see table 4.5).

4.5.3 Conclusion

The performance of the measurement of the luminosity spectrum using the acollinearity of wide-angle Bhabha events was studied, by implementing a simulation of the measurement method and studying possible systematic effects that can affect the precision of the measurement.

According to these studies, it was shown that the measurement method works well by performing a fit for the beamstrahlung parameters between a 'measured' spectrum and a collection of 'fit' spectra. When no detector or beam-beam effects are present, the fit recovers the true beamstrahlung parameters for the fitted spectrum. The statistical errors on the fitted parameters for a data sample of 3 fb^{-1} are small compared to the possible systematic effects.

The inclusion of the detector resolution effect on the 'measured' data sample has a very small impact on the measured variables, indicating that the tracking resolution is not a limiting factor of the measurement.

The effect of the simplified form of the luminosity spectrum in the measurement method, and the effects of beam-beam interactions were studied by including the Bhabha scattering events in the bunch crossing simulations of `Guinea-Pig++`, and applying beamstrahlung and beam-beam effects at the microscopic level.

This results in small shifts in the measured luminosity spectrum parameters and average beam energy for the low beamstrahlung cases of the Nominal and LowN accelerator settings, of the order of ~ 10 MeV. In these two cases it is envisioned that the luminosity spectrum can be measured with adequate precision. For the higher beamstrahlung scenario of the LargeY accelerator setting, the measured luminosity spectrum has a larger shift, with the average beam energy shifted by approximately 125 MeV.

The measured spectrum for the LowP accelerator setting gives a relative shift in the average beam energy of approximately 1275 MeV, indicating that the extreme beamstrahlung scenario of this accelerator setting gives a large bias in the luminosity spectrum measurement.

In conclusion, this study demonstrates that the luminosity spectrum at the ILC can be measured with good precision by using the Bhabha acollinearity method, as long as the beamstrahlung at the IP is kept within the levels defined by the Nominal and LowN accelerator parameter sets. In higher beamstrahlung environments, the measurement is biased by large systematic effects attributed to the extreme beam-beam interactions at the IP, leading to large shifts in the measured beamstrahlung parameters.

4.6 Summary

In this chapter, the concept of the luminosity spectrum at a linear collider was examined, by first looking at the concepts of centre-of-mass energy and luminosity of the collider, and the methods by which they will be measured at the ILC. The way the luminosity spectrum arises through both beam-beam and accelerator related effects was described, and a detailed parameterization was developed in order to be able to describe the simulation outcome of beam-beam dedicated programs such as `GuineaPig++`. The default ILC RDR accelerator parameter plane was fitted with our parametrization, and the beamstrahlung fit parameters for each of the four different accelerator settings were obtained.

The method of measuring the luminosity spectrum through the use of Bhabha events was described, and a detailed description of the simulation and fitting methods was given, explaining all the assumptions used. Then the possible luminosity spectrum measurement systematics were examined by looking at the way that beam-beam effects and the detector resolution can affect the luminosity spectrum measurement. This was done for all four settings of the ILC operational parameter plane. The results of this study showed that the Bhabha scattering method for measuring the luminosity spectrum for the two 'low' beamstrahlung scenarios (Nominal and LowN) is only affected at the ~ 10 MeV level when looking at the total shift of the measured average energy of the luminosity spectrum compared to the true one. At the increased beamstrahlung scenario LargeY, this effect becomes approximately 125 MeV, and at the extreme beamstrahlung scenario of the LowP setting, the average beam energy is shifted by approximately 1275 MeV with large shifts in the measured beamstrahlung parameters, leading to a large bias in the luminosity spectrum measurement.

Chapter 5

The Top Quark Threshold

"[...] the $t\bar{t}$ threshold region may be identified as the long-sought "hydrogen atom of the strong interaction" [...]"

Matthew J. Strassler and Michael E. Peskin [78]

5.1 Introduction

The top quark production threshold at an e^+e^- linear collider offers a unique QCD environment, well suited for precision measurements of the top quark properties. This is both due to the clean experimental environment of a linear collider, and the unique attributes (see below) of the top quark threshold, which allow precise perturbative QCD calculations to take place. One of the virtues of the top quark threshold is that the behaviour of some of the main observables in the threshold region, like the cross-section, the top momentum distribution and the forward-backward asymmetry, are highly correlated to the mass of the top quark M_t, its width Γ_t, and the strong coupling constant α_s. Thus by measuring these observables as a function of the centre-of-mass energy, one can precisely measure the top quark parameters.

For the precise measurement of the top quark parameters, a very accurate theoretical description of the top quark threshold has to exist. Over the past 20 years this has been the subject of extensive research (e.g. [79, 78, 80, 37, 36, 81, 82]), with many important advancements in the theoretical description of the process. However, most of these calculations have not yet been fully utilized in experimental studies.

In the first half of this chapter, a brief review of the theoretical framework of the QCD calculations used in the later parts of this thesis will be given, focusing in

particular on the aspects that will be used in the next chapter for the implementation of these calculations into a simulation of the top production threshold.

The second half of the chapter will focus on the implementation of the calculations of the threshold observables, describing the techniques used for their realistic implementation in experimental studies, studying the dependence of the observable distributions on the top quark parameters, and describing some of the limiting factors in these studies, that will then be addressed in chapter 6.

5.2 Green Functions, Cross-Sections and Distributions

In e^+e^- collisions, top quarks are produced in pairs via the process $e^+e^- \rightarrow t\bar{t}$, mediated by a virtual photon γ^* or Z^0 boson, as can be seen in the Feynman diagram of figure 2.8.

The top quark decays via the weak interaction into a W boson and a b-quark. Due to the large top quark width $\Gamma(t \rightarrow bW) = \frac{G_F}{\sqrt{2}}\frac{M_t^3}{8\pi} \approx 1.5$ GeV the $t\bar{t}$ pair decays before it can hadronize, allowing for a fully perturbative treatment of the QCD calculation.

At its production threshold $\sqrt{s} \approx 2M_t \approx 350$ GeV, the $t\bar{t}$ pair moves with non-relativistic velocities $v = \sqrt{1 - 4M_t^2/s} << 1$. Because of this, the physical scales governing the $t\bar{t}$ dynamics, given by the top quark mass M_t, its momentum $M_t v$ and kinetic energy $\frac{1}{2}M_t v^2$, are widely separated, causing a break-down of the standard multi-loop expansion in α_s, due to singular terms arising of the form (α_s/v).

This is solved in the framework of effective field theories by using the hierarchy $M_t \gg M_t v \gg M_t v^2 > \Gamma_t \gg \Lambda_{QCD}$, with Λ_{QCD} defining the perturbative regime of QCD, and performing the perturbative calculation by using a double expansion in α_s and v. This leads to a non-relativistic formulation of QCD (NRQCD), in which the top quark production threshold can be described by the time-independent Schrödinger equation containing an instantaneous potential [79, 78, 37]. The solutions of the Schrödinger equation are given in the form of scattering wave amplitudes, from which one can obtain the total cross-section via the optical theorem.

In this section, the basic principles behind the calculation of the $t\bar{t}$ properties at threshold are discussed, illustrating how the quantities used in the later parts of this thesis arise in these calculations. For a detailed account of the calculation, the interested reader should refer directly to [37].

5.2.1 Non-Relativistic QCD

NRQCD is an effective theory of QCD formulated for non-relativistic heavy quark-antiquark systems [83, 84]. It is based on the separation of the physical scales governing the dynamics of the QCD system by separating out the low momentum scales $M_t v$ and $M_t v^2$ which describe the non-relativistic quark-antiquark dynamics from the high momentum scale M_t which describes the hard effects between the quarks and gluons.

For the $t\bar{t}$ threshold, the NRQCD Lagrangian can be obtained from the full QCD Lagrangian by integrating out all hard momentum effects contributing to quark-antiquark or quark-gluon terms of order M_t. This leads to a Lagrangian of the form [37] :

$$
\begin{aligned}
\mathcal{L}_{\text{NRQCD}} \;=\; & -\frac{1}{2}\,\text{Tr}\, G^{\mu\nu} G_{\mu\nu} + \sum_{q=u,d,s,c,b} \bar{q}\, i\not{D}\, q \\
& + \psi^\dagger \Big[iD_t + c_2\,\frac{\boldsymbol{D}^2}{2\,M_t} + c_4\,\frac{\boldsymbol{D}^4}{8\,M_t^3} + \ldots \\
& + \frac{c_F\,g_s}{2\,M_t}\,\boldsymbol{\sigma}\cdot\boldsymbol{B} + \frac{c_D\,g_s}{8\,M_t^2}\,(\,\boldsymbol{D}\cdot\boldsymbol{E} - \boldsymbol{E}\cdot\boldsymbol{D}\,) + \frac{c_S\,g_s}{8\,M_t^2}\,i\,\boldsymbol{\sigma}\,(\,\boldsymbol{D}\times\boldsymbol{E} - \boldsymbol{E}\times\boldsymbol{D}\,) + \ldots \Big]\,\psi \\
& + \chi^\dagger \Big[iD_t - c_2\,\frac{\boldsymbol{D}^2}{2\,M_t} - c_4\,\frac{\boldsymbol{D}^4}{8\,M_t^3} + \ldots \\
& - \frac{c_F\,g_s}{2\,M_t}\,\boldsymbol{\sigma}\cdot\boldsymbol{B} + \frac{c_D\,g_s}{8\,M_t^2}\,(\,\boldsymbol{D}\cdot\boldsymbol{E} - \boldsymbol{E}\cdot\boldsymbol{D}\,) + \frac{c_S\,g_s}{8\,M_t^2}\,i\,\boldsymbol{\sigma}\,(\,\boldsymbol{D}\times\boldsymbol{E} - \boldsymbol{E}\times\boldsymbol{D}\,) + \ldots \Big]\,\chi\,,
\end{aligned}
\tag{5.1}
$$

where only terms relevant to the NNLO computation of [37] are shown, and summation over all colour states is assumed.

The first two terms in eq. 5.1 are the standard relativistic gluonic and quark fields with $G^{\mu\nu}$ being the gluon field strength tensor, and q the Dirac spinor for massless quarks. The remaining terms are the interaction terms describing the dynamics of the non-relativistic $t\bar{t}$ pair with the Pauli spinors ψ and χ corresponding to the t and $\bar{t}$ quark respectively. $\boldsymbol{\sigma}$ is the Pauli spin matrix . The terms $\boldsymbol{E}$ and $\boldsymbol{B}$ correspond to the electric and magnetic components of the gluon field strength tensor and D_t and $\boldsymbol{D}$ to the time and space components of the gauge covariant derivative D_μ.

The c_2, c_4, c_F, c_D, c_S are short-distance coefficients[1] encoding the effects due to quark and gluon momenta of order $\geq M_t$.

[1]The explicit definition and calculation of the short-distance coefficients at NNLO can be found in Appendix A of [37].

Following the same formalism, the NNLO NRQCD currents can be defined for the vector and axial-vector contributions that can produce and annihilate the $t\overline{t}$ pair at threshold as [37] :

$$\tilde{j}^v_k(q) = c^v_1 \left(\tilde{\psi}^\dagger \sigma_k \tilde{\chi}\right)(q) - \frac{c^v_2}{6M_t^2}\left(\tilde{\psi}^\dagger \sigma_k (-\tfrac{i}{2}\overleftrightarrow{\boldsymbol{D}})^2 \tilde{\chi}\right)(q) + \dots , \tag{5.2}$$

$$\tilde{j}^v_k(-q) = c^v_1 \left(\tilde{\chi}^\dagger \sigma_k \tilde{\psi}\right)(-q) - \frac{c^v_2}{6M_t^2}\left(\tilde{\chi}^\dagger \sigma_k (-\tfrac{i}{2}\overleftrightarrow{\boldsymbol{D}})^2 \tilde{\psi}\right)(-q) + \dots , \tag{5.3}$$

for the QCD vector current ($j^v_\mu = \bar{t}\gamma_\mu t$) given in terms of the S-wave spin triplet ${}^3S_1$ NRQCD currents.
The axial-vector QCD current ($j^a_\mu = \bar{t}\gamma_\mu\gamma_5 t$) in terms of the P-wave spin triplet ${}^3P_1$ NRQCD currents is given by

$$\tilde{j}^a_k(q) = \frac{c^a_1}{M_t}\left(\tilde{\psi}^\dagger (-\tfrac{i}{2}\overleftrightarrow{\boldsymbol{D}}\times\boldsymbol{\sigma})_k \tilde{\chi}\right)(q) + \dots , \tag{5.4}$$

$$\tilde{j}^a_k(-q) = \frac{c^a_1}{M_t}\left(\tilde{\chi}^\dagger (-\tfrac{i}{2}\overleftrightarrow{\boldsymbol{D}}\times\boldsymbol{\sigma})_k \tilde{\psi}\right)(-q) + \dots , \tag{5.5}$$

where $\sqrt{q^2}$ is the available centre-of-mass energy[2], and $c^v_{1,2}$ and c^a_1 are the corresponding vector and axial-vector current short-distance coefficients.

From the NRQCD currents, one can form an expression for the total cross-section for $t\overline{t}$ production at threshold by using the optical theorem. This leads to the vector and axial-vector current induced cross-sections having the form :

$$R^v(q^2) = \frac{4\,\pi}{q^2}\,\mathrm{Im}\left[\,-i\,\langle\,0\,|T\,\tilde{j}^v_i(q)\,\tilde{j}^{v\,i}(-q)\,|\,0\,\rangle\,\right], \tag{5.6}$$

$$R^a(q^2) = \frac{4\,\pi}{q^2}\,\mathrm{Im}\left[\,-i\,\langle\,0\,|T\,\tilde{j}^a_i(q)\,\tilde{j}^{a\,i}(-q)\,|\,0\,\rangle\right]. \tag{5.7}$$

where T is the time-ordering operator. Putting eqs. 5.2 to 5.5 into eqs. 5.6 and 5.7, one can write the explicit expressions for the NRQCD NNLO cross-sections as [37] :

$$R^v_{\mathrm{NNLO}}(q^2) = \frac{4\,\pi}{q^2}\,C^v\,\mathrm{Im}\Big[\,\mathcal{A}^v(q^2)\,\Big] + \dots , \tag{5.8}$$

$$R^a_{\mathrm{NNLO}}(q^2) = \frac{4\,\pi}{q^2}\,C^a\,\mathrm{Im}\Big[\,\mathcal{A}^a(q^2)\,\Big] + \dots , \tag{5.9}$$

[2]Following the notation of [37].

where $\mathcal{A}^v$ and $\mathcal{A}^a$ are the vector and axial-vector current correlators, given by

$$\mathcal{A}^v = i \left\langle 0 \left| \left(\tilde{\psi}^\dagger \vec{\sigma}\, \tilde{\chi} + \frac{1}{6M_t^2} \tilde{\psi}^\dagger \vec{\sigma}\, (-\tfrac{i}{2} \overleftrightarrow{\boldsymbol{D}})^2 \tilde{\chi} \right) \left(\tilde{\chi}^\dagger \vec{\sigma}\, \tilde{\psi} + \frac{1}{6M_t^2} \tilde{\chi}^\dagger \vec{\sigma}\, (-\tfrac{i}{2} \overleftrightarrow{\boldsymbol{D}})^2 \tilde{\psi} \right) \right| 0 \right\rangle \tag{5.10}$$

$$\mathcal{A}^a = i \left\langle 0 \left| \left(\tilde{\psi}^\dagger (-\tfrac{i}{2} \overleftrightarrow{\boldsymbol{D}} \times \boldsymbol{\sigma})\, \tilde{\chi} \right) \left(\tilde{\chi}^\dagger (-\tfrac{i}{2} \overleftrightarrow{\boldsymbol{D}} \times \boldsymbol{\sigma})\, \tilde{\psi} \right) \right| 0 \right\rangle \tag{5.11}$$

and $C^v = (c_1^v)^2$ and $C^a = 1$ are the vector and axial-vector short distance coefficients. The total cross-section $\sigma_{tot}^{\gamma,Z}(e^+e^- \to \gamma^*, Z^* \to t\bar{t})$ can now be expressed in terms of the R^v and R^a as

$$\begin{aligned} \sigma_{tot}^{\gamma,Z}(q^2) &= \sigma_{pt} \left[Q_t^2 - 2\, \frac{q^2}{q^2 - M_Z^2}\, v_e\, v_t\, Q_t + \left(\frac{q^2}{q^2 - M_Z^2} \right)^2 \left[v_e^2 + a_e^2 \right] v_t^2 \right] R^v(q^2) \\ &\quad + \sigma_{pt} \left(\frac{q^2}{q^2 - M_Z^2} \right)^2 \left[v_e^2 + a_e^2 \right] a_t^2\, R^a(q^2)\,, \end{aligned} \tag{5.12}$$

with the point-like cross-section, and the vector and axial-vector fermion couplings given respectively by

$$\sigma_{pt} = \frac{4\,\pi\,\alpha^2}{3\,q^2}\,, \tag{5.13}$$

$$v_f = \frac{T_3^f - 2\,Q_f\,\sin^2\theta_W}{2\,\sin\theta_W\,\cos\theta_W}\,, \tag{5.14}$$

$$a_f = \frac{T_3^f}{2\,\sin\theta_W\,\cos\theta_W}\,. \tag{5.15}$$

where α is the fine structure constant, Q_f the electric charge of fermion f, θ_W the Weinberg angle, and T_3^f the third component of the weak isospin.

Therefore, in order to obtain predictions for the total cross-section one needs to calculate the non-relativistic current correlators $\mathcal{A}^v$ and $\mathcal{A}^a$. In the context of [37], this is done by deriving an equation of motion describing the top quark dynamics, which in the non-relativistic limit can be done by using a two-body Schrödinger equation with an instantaneous potential.

5.2.2 Green Functions and the Schrödinger Equation

The non-relativistic current correlators $\mathcal{A}^v$ and $\mathcal{A}^a$ can, in principle, be calculated using Feynman rules based on the NRQCD Lagrangian of eq. 5.1. This would, however, lead to the need of resumming an infinite amount of Feynman diagrams, making the method impractical for realistic calculations.

It turns out that the most practical way of calculating $\mathcal{A}^v$ and $\mathcal{A}^a$ is by deriving an equation of motion for the off-shell top quark four point Green function, which in the non-relativistic limit can be described by a two-body Schrödinger equation.

The Green function $\tilde{G}(\boldsymbol{k},\boldsymbol{k'};q^2)$ of the Schrödinger equation, describing the off-shell elastic scattering of a $t\bar{t}$ pair with centre-of-mass three momentum $\pm\boldsymbol{k}$ into a $t\bar{t}$ pair with three momentum $\pm\boldsymbol{k'}$, is given by [37]

$$\Big[\,\frac{\boldsymbol{k}^2}{M_t}-\frac{\boldsymbol{k}^4}{4M_t^3}\,-\,\Big(\,\frac{p_0^2}{M_t}-\frac{p_0^4}{4M_t^3}\,\Big)\,-\,i\,\Gamma_t\,\Big(\,1-\frac{\boldsymbol{k}^2}{2\,M_t^2}\,\Big)\,\Big]\,\tilde{G}(\boldsymbol{k},\boldsymbol{k'};q^2)$$

$$+\int\frac{d^3\boldsymbol{p'}}{(2\,\pi)^3}\,\tilde{V}(\boldsymbol{k},\boldsymbol{p'})\,\tilde{G}(\boldsymbol{p'},\boldsymbol{k'};q^2)\;=\;(2\,\pi)^3\,\delta^{(3)}(\boldsymbol{k}-\boldsymbol{k'}) \tag{5.16}$$

where the term p_0 corresponds to the centre-of-mass three momentum of the top quarks, and $\tilde{V}$ is the instantaneous potential of the interaction. The tilde in the terms $\tilde{V}$ and $\tilde{G}$ indicates that these terms only describe the potential quarks and ultrasoft gluonic degrees of freedom according to the NRQCD factorization theorem of [83, 84].

By using partial wave decomposition of the Green functions

$$\tilde{G}(\boldsymbol{k},\boldsymbol{k'};q^2)\;\;=\;\;\sum_{l=0}^{\infty}\tilde{G}^l(\boldsymbol{k},\boldsymbol{k'};q^2) \tag{5.17}$$

with l being the angular momentum quantum number, one can arrive at the relation of the Green functions of the Schrödinger equation to the NRQCD current correlators $\mathcal{A}^v$ and $\mathcal{A}^a$ for the S- and P-wave terms (corresponding to the vector and axial-vector contributions respectively) to be given by

$$\mathcal{A}^v(q^2)\;\;=\;\;6\,N_c\int\frac{d^3\boldsymbol{k}}{(2\pi)^3}\int\frac{d^3\boldsymbol{k'}}{(2\pi)^3}\,\Big(1+\frac{\boldsymbol{k}^2}{6M_t^2}\Big)\tilde{G}^0(\boldsymbol{k},\boldsymbol{k'})\,\Big(1+\frac{\boldsymbol{k'}^2}{6M_t^2}\Big) \tag{5.18}$$

$$\mathcal{A}^a(q^2)\;\;=\;\;4\,N_c\int\frac{d^3\boldsymbol{k}}{(2\pi)^3}\int\frac{d^3\boldsymbol{k'}}{(2\pi)^3}\,\frac{\boldsymbol{k}\boldsymbol{k'}}{M_t^2}\,\tilde{G}^1(\boldsymbol{k},\boldsymbol{k'}) \tag{5.19}$$

where the energy argument of the Green functions is dropped for simplicity.

By defining the S- and P-wave vertex Green functions as

$$S(\boldsymbol{k})\;\;=\;\;\int\frac{d^3\boldsymbol{p'}}{(2\,\pi)^3}\,\tilde{G}^0(\boldsymbol{k},\boldsymbol{p'})\,\Big(\,1+\frac{\boldsymbol{p'}^2}{6M_t^2}\,\Big)\,, \tag{5.20}$$

$$P(\boldsymbol{k})\;\;=\;\;\int\frac{d^3\boldsymbol{p'}}{(2\,\pi)^3}\,\frac{\boldsymbol{k}\boldsymbol{p'}}{\boldsymbol{k}^2}\,\tilde{G}^1(\boldsymbol{k},\boldsymbol{p'})\,, \tag{5.21}$$

one can obtain the solutions of the Schrödinger equation in terms of the S- and P-wave integral equations given by

$$S(\boldsymbol{k}) \;=\; G^f(\boldsymbol{k})\left(1+\frac{\boldsymbol{k}^2}{6M_t^2}\right) \;-\; G^f(\boldsymbol{k})\int\frac{d^3\boldsymbol{p}'}{(2\pi)^3}\,\tilde{V}(\boldsymbol{k},\boldsymbol{p}')\,S(\boldsymbol{p}')\,, \tag{5.22}$$

$$P(\boldsymbol{k}) \;=\; G^f(\boldsymbol{k}) \;-\; G^f(\boldsymbol{k})\int\frac{d^3\boldsymbol{p}'}{(2\pi)^3}\,\frac{\boldsymbol{k}\boldsymbol{p}'}{\boldsymbol{k}^2}\,\tilde{V}_c^{\rm LO}(\boldsymbol{k},\boldsymbol{p}')\,P(\boldsymbol{p}') \tag{5.23}$$

with

$$G^f(\boldsymbol{k}) = \frac{M_t}{\boldsymbol{k}^2-p_0^2-\frac{\Gamma_t^2}{4}-i\,M_t\,\Gamma_t}\left[1+\frac{\boldsymbol{k}^2+p_0^2}{4\,M_t^2}-i\,\frac{\Gamma_t}{4\,M_t}\right] \tag{5.24}$$

being the free vertex function.

The $\tilde{V}$ term in eq. 5.22 corresponds to the full NNLO NRQCD instantaneous potential while the term $\tilde{V}_c^{\rm LO}$ in eq. 5.23 is the Coulomb potential given only at LO since the axial-vector contribution to the total cross-section is already suppressed by a v^2 term in the non-relativistic expansion [37].

To obtain the relations for the total cross-section (as given in eqs. 5.6 and 5.7), the optical theorem can be used, which relates the forward scattering amplitude to the total cross-section of the scatterer, relating the imaginary part of the current correlators $\mathcal{A}^v$ and $\mathcal{A}^a$ to the phase space integrals over the S and P vertex functions, as given by

$$\mathrm{Im}\Big[\,\mathcal{A}^v(q^2)\,\Big] \;=\; 6\,N_c\int\frac{d^3\boldsymbol{k}}{(2\pi)^3}\,|S(\boldsymbol{k})|^2\,\Gamma_t\left(1-\frac{\boldsymbol{k}^2}{2\,M_t^2}\right), \tag{5.25}$$

$$\mathrm{Im}\Big[\,\mathcal{A}^a(q^2)\,\Big] \;=\; 4\,N_c\int\frac{d^3\boldsymbol{k}}{(2\pi)^3}\,\frac{\boldsymbol{k}^2}{M_t^2}\,|P(\boldsymbol{k})|^2\,\Gamma_t\,. \tag{5.26}$$

Through the use of these equations and the optical theorem, the NNLO predictions of the cross-section for $t\bar{t}$ production at threshold can be obtained.

5.2.3 Total Cross-Section and Momentum Distributions

The optical theorem expressions relating the vector and axial-vector current correlators to the Green vertex functions describing the dynamics of the NRQCD system are given by [37] :

$$\mathrm{Im}\left[\,\mathcal{A}^v+i\frac{3\,N_c\,M_t\,\Gamma_t}{2\,\pi^2}\left[\,2\frac{M_t}{\Lambda}-(1+\sqrt{3})\,\right]\,\right] = 3\,N_c\int\frac{d^4k}{(2\pi)^4}\,|S(k^0,\boldsymbol{k})|^2\,\Gamma_t^2\left(1-\frac{\boldsymbol{k}^2}{M_t^2}\right) \tag{5.27}$$

$$\mathrm{Im}\Big[\,\mathcal{A}^a + i\frac{N_c\,M_t\,\Gamma_t}{\pi^2}\Big[\,-2\frac{\Lambda}{M_t}+2\,(\sqrt{3}-1)\,\Big]\,\Big] = 2\,N_c\int\frac{d^4k}{(2\pi)^4}\,\frac{\boldsymbol{k}^2}{M_t^2}\,|P(k^0,\boldsymbol{k})|^2\,\Gamma_t^2 \quad (5.28)$$

where proper account has been taken for the inclusion of counter-terms arising from photon and Z^0 boson wave function renormalization constants contributing to the NRQCD Lagrangian.

Taking into account these arguments, and through the use of the optical theorem formulation given above, the expressions for the vector and axial-vector current induced cross-section, including all the effects of the finite top quark width at Born level in the non-relativistic expansion, are given by :

$$R^v_{\rm NNLO}(q^2) = \frac{4\,\pi}{q^2}\,C^v\,\mathrm{Im}\Big[\,\mathcal{A}^v(q^2)\,\Big] + \frac{3\,N_c\,\Gamma_t}{2\,\pi\,M_t}\Big[\,2\frac{M_t}{\Lambda}-(1+\sqrt{3})\,\Big]\Big] \quad (5.29)$$

$$R^a_{\rm NNLO}(q^2) = \frac{4\,\pi}{q^2}\,C^a\,\mathrm{Im}\Big[\,\mathcal{A}^a(q^2)\,\Big] + \frac{N_c\,\Gamma_t}{\pi\,M_t}\Big[\,-2\frac{\Lambda}{M_t}+2\,(\sqrt{3}-1)\,\Big]\Big] \quad (5.30)$$

where C^v and C^a are the vector and axial-vector NRQCD short distance coefficients respectively. These provide the matching from the NRQCD effective theory to the full theory by incorporating contributions where the three momenta in the loop integrals are larger than the cutoff $\Lambda \sim M_t$, and hence are excluded in the NRQCD approximation from the momentum scale factorization arguments given in the previous section. The description of the calculation for the short distance coefficients is beyond the scope of this chapter, but for the interested reader their explicit calculation can be found in Appendix A of [37].

By substituting the expressions of eqs. 5.29 and 5.30 into eq. 5.12, the expression for the total cross-section of the full QCD NNLO non-relativistic expansion can be obtained.

In addition, from the expressions of eqs. 5.27 and 5.28, the centre-of-mass three-momentum distributions for the top quarks can be derived as

$$\frac{dR^v_{\rm NNLO}(q^2)}{d|\boldsymbol{k}|} = C^v\,\frac{6\,N_c}{\pi\,q^2}\,\Gamma_t^2\,\Big(1-\frac{\boldsymbol{k}^2}{M_t^2}\Big)\,\boldsymbol{k}^2\int\frac{dk^0}{2\pi}\,|S(k^0,\boldsymbol{k})|^2 \quad (5.31)$$

$$\frac{dR^a_{\rm NNLO}(q^2)}{d|\boldsymbol{k}|} = C^a\,\frac{4\,N_c}{\pi\,q^2}\,\Gamma_t^2\,\frac{\boldsymbol{k}^4}{M_t^2}\int\frac{dk^0}{2\pi}\,|P(k^0,\boldsymbol{k})|^2 \quad (5.32)$$

for the vector and axial-vector current contributions respectively.

Finally, one of the unique characteristics of the top quark production threshold is the existence of an observable forward-backward asymmetry of the top quarks, which is due to the interference of the vector and axial-vector production vertices in the

threshold region.

The vector vertex contributes S- and D-wave resonance states while the axial-vector contribution appears as a P-wave resonance. For values of $M_t \geq 100$ GeV, the widths of the S- and P-wave resonances interfere with each other producing a sizeable forward-backward asymmetry, even in the region below threshold. Since the P-wave contribution to the threshold region is suppressed by a power of β, this leads to a correction to the main S-wave contribution to the total cross-section of $\mathcal{O}(\beta)$, and as the interference terms of the vector and axial-vector couplings are proportional to $\cos\theta$, the amount of forward-backward asymmetry is of $\mathcal{O}(\beta)$.

A general form of the $\cos\theta$ dependence of the differential cross-section contributions leading to the forward-backward asymmetry A_{FB} can be seen in the expression

$$\mathcal{A}_{\text{FB}} = \frac{1}{\sigma_{tot}} \int d|\boldsymbol{k}| \left(\int_0^1 d\cos\theta - \int_{-1}^0 d\cos\theta \right) \frac{d\sigma}{d|\boldsymbol{k}| d\cos\theta} \tag{5.33}$$

The energy dependence of the forward-backward asymmetry in the threshold region, which arises from the different energy spectra of the S- and P-wave resonances, can lead to an important observable for the top quark threshold measurements.

5.2.4 Mass Definition

The measurement of the top quark mass using a threshold scan highly depends on the rise and peak position of the total cross-section lineshape in relation to the mass definition of the top quark. For this reason, the peak position in the total cross-section lineshape must correspond as closely as possible to the $t\bar{t}$ threshold mass $2M_t$, and must be stable with respect to the order of the approximation used as well as parameters such as the strong coupling constant and the renormalization scale.

The top quark pole mass, defined as the pole in the perturbative quark propagator, although infrared safe to all orders of perturbation theory, can lead to significant instabilities in its definition as it is ambiguously defined above Λ_{QCD}, which can lead to large theoretical uncertainties when extracted from data [85, 86]. For these reasons, the so-called threshold masses, such as the $1S$ mass M_t^{1S} [37], need to be employed [36]. The $1S$ mass, defined as half the perturbative mass of the fictitious toponium $1\ ^3S_1$ ground state resonance [37], is physically better defined than the pole mass and leads to a substantially more stable prediction of the energy where the threshold cross-section rises.

While the $1S$ mass is a suitable mass definition for problems involving non-relativistic and close to mass-shell top quarks, problems involving off-shell top quarks

(such as in electroweak corrections) and effects of top quarks at energies much larger than the top mass are more conveniently parameterized in terms of the renormalization scale-dependent top quark $\overline{MS}$ mass $\overline{m}_t(\mu)$.

The top $\overline{MS}$ mass can can be reliably determined from the $1S$ mass using perturbation theory. The perturbative conversion formula is fully known at order α_s^3 [36, 87, 88, 89] and at this time contains a perturbative uncertainty of about 70 MeV for $\overline{m}_t(\mu = \overline{m}_t)$. The conversion formula has, in addition, a significant and irreducible dependence on the value of $\alpha_s(M_Z)$ from the relatively large order α_s terms. An uncertainty $\delta\alpha_s(M_Z) = x \cdot 0.001$ leads to an additional uncertainty for $\overline{m}_t(\overline{m}_t)$ of $x \cdot 70$ MeV [37, 36]. To summarize, the expected uncertainty of the $\overline{MS}$ mass $\overline{m}_t(\mu = \overline{m}_t)$ from a measurement of the $1S$ mass with an error of δM_t^{1S} and for a given error $\delta\alpha_s(M_Z) = x \cdot 0.001$ is

$$\delta\overline{m}_t(\overline{m}_t) \;=\; \delta M_t^{1S} \;\pm\; 70 \text{ MeV(pert)} \;\pm\; x \cdot 70 \text{ MeV}(\alpha_s)\,. \tag{5.34}$$

In this thesis, unless otherwise stated, the top quark mass M_t refers to the threshold 1S mass M_t^{1S}.

5.2.5 Numerical Implementation: `TOPPIK`

The numerical implementation of the threshold calculations described in the previous section is done with the Fortran code `TOPPIK` written by the authors of [37]. The main difficulty in the numerical calculation of the total and differential cross-sections is the solution of the integral equations in the vertex functions of eqs. 5.25 and 5.26. In `TOPPIK` this is done numerically by discretisation. By rewriting the integrals $\int dp'(p' \equiv |\mathbf{p}'|)$ of eqs. 5.25 and 5.26 into sums over a fixed set of momentum values $\Sigma_i p'^i$ (from now called the momentum grid), the integral equations are reduced into a system of linear equations, which can be solved numerically by the inversion of the resulting (complex) matrixes.

For the discretisation of the momentum grid, it turns out that the most efficient method is by using Gaussian quadrature [37], where high numerical accuracy (of order 0.1–1%) can be achieved by using a relatively small number of discretisation points (of order 100).

The main input parameters in the `TOPPIK` calculation are the centre-of-mass energy of the interaction $\sqrt{s}$, the top quark mass M_t (in the 1S mass scheme), the top quark width Γ_t, the strong coupling constant $\alpha_s(M_Z)$ at the Z^0 mass scale (which is then evolved to the scale of the interaction), the Higgs boson mass M_H, and the soft

renormalization scale μ governing the strength of the potential. The renormalization scale affects the stability of the calculation, with the value recommended by [37] being 20 GeV. A table of the default parameters used throughout this thesis (unless otherwise stated) is given in table 5.1.

Table 5.1: Default TOPPIK input parameters used throughout this thesis (unless otherwise stated).

Parameter	Value
$\sqrt{s}$	variable
M_t	175.0 GeV
Γ_t	1.43 GeV
$\alpha_s(M_Z)$	0.118
M_h	115.0 GeV
μ	20.0 GeV

The output of the TOPPIK calculation is the total S- and $S-P$ wave (interference term) cross-section, together with the differential cross-section for S-wave, P-wave and the $S-P$ interference term.

The main practical difficulty in the usage of the TOPPIK code is the CPU time needed for the calculation. For each calculation (i.e. per event) of the total cross-section as a function of the parameters given in $\sigma_{t\bar{t}}(\sqrt{s}; M_t, \Gamma_t, \alpha_s, M_h)$, the TOPPIK calculation takes approximately 1.5 sec of CPU time[3], making the direct use of TOPPIK impractical for the large scale simulations needed at top threshold.

In the remaining part of this chapter, the observables of the top quark production threshold are discussed, including the need for fast calculation of the observable distributions for realistic simulations of the top threshold, and how this is solved in the context of TOPPIK. The next chapter discusses the implementation of the TOPPIK calculations, including realistic experimental effects due to the luminosity spectrum, in a fast fully differential Monte Carlo event generator.

5.3 Observables at the $t\bar{t}$ Threshold

Observables at the top threshold, such as the total cross-section for $t\bar{t}$ production, the momentum distribution of the top quarks and their forward-backward asymmetry, have a high dependence on the mass of the top quark, its width and the strong coupling constant. Also, these observables have an energy dependence in the threshold

[3]On an Intel Pentium 4 workstation with a 3 GHz Dual CPU processor.

region, and hence through a threshold scan, where these observables are measured in a series of points across the top production threshold, precise measurements of the top quark properties can be made.

The most important of these observables is the total cross-section. The position of the rise and the peak in the total cross-section lineshape in the threshold region is highly correlated to the top quark mass as it can be seen in the plot of figure 5.1. Therefore, by measuring the rate of colour singlet top quarks across the threshold

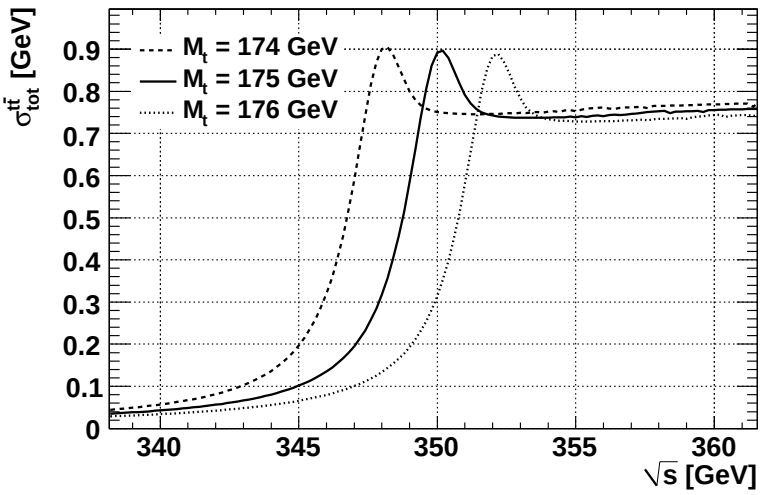

Figure 5.1: Total cross-section for $t\bar{t}$ production at threshold for different values of the top quark mass.

region and thus reconstructing the cross-section lineshape, one can extract the top quark mass from the rise and position of the peak in the cross-section lineshape.

It is important to note that this method benefits from the fact that only the correct identification of top quarks is needed, and not their full reconstruction, making this method independent of detector systematic uncertainties arising from the full reconstruction of top events.

The plots of figure 5.2 show the dependence of the $t\bar{t}$ total cross-section to the width of the top quark (left) and the strong coupling constant α_s (right). This dependence allows the threshold scan to be used for the measurement of the top quark properties, by fitting for the cross-section lineshape with free parameters: the top quark mass, width and the strong coupling constant.

The other two important distributions at the top threshold, which can act as observables for the direct measurement of the top quark properties are the top momentum distribution and the forward-backward asymmetry.

The momentum distribution of the top quarks also has a strong dependence on the value of the top quark mass and the strong coupling constant, but does not depend

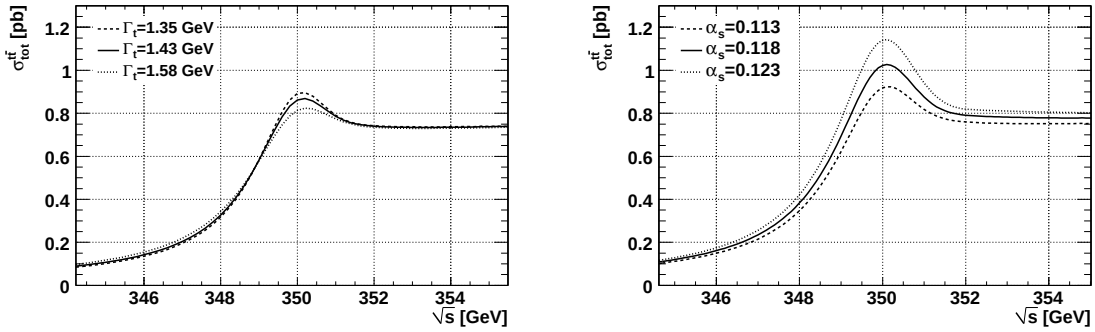

Figure 5.2: Total cross-section for $t\bar{t}$ production at threshold for different values of the top quark width (left) and strong coupling constant (right).

on the value of the top quark width, thus providing an independent observable for the threshold scan with different correlations between the parameters compared to the total cross-section. Figure 5.3 shows the top momentum distribution for different values of the top quark mass and the strong coupling constant.

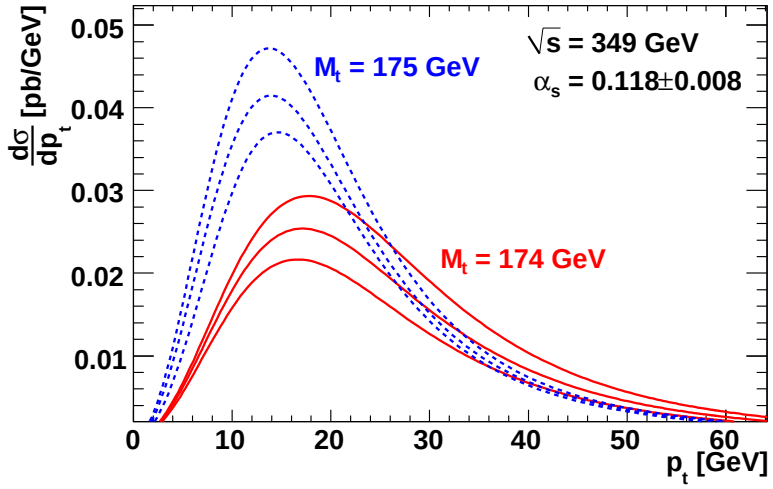

Figure 5.3: Top quark momentum distribution at $\sqrt{s} = 349$ GeV for different values of M_t (solid line versus dashed line) and α_s (three dashed/solid lines correspond to three different α_s values).

Instead of using the momentum distribution directly, an observable more convenient for a threshold scan is the peak position of the momentum distribution, named $\mathrm{P_{peak}}$, which provides an energy dependence across the threshold region similar to that of the total cross-section [28]. The plots on the left of figure 5.4 show the energy dependence of $\mathrm{P_{peak}}$ for different values of the top quark mass, width and strong coupling constant. It can be seen in these plots that although the dependence on M_t is similar to that of $\sigma^{t\bar{t}}_{tot}$, there is little dependence on the top quark width Γ_t and α_s. It can be noted that the minimum value and behaviour of the peak of the top

quark momentum distribution is correlated with the threshold value of the top quark mass, with off threshold top quarks having larger values for the top momentum. The increased values in the momentum distribution for top quarks below threshold are suppressed by the small value of the total cross-section at that energy range. This relationship was also observed in [37] and [28]. Thus the momentum distribution can be used as an observable for the threshold scan with different correlations in the parameters compared to the total cross-section.

Finally, the last interesting observable across the threshold region is the forward-backward asymmetry, A_{FB}, of the $t\bar{t}$ pair. As discussed in section 5.2.3, due to the mixing of S- and P-wave states in $t\bar{t}$ production near threshold, an energy dependent forward-backward asymmetry arises. This provides another independent observable for the measurement of the top quark parameters in a threshold scan. A_{FB} is defined theoretically by eq. 5.33 (experimentally it is defined in the next chapter), and its dependence on M_t, Γ_t and α_s can be seen in the plots on the right of figure 5.4.

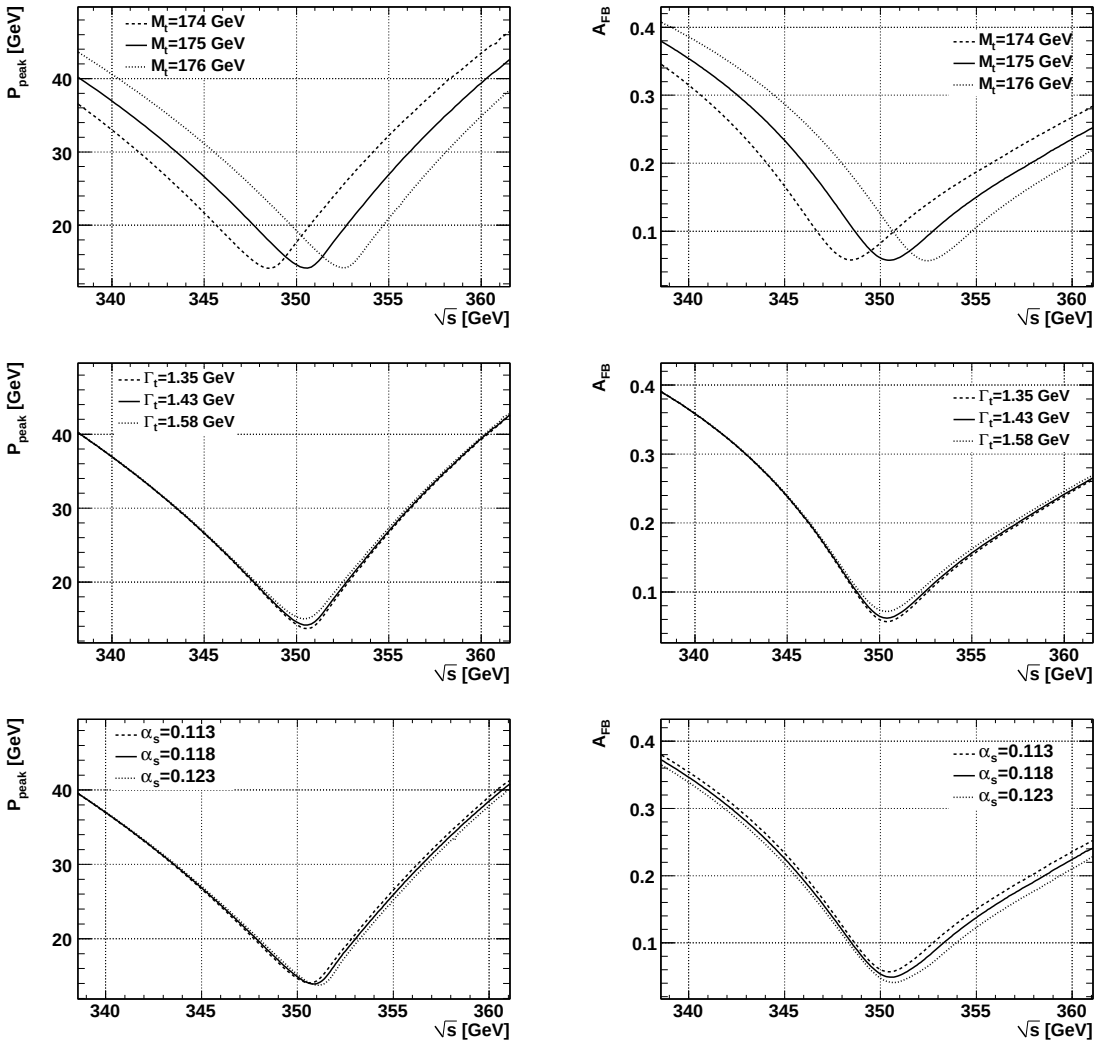

Figure 5.4: P_{peak}(left) and A_{FB}(right) dependence on the top quark mass, the top quark width and the strong coupling constant (from top to bottom).

5.4 Luminosity Spectrum Effects

The dominant experimental uncertainty in the top quark measurements via a threshold scan at a future linear collider is likely to come from the effects of the luminosity spectrum on the threshold observables.

The effects of the luminosity spectrum influence the centre-of-mass energy of collisions, thereby reducing (or increasing) the nominal $\sqrt{s}$ of the machine. In the resonant-like structure such as the total cross-section lineshape, this can highly influence the 'observed' cross-section making it considerably different from the theoretical 'bare' lineshape. This is one of the most important reasons why the luminosity spectrum must be measured precisely as discussed in chapter 4.

To estimate the effects of the uncertainties of the luminosity spectrum on the top quark threshold measurements, elaborate simulation methods must be employed.

The top quark cross-section lineshape in a threshold scan will be measured by measuring the rate of colour singlet top quarks produced at a given integrated luminosity, therefore obtaining the total cross-section for $t\bar{t}$ production. Doing this at different energies across the top threshold allows us to measure the total cross-section lineshape, from which the top quark mass, width and strong coupling constant can be obtained.

To first order, the effect of the luminosity spectrum on the observed cross-section can be approximated by calculating the integral

$$\sigma_{t\bar{t}}^{obs}(\sqrt{s}) = \int_0^1 dx_1\, dx_2\ \mathcal{L}(x_1, x_2, \sqrt{s}) \times \sigma_{t\bar{t}}^{th}(x_1, x_2, \sqrt{s}) \tag{5.35}$$

where $\sigma_{t\bar{t}}^{obs}$ is the observed cross-section, $\sigma_{t\bar{t}}^{th}$ is the theoretical cross-section unsmeared by the luminosity spectrum, $\mathcal{L}$ is the luminosity spectrum (see chapter 4), and $x_{1,2}$ are the fractional energy losses for the two colliding beams. This effectively smears out the theoretical 'bare' cross-section lineshape approximating the effects of the luminosity spectrum on the observed total cross-section. This is the method used in most previous experimental simulations of the top threshold measurements at a linear collider (e.g. [28, 29, 30, 31]).

This integral can be calculated numerically using a realistic luminosity spectrum (as in figure 4.3) and the luminosity spectrum parameterization and simulation methods described in chapter 4, leading to figure 5.5, where the effects of the different components of the luminosity spectrum on the cross-section lineshape are clearly visible.

This approximation of 'smearing' the theoretical observables by the luminosity

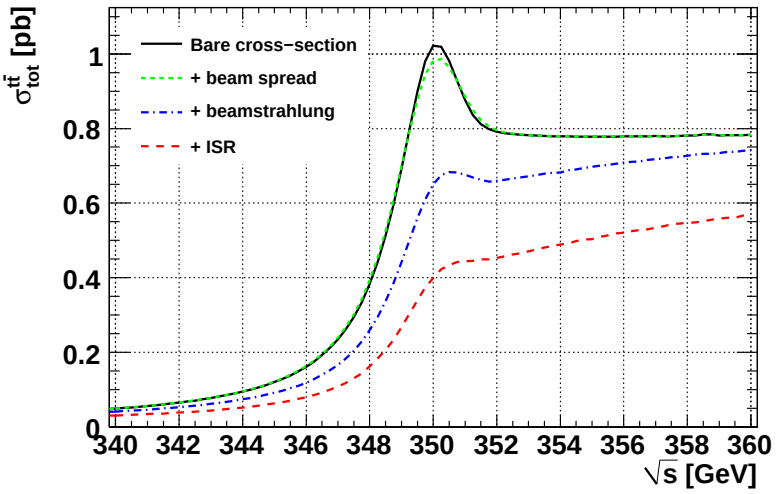

Figure 5.5: Total cross-section smeared by the three components of the luminosity spectrum (as in figure 4.3).

spectrum cannot be applied to the differential observables such as the momentum distribution and forward-backward asymmetry. These distributions need to be measured from fully reconstructed events with the luminosity spectrum applied to the microscopic level since boosts due to asymmetries in the beam energies of the colliding beams, or correlations between the beam energies could potentially distort the observed distributions and therefore an event-by-event simulation is needed. Even for the total cross-section, the 'smearing' simulation neglects experimental effects from event identification uncertainties, as well as detector acceptance effects and other reconstruction and detector related systematics.

The next chapter describes how this problem is solved by implementing the theoretical calculations summarized in the previous sections into a fully differential event generator including the effects of the luminosity spectrum at the microscopic level, which enables us to perform realistic simulations of the top quark production threshold measurements.

5.5 Summary

In this chapter, a theoretical description of the $t\bar{t}$ threshold was given, following the work of [37], by explaining the NRQCD framework that is used in the calculations of the top quark threshold observables. An overview of how one arrives from the NRQCD Lagrangian to the S- and P-wave Green functions, and from there to expressions for the total and differential cross-sections was described, with a special focus on the role of the Green functions as the variables that contain all the dynamics of the QCD system, and which are used in the next chapter as the basis of the calculation for the simulation of the top quark threshold using a Monte Carlo event generator.

The numerical implementation of the threshold calculation, in the form of the code `TOPPIK`, was described, focusing on the fact that `TOPPIK` is unsuitable for large scale computations due to its high CPU requirements.

The behaviour of the main observable distributions at the top threshold was examined, by looking at how the top quark total cross-section $\sigma_{tot}^{t\bar{t}}$, the peak in the momentum distribution P_{peak}, and the forward-backward assymetry A_{FB} change with respect to changes in the values of the top quark mass M_t, the top quark width Γ_t, and the strong coupling constant α_s.

Finally, a first discussion of how the luminosity spectrum affects the top threshold was given, outlining the reasons why a fully differential event generator is needed for future simulations of the top quark threshold.

Chapter 6

Monte Carlo Event Generator for $t\bar{t}$ Production at Threshold

"[...] Another change which I find disturbing is the rising tyranny of Carlo. No, I don't mean that fellow who runs CERN, but the other one, with first name Monte. The simultaneous increase in detector complexity and in computational power has made simulation techniques an essential feature of contemporary experimentation. The Monte Carlo simulation has become the major means of visualization of not only detector performance but also of physics phenomena. So far so good. But it often happens that the physics simulations provided by the Monte Carlo generators carry the authority of the data itself. They look like data and feel like data, and if one is not careful they are accepted as if they were data. All Monte Carlo codes come with a GIGO (garbage in, garbage out) warning label. But the GIGO warning label is just as easy for a physicist to ignore as that little message on a pack of cigarettes is for a chain smoker. [...]"

J.D. Bjorken

Extract from a talk given at the 75th anniversary celebration of the Max Planck Institute of Physics, Munich, Germany (Dec. 10th 1992). As quoted in: Beam Line, Winter 1992, vol 22., No. 4

6.1 Introduction

Most studies in particle physics, and especially if they are based on accelerators that have yet to be built, rely in some way on the Monte Carlo (MC) method.

In this chapter we will outline some of the basics of Monte Carlo techniques, review some of the existing MC generators for top quark production at threshold and highlight their shortcomings, and discuss how these shortcomings can be overcome in the form of a new $t\bar{t}$ threshold event generator, `ttbarMC`.

6.2 The Monte Carlo Method

The Monte Carlo method is one of the most important tools in modern particle (and in general computational) physics. Its uses range from integrating cross-sections for a process, to generating fully differential events, to detector simulations for correcting the data for acceptance and detection inefficiencies, data simulation, analysis and more. It is equally important both in the preparation stage of experiments, when data are not available and have to be simulated in order to study the design and performance of the experimental apparatus, and during the running of experiments, for comparing simulation against data in order to better understand the experimental apparatus and the actual data.

In this section we will outline some of the key features of the Monte Carlo method, leaving more detailed descriptions to be found in references [90] and chapter 3 of [91].

The Monte Carlo method is essentially a numerical method for calculating integrals. In its simplest form it can be described as treating an integral as the average of its integrand. Suppose we want to calculate the definite integral of a function $f(x)$, this can be written as

$$I = \int_{x_1}^{x_2} f(x)dx = (x_2 - x_1)\langle f(x)\rangle \approx (x_2 - x_1)\frac{1}{N}\sum_{i=1}^{N} f(x_i) \tag{6.1}$$

which means that by taking N values of x, uniformly distributed in the interval (x_1, x_2), the average value of $f(x)$ will form a reasonable estimate of I.

To perform this calculation we need a number of x values uniformly distributed. For this we can use a sequence of uniformly distributed random numbers[1]. The use of random numbers leads to one of the key features of the MC method, that for a large enough N, the accuracy of this method follows the Central Limit Theorem. This means that the distribution of $\langle f_i\rangle$ will tend to a Gaussian with a standard deviation $\sigma_{MC} = \sigma/\sqrt{N}$, with σ the standard deviation of f_i, and since σ will approximate the standard deviation of $f(x)$, our accuracy scales with $1/\sqrt{N}$.

The rate of convergence of the MC method does not look very convincing at first, especially when compared with the more traditional methods of the Trapezium rule, Simpson's rule or Gaussian quadrature. These methods use a similar principle as in eq. 6.1, but with splitting the integration domain in a uniform weighted grid (non-uniform in the case of Gaussian quadrature) and performing sequential averaging

[1] What defines a 'random' number is the subject of a large literature (e.g. [92]). For our purposes we assume that by 'random' number we mean a pseudo-random number with a large enough period like the $2^{19937} - 1$ period of the Mersenne-Twistor algorithm [93].

over the grid of the integration domain. In one-dimensional integrals these methods converge with a rate of $\frac{1}{N^2}$ for the Trapezium rule, $\frac{1}{N^4}$ for Simpson's rule and $\frac{1}{N^{(2m-1)}}$ for Gaussian quadrature, with m being the order of quadrature.

The major advantage of the MC method over the more traditional quadrature methods comes when looking at multi-dimensional integrals. The quadrature methods suffer from the fundamental problem that the convergence rate scales according to the number of points in each integration axis, $N^{1/d}$, with d the dimension of the integral. Hence, in multi-dimensional integrals, the Trapezium rule converges like $\frac{1}{N^{2/d}}$, Simpson's rule like $\frac{1}{N^{4/d}}$, and Gaussian quadrature like $\frac{1}{N^{(2m-1)/d}}$. The MC method however, still obeys the Central Limit Theorem thus still converging with $\frac{1}{\sqrt{N}}$ rate, and since in any realistic applications including particle physics the integrals tend to be multi-dimensional, the MC method is the method of choice.

In particle physics the most typical case of using the MC method is in event generation. Event generators are used to encode our theoretical understanding of a physics process, and simulate it as it would appear in a detector, in the form of particle physics events.

In event generation for collider physics, what is observed in an experiment is described by the convolution of the beam distributions with the collision cross-section. In e^+e^- collisions for example, the collision centre-of-mass energy can be described by the distribution of energies in the two beams (as discussed in Chapter 4), the luminosity spectrum. The observed cross-section at the collider will then be the convolution of the luminosity spectrum with the differential cross-section for the physics process in question.

The luminosity spectrum as a function of the integration variables for the two beams x^{n_1} and x^{n_2} can be described as

$$\frac{d^{n_{1,2}}\mathcal{L}}{dx_1^{n_1}dx_2^{n_2}} \tag{6.2}$$

and the differential cross-section for the final state partons, encoding all the final state scattering angles and kinematic variables in y^m, is

$$\frac{d^m\sigma_{th}}{dy^m} \tag{6.3}$$

where σ_{th} is the theoretical cross-section of the process.

The observed cross-section σ_{obs}, is the convolution of previous two distributions,

and can be described by the phase space integral

$$\sigma_{obs} = \int d^{n_1}x_1 \int d^{n_2}x_2 \int d^{m}y \, \frac{d^{n_{1,2}}\mathcal{L}}{dx_1^{n_1} dx_2^{n_2}} \cdot \frac{d^m \sigma_{th}}{dy^m} \tag{6.4}$$

It is this integral that event generators compute, by treating the integrand as a probability distribution and selecting events in phase space according to the corresponding probabilities of the integration variables.

6.3 Existing Generators

To perform a study of the $t\bar{t}$ threshold measurements at a linear collider, accurate predictions of the total cross-section, momentum and angular distributions are needed.

Most general purpose event generators calculate the matrix elements for the top quark threshold only to leading order in QCD As it is discussed in chapter 5, the dynamics of the $t\bar{t}$ system at threshold are much more complicated than this approach. This is illustrated with the plot of figure 6.1 which shows the total cross-section predictions for $t\bar{t}$ production at threshold from the general purpose event generators `Pythia` [94], `Herwig` [95] and `Pandora` [66]. Also plotted (red line) is the NNLO QCD prediction calculated using the `TOPPIK` code [37]. `Herwig` and `Pythia` use LO matrix elements for the total cross-section calculation, while `Pandora` uses helicity amplitudes to build up the total cross-section prediction. `TOPPIK` calculates the full QCD corrections at NNLO using the formalism discussed in chapter 5.

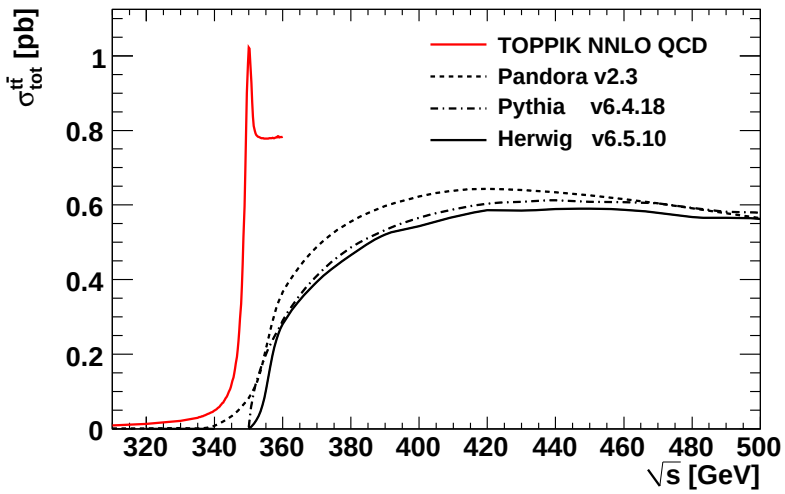

Figure 6.1: Total cross-section predictions from standard multi-purpose LO calculations from `Pythia`, `Herwig` and `Pandora` and NNLO QCD prediction from `TOPPIK`.

It is obvious from this plot that the calculations used in the general purpose event generators do not suffice for an accurate description of the $t\bar{t}$ production threshold. Hence a new event generator must be developed.

In the following, we will describe the implementation of NNLO QCD calculations [37] for the $t\bar{t}$ production threshold into an efficient Monte Carlo event generator, to be used in conjunction with the luminosity spectrum effects, for studies of the $t\bar{t}$ threshold measurements.

6.4 A New $t\bar{t}$ Threshold Generator : `ttbarMC`

For a proper description of the $t\bar{t}$ production threshold, a new specialized event generator using high order QCD calculations is needed.

For the implementation of such a generator we define a set of requirements regarding its design and usability. The first being that the QCD calculations used must be state-of-the-art such that an accurate description of the threshold dynamics can be obtained. The luminosity spectrum must be generically built into the MC integration procedure and its effects carefully taken into account.

It must also have reasonably fast execution time so that realistic studies can be performed and it must have the ability to return fully hadronized events.

In the following we will describe the implementation of such a generator including the fulfillment of the requirements listed above.

6.4.1 Generator Layout : Using `TOPPIK`

The QCD calculations of the total and differential quantities are performed using the `TOPPIK` code, which is the implementation of the calculations described in [37] and summarized in chapter 5.

`TOPPIK` is a fortran code that performs a fully differential NNLO QCD calculation for $t\bar{t}$ production at threshold, by using the Green function method to numerically solve the Lippmann-Schwinger equation[2]. The main problem with directly using it in an event generator is CPU time. It takes about 1.5 sec [3] for every function call that calculates the total cross-section including differential quantities. Most of the CPU time in `TOPPIK` is spent on the inversion of complex matrices for solving sets of linear equations. The solution of the Lippmann-Schwinger equation using the Green function method numerically is done by forming and solving sets of up to 300

[2]The Fourier transform of the Schrödinger equation.

[3]On an 3 GHz Intel Pentium 4 PC

linear equations containing the discretised Green functions. These are cumbersome computations with no potential for a large speed-up by using traditional means (i.e. faster computers, code optimizations, etc.).

This is further complicated by the need to explicitly take into account the luminosity spectrum in event generation, meaning that every event can have a different $\sqrt{s}$. The fact that the QCD dynamics at threshold change rapidly with $\sqrt{s}$, so that production angles and momentum distributions change, means that we cannot produce events at a fixed $\sqrt{s}$ and then scale/boost them by the luminosity spectrum as was done in the case of Bhabha scattering described in chapter 4. The luminosity spectrum has to be explicitly taken into account in the MC integration procedure.

A typical event generator makes 10^6–10^7 function calls for MC exploration / integration and generation of events. If we consider generation of events only, an example run for 10^6 events would require about 11 days of CPU time just for the `TOPPIK` function calls. Therefore a generator which can significantly reduce this processing time is highly desirable.

The solution for speeding-up the calculations (described in section 6.4.2) such that they can be used in a practical event generator is to use interpolation techniques on a pre-calculated grid of `TOPPIK` output (look-up table). Use of interpolation provides a speed-up of about 10^3 relative to the direct use of `TOPPIK`, allowing us to use these calculations in event generation in an efficient way.

A schematic diagram of the layout of `ttbarMC` can be seen in figure 6.2. The core of the generation procedure is the interpolated version of the `TOPPIK` calculations employing NNLO QCD quantities for the differential distributions of the generated $t\bar{t}$ pairs.

The algorithms for MC integration and event generation are based on the use of the general purpose cellular MC event generator `mFOAM` [96]. The kinematics of the events are computed at this stage and event rejection according to conservation laws and phase space restrictions takes place. The luminosity spectrum is applied at the event-by-event level. The $t\bar{t}$ pair is then decayed into $W^+W^-b\bar{b}$ with the appropriate kinematics for two-body decays.

The parton level $W^+W^-b\bar{b}$ events can then either be returned to the user or be passed on to `Pythia` for hadronization. `ttbarMC` interacts with `Pythia` via the `pandora_pythia` interface. The `pandora_pythia` interface was originally developed as a plug-in to the `Pandora` MC generator and was modified accordingly to suit our needs.

In the following sections we will examine in detail all the steps involved in the generation of events using `ttbarMC`.

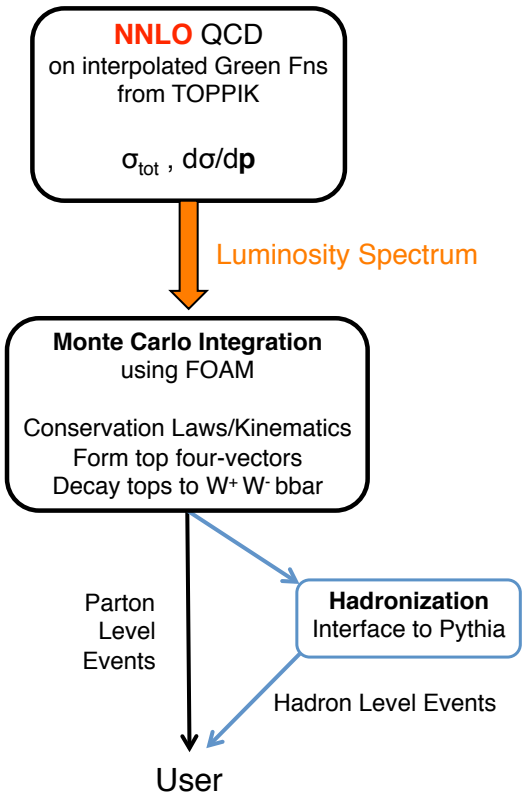

Figure 6.2: Schematic layout of `ttbarMC`.

6.4.2 Interpolation

In order to use the NNLO QCD calculations as implemented in the code `TOPPIK` in a MC event generator, a large speed-up of the CPU time of the calculations is needed. To achieve this, we use interpolation techniques on a look-up table formed by `TOPPIK` calculated quantities.

The principle behind the interpolation scheme is to run the full `TOPPIK` calculation once and store the fundamental variables of the calculation in a look-up table as a function of the dynamic variable that we are interested in. When fast access to the `TOPPIK` calculations is needed (e.g. in event generation) this can be done by performing interpolations on the stored variables, and building the rest of the calculation from the interpolated quantities.

The QCD calculations summarized in chapter 5 and implemented in `TOPPIK` use the Green function technique for solving the Lippmann-Schwinger (LS) equation. As solutions to the LS equation, the Green functions encode all the dynamics of the $t\bar{t}$ system. Furthermore, the most CPU time-consuming part of the calculation is the numerical solution of the LS equation, and since the Green functions come after the solution they are ideal for use in the interpolation scheme. The rest of the calculation

from the S- and P-wave Green functions of eqs. 5.22 and 5.23 to the total and differential cross-sections of eqs. 5.29, to 5.33 can be performed in a computationally simple and fast manner.

The calculations of `TOPPIK` mainly depend on the input values of the mass of the top quark M_t, the width of the top quark Γ_t, the strong coupling constant α_s, the Higgs mass M_H and the centre-of-mass energy of the interaction $\sqrt{s}$. The only quantity that can change on the event-by-event basis is the $\sqrt{s}$ of the interaction, and hence that is the dynamic variable of the interpolation.

To build up the interpolation grid (look-up table) we need to calculate with `TOPPIK` the Green functions for a range of $\sqrt{s}$ values and save them in a file. Every time `ttbarMC` is called to generate events, it will load this file into memory and perform interpolations between the pre-computed values of the Green functions at the interpolation grid points and any required value of $\sqrt{s}$ between the grid points (but contained within the range of the interpolation grid). Using this method, the interpolation technique will mimic the actual call to `TOPPIK` but be much faster computationally.

To realize this technique, we need to examine the form and evolution of the Green functions as a function of the interpolation variable $\sqrt{s}$. The Green functions used in the solution of the LS equation are complex variables, one for the S-wave part of the solution and one for the P-wave part. In their numerical implementation they are a discretised distribution with as many as 300 sampling points. The discretisation is chosen in such a way so that the integration of the Green functions using Gauss-Legendre numerical quadrature can be trivially performed.

The first step in the interpolation procedure is to transform the complex S- and P-wave Green functions from real and imaginary parts to the magnitude and phase of the complex number. This is done because the magnitude/phase domain offers a more simple functional behaviour for the two components with a smoother evolution in $\sqrt{s}$, which is better suited for the interpolation that follows. The plots of figure 6.3 show the evolution of the components of the S-wave Green function for different $\sqrt{s}$ values. After the interpolation is performed, the magnitude and phase representation is transformed back to the cartesian components of the complex number.

For a finely spaced pre-computed interpolation grid, we can use linear interpolations between adjacent grid points to obtain any required value of the Green functions within the range of the grid.

This can be illustrated with the help of the diagram in figure 6.4 where the two black solid points represent two adjacent entries in the interpolation grid, and the red dashed point is the position at which the calculation is to be performed. This can be

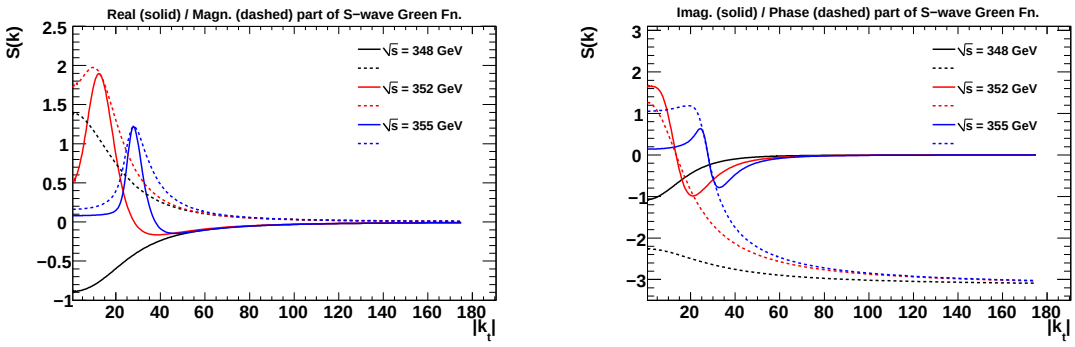

Figure 6.3: The S-wave Green function is shown for different values of $\sqrt{s}$, with $|k_t|$ being the magnitude of the top quark's three momentum vector. The plot on the left shows the real part (solid) and magnitude (dashed) of the Green function while the plot on the right shows the imaginary part (solid) and phase (dashed) component.

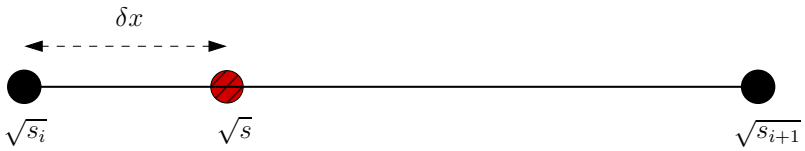

Figure 6.4: Linear interpolation in-between grid points

done by computing

$$y(\sqrt{s}) = y(\sqrt{s_i}) + \delta x(y(\sqrt{s_{i+1}}) - y(\sqrt{s_i})) \tag{6.5}$$

with the fractional difference between grid points given by

$$\delta x = \frac{\sqrt{s} - \sqrt{s_i}}{\sqrt{s_{i+1}} - \sqrt{s_i}} \tag{6.6}$$

$y(\sqrt{s})$ indicates the value of the S- or P-wave Green function at that $\sqrt{s}$. Since in their numerical format, the Green functions are actually discretised (usually in 300 points), the interpolation must be performed for all discretised points.

The interpolation method can be tested by comparing computations between `TOPPIK` calculated values and interpolated values. This is shown in the plots of figure 6.5 where we compute the S-wave Green function for 300 different $\sqrt{s}$, uniformly distributed in $\sqrt{s} = 2M_t \pm 8$ GeV range, and compare with the interpolated values for the same $\sqrt{s}$.

It can be seen from these plots that the interpolation is accurate in reproducing the `TOPPIK` calculated values since both difference distributions peak at 0 with an RMS of $< 0.03\%$, which is comparable to the numerical accuracy of `TOPPIK`. The P-wave Green function yields similar results.

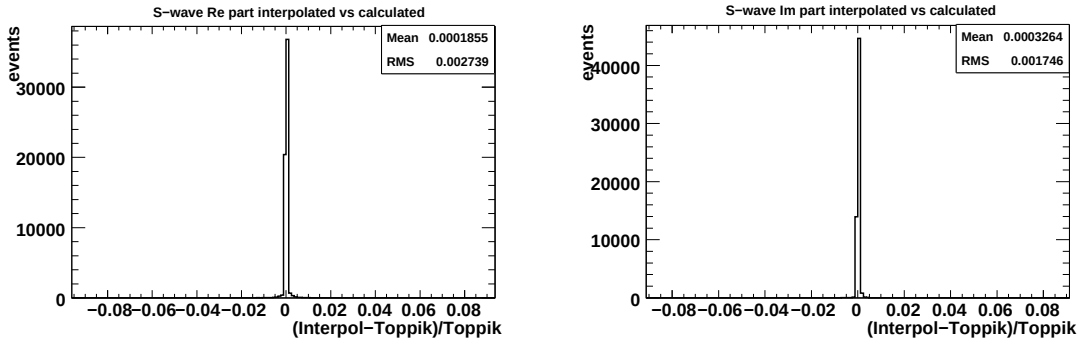

Figure 6.5: Difference plots for the real and imaginary parts of the S-wave Green function for 300 different $\sqrt{s}$ uniformly distributed in the $\sqrt{s} = 2M_t \pm 8$GeV range, as computed with TOPPIK and the interpolator. The RMS of the distributions is ~ 0.005.

The rest of the calculation from the interpolated Green functions to the total and differential cross-section quantities is implemented in ttbarMC, by using the same methods as in TOPPIK but re-written in an object-oriented way.

The ultimate test for the interpolation method and in general the implementation of the TOPPIK calculations in ttbarMC is to compare the predictions for the total cross-section $\sigma_{tot}^{t\bar{t}}$ between TOPPIK and the interpolator based calculation. The total cross-section depends on the integral of the differential cross-section distributions and hence provides the ultimate test for the accuracy of the interpolation, by checking all the components of the calculation at once.

The plots of figure 6.6 show the comparison of the predictions for the total $t\bar{t}$ cross-section between the direct calculation of TOPPIK and the interpolation based calculation in ttbarMC. The two predictions agree to within less than 0.5% of each other, which is comparable to the numerical precision of TOPPIK and is much less than the theoretical uncertainty of the QCD calculation. Thus the interpolation based calculation can be used instead of the direct TOPPIK calculation without any compromise in the accuracy of the results.

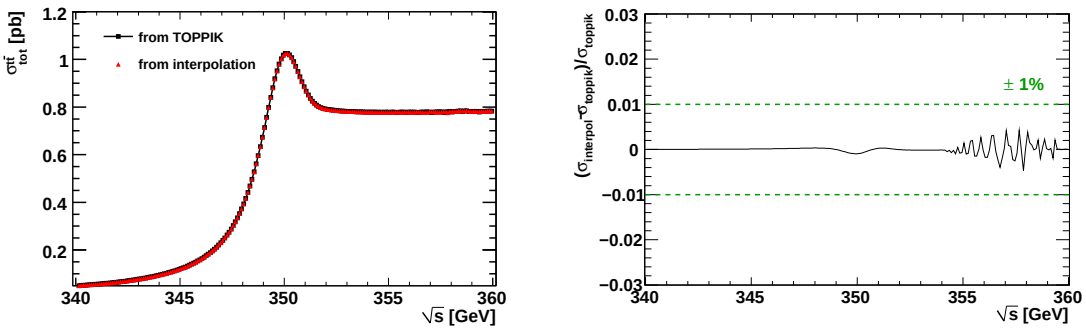

Figure 6.6: Total cross-section predictions from TOPPIK and interpolation based calculations (left) and the fractional difference of the two calculations (right).

A further demonstration of the agreement between the TOPPIK calculated quantities and the interpolation based ttbarMC calculations will be given in section 6.4.5, where we will compare the differential distributions produced from generated events using ttbarMC to the theoretical predictions of those distributions by TOPPIK, and show that they are in perfect agreement with each other.

Finally, using the interpolation based method for the calculation of the QCD predictions of TOPPIK takes ~ 1 msec of CPU time per calculation, a relative speed-up of 10^3 to using TOPPIK directly. Thus, this allows us to use these state-of-the-art calculations in the context of event generation with a realistic CPU execution time, solving the problem that had forbade using them in experimental studies with event generators until now.

6.4.3 Phase Space Integration

The phase space integral in event generation is the convolution of the initial state beam distributions with the collision cross-section. It defines the amount of observed cross-section for a given process taking into account all phase space variables that contribute to the final state particles. A generic example of this is given in eq. 6.4 where the phase space integral is the convolution of the two colliding beam distributions with the differential cross-section of the process.

In a similar way, in the case of the $t\bar{t}$ production threshold the phase space integral is defined as the convolution of the two beam distributions contributing to the luminosity spectrum, and the differential cross-section for $t\bar{t}$ production. By treating the integrands as probability distributions and selecting events in phase space according to the corresponding probabilities for each variable of integration, the expected value for the observed cross-section is obtained.

The distribution of energy in the two colliding beams is described by the luminosity spectrum. The luminosity spectrum distribution has the form

$$\frac{d\mathcal{L}(x_1^{isr}, x_1^{bs}, x_2^{isr}, x_2^{bs}; \sqrt{s})}{dx_1^n dx_2^n} \tag{6.7}$$

where x^{isr} and x^{bs} are the probabilities of energy loss for the initial state particles from ISR and beamstrahlung respectively. Subscripts 1 and 2 denote the electron and positron beams. The formalism of using the luminosity spectrum in the phase space integral is the same as was discussed in section 4.3.1, with the difference that the ISR calculation is explicitly implemented in ttbarMC rather than using the Pandora implementation. This is done using the same procedure as in Pandora, by treating

eq. 4.14 as the probability distribution for an initial state particle exhibiting ISR radiation, but performing the integration of the probability distribution directly in `ttbarMC`.

The expression for the differential cross-section for $t\bar{t}$ production at threshold is that of eqs. 5.31 and 5.32. It includes the vector current (S-wave) differential cross-section and the vector/axial-vector current (S-P wave) intereference term. In the phase space integral this has the form

$$\frac{d\sigma^{t\bar{t}}(p_{t\bar{t}}, \Omega; \sqrt{s})}{dp_{t\bar{t}}\, d\Omega} \tag{6.8}$$

where $p_{t\bar{t}}$ is the intrinsic momentum of the $t\bar{t}$ pair, and $d\Omega = d\cos\theta d\phi$ is the solid angle element. The integral over solid angle and momentum gives the total cross-section for the process.

The convolution of eqs. 6.7 and 6.8 leads to the phase space integral for $t\bar{t}$ production. It has the form

$$\sigma^{t\bar{t}}_{obs}(\sqrt{s}) = \int d^{n_1}x_1\, d^{n_2}x_2\, dp_{t\bar{t}}\, d\Omega\, \frac{d^{n_{1,2}}\mathcal{L}(x_1^{isr}, x_1^{bs}, x_2^{isr}, x_2^{bs}; \sqrt{s})}{dx_1^{n_1} dx_2^{n_2}} \cdot \frac{d\sigma^{t\bar{t}}(p_{t\bar{t}}, \Omega; \sqrt{s})}{d\Omega} \tag{6.9}$$

This defines the entire phase space for the generation of events. To satisfy phase space restrictions according to the allowed kinematics and taking into account energy-momentum conservation in the generation of events, we impose a set of kinematic checks for each selected phase space point. These are discussed in detail in section 6.4.4. If any of these checks is not satisfied, the corresponding phase space point is forced to contribute zero to the integral (forcing zero weight), such as to exclude it from the estimate of the integral and the generation of events.

The computation of the kinematic variables at this stage of the calculation leads to the formation of the parton level events as described in the next section.

The MC integration and event generation in `ttbarMC` is based on the `mFoam` [96] MC event generator/simulator. `mFoam` is a general purpose self-adapting MC event generator that uses a cellular splitting algorithm for integration and simulation of any arbitrary unnormalized probability density function (PDF). The calculation has two stages. `mFoam` first performs the 'exploration' stage in which it splits the integration domain into a grid of cells (refered to as 'foam') according to a recursive binary splitting algorithm, and approximates the integration PDF $\rho(\vec{x})$ by another PDF $\rho'(\vec{x})$ which is constant in each integration cell, with $w = \rho(\vec{x})/\rho'(\vec{x})$ being the MC weight. The main objective of the cell splitting algorithm is to minimize the ratio of the maximum weight to the average weight $w_{max}/\langle w \rangle$.

In the generation stage of the calculation, weighted events are generated according to the approximate PDF $\rho'(\vec{x})$. For events of weight equal to one, the standard acceptance-rejection MC algorithm is used, with a certain rejection rate defining the efficiency of the MC run. A big advantage of `mFoam` is that by optimizing its exploration stage for maximum weight reduction by minimizing $w_{max}/\langle w \rangle$, a low rejection rate can be achieved, leading to more efficient MC generation.

The algorithms of `mFoam` have been succesfully used for event generation in the `KKMC` [97] MC event generator.

Another advantage for using `mFoam` is its implementation within the `ROOT` analysis framework [98]. Because of this `mFoam` shares the `ROOT` input-output (IO) framework, which enables us to be able to store and retrieve from memory a full instance of the MC state. Thus in a lengthy MC run, one can pause the run during execution and save the state of the run to memory. At a later stage, by loading from memory the saved file containing the `mFoam` state, the generation can continue exactly from where it was stopped, with the same random number sequences and no need to re-explore the probability distributions.

6.4.4 Generation Kinematics

In this section we describe in detail the kinematics used to generate partons from the quantities calculated in the phase space integral of eq. 6.9.

We start by defining the centre-of-mass energy of the collision according to the colliding leptons.

The 4-vectors of the incoming leptons are:

$$x_1 \cdot (E_1, 0, 0, P_{1z}) \qquad \text{and} \qquad x_2 \cdot (E_2, 0, 0, -P_{2z}) \tag{6.10}$$

where E_1 and E_2 are the energies of the electron and positron respectively and x_1 and x_2 are the fractional energy losses according to the luminosity spectra given by the MC integrator.

Now adding the two together (neglecting the electron mass) gives the total centre-of-mass energy:

$$\begin{aligned}
& \mid \mathbf{P}_1 + \mathbf{P}_2 \mid = (x_1 E_1 + x_2 E_2, 0, 0, x_1 P_{1z} - x_2 P_{2z}) \\
\Rightarrow \quad & x_1^2 E_1^2 + 2 x_1 x_2 E_1 E_2 + x_2^2 E_2^2 - (x_1 P_{1z} + x_2 P_{2z})^2 = s \\
\Rightarrow \quad & x_1^2 E_1^2 + 2 x_1 x_2 E_1 E_2 + x_2^2 E_2^2 - x_1^2 E_1^2 - 2 x_1 x_2 P_{1z} \cdot P_{2z} - x_2^2 E_2^2 = s \\
\Rightarrow \quad & 2 x_1 x_2 (E_1 E_2 - P_{1z} \cdot P_{2z}) = 2 x_1 x_2 (2 E_1 E_2) = 4 x_1 x_2 E_1 E_2 = s
\end{aligned}$$

$$\sqrt{s} = 2\sqrt{x_1 x_2 E_1 E_2} \tag{6.11}$$

The intrinsic momentum of the top, P_t, is chosen by the MC integrator using the intrinsic momentum integral distribution (incorporating all QCD kinematics (see chapter 5)).

To verify energy conservation we impose that :

$$\frac{E_{cme}}{2} \geq P_t \qquad \text{otherwise } \texttt{reject} \tag{6.12}$$

otherwise we reject the event. The total available energy E_{cme} is split in half because the choice of P_t controls the virtuality of the t or $\overline{t}$.

Since the available energy and momentum of the $t\overline{t}$ system have been defined we define the virtual mass of the top quark using

$$E^2 = M^2 + P^2. \tag{6.13}$$

Given the available energy is $E_{cme}/2$, it follows that

$$\begin{aligned} \left(\frac{E_{cme}}{2}\right)^2 &= M_t^2 + P_t^2 \\ \Rightarrow \qquad M_t &= \sqrt{\frac{E_{cme}^2}{4} - P_t^2} \end{aligned} \tag{6.14}$$

It should be noted that the virtuality of the generated top quarks at this stage depends only on the choosen value of the top quark momentum thereby conserving total energy and momentum. More complicated treatments such as using a Breit-Wigner distribution (as is done for the decay os the W bosons below) can also be employed but given the threshold nature of the top quark mass measurements it is expected that it would not make a difference in the results presented here.

Now we can start building the top quark decays to W-bosons and b-quarks by choosing energy-momentum values for the decay system using standard two-body decay kinematics.

Starting with the decay of the top in a W^+ and a b-quark we can give a Lorentz-like mass distribution to the W by

$$M_{W^+} = \sqrt{M_W^2 + M_W \cdot \Gamma_W \cdot \tan\left(rnd[-1,1] \cdot \frac{\pi}{2}\right)} \qquad \text{for } M_{W^+} > 0 \tag{6.15}$$

where M_{W^+} is the effective mass of the W^+ in the decay and M_W and Γ_W are the

PDG[2] values of the mass and width of the W. The $rnd[-1,1]$ is a random number uniformly distributed between -1 and 1. Eq. 6.15 follows the non-relativistic Breit-Wigner (also known as Cauchy-Lorentz) distribution function[4]

$$P(m)dm = \frac{1}{(m-m_0)^2 + \frac{\Gamma^2}{4}}dm \tag{6.16}$$

by using the inverse of the cumulative distribution function (CDF) of the Cauchy distribution

$$F^{-1}(p; m_0, m_0\Gamma) = m_0 + m_0 \cdot \Gamma \cdot \tan\left(\pi \cdot \left(p - \frac{1}{2}\right)\right) \tag{6.17}$$

Values distributed according to $F^{-1}(= m^2)$ give a Breit-Wigner mass distribution to the W. For the mass of the b-quark, M_b, we use the PDG[2] value.
To check that we still conserve the mass of the top decay system we impose that

$$M_t \geq M_{W^+} + M_b \qquad \text{otherwise } \texttt{reject} \tag{6.18}$$

otherwise we reject the event.

To choose values for the energy of the W^+ and b-quark we start from the energy momentum conservation relation in the rest frame of the top

$$\mathbf{P}_t = \mathbf{P}_W + \mathbf{P}_b \tag{6.19}$$

with

$$\mathbf{P}_t = (M_t;\ 0) \qquad \mathbf{P}_W = (E_W;\ \vec{P_W}) \qquad \mathbf{P}_b = (E_b;\ \vec{P_b}) \tag{6.20}$$

Re-arranging eq. 6.19 to solve for E_W yields

$$\begin{aligned}
(\mathbf{P}_b)^2 &= (\mathbf{P}_t - \mathbf{P}_W)^2 \\
\Rightarrow \mathbf{P}_t^2 + \mathbf{P}_W^2 - 2\mathbf{P}_t \cdot \mathbf{P}_W &= M_b^2 \\
\Rightarrow M_t^2 + M_W^2 - 2M_t E_W &= M_b^2 \qquad \text{since} \qquad \mathbf{P}_t \cdot \mathbf{P}_W = M_t E_W - 0 \cdot \vec{P_W} \\
\Rightarrow E_W &= (M_t^2 + M_W^2 - M_b^2)\ /\ 2M_t
\end{aligned} \tag{6.21}$$

similarly solving eq. 6.19 for E_b yields

$$E_b = (M_t^2 - M_W^2 + M_b^2)\ /\ 2M_t \tag{6.22}$$

[4]The mass distribution of hadrons and bosons involved in the hard process follow the non-relativistic Breit-Wigner distribution [94].

To ensure that the generated W and b-quark are on-shell we check that

$$E_{W^+} \geq M_{W^+} \qquad \text{and} \qquad E_b \geq M_b \qquad \text{otherwise } \texttt{reject} \tag{6.23}$$

otherwise we reject the event. The same process from eq. 6.15 to eq. 6.23 is repeated for the decay of the $\overline{t}$ into a W^- and a $\overline{b}$. Since we have constrained both the t and $\overline{t}$ decay systems by choosing energy and mass values for the decay products, we can impose a global energy conservation by forming the total generated energy E_{gen}, in the event, as

$$E_{gen} = \sqrt{(M_{W^+} + M_b)^2 + P_t^2} + \sqrt{(M_{W^-} + M_{\bar{b}})^2 + P_t^2} \tag{6.24}$$

and imposing that

$$E_{cme} \geq E_{gen} \qquad \text{otherwise } \texttt{reject} \tag{6.25}$$

and otherwise rejecting the event.

The decay of the $t\overline{t}$ pair into W bosons and b-quarks is calculated in the rest frame of the top, boosted by the top momentum. A sketch of this is shown in figure 6.7.

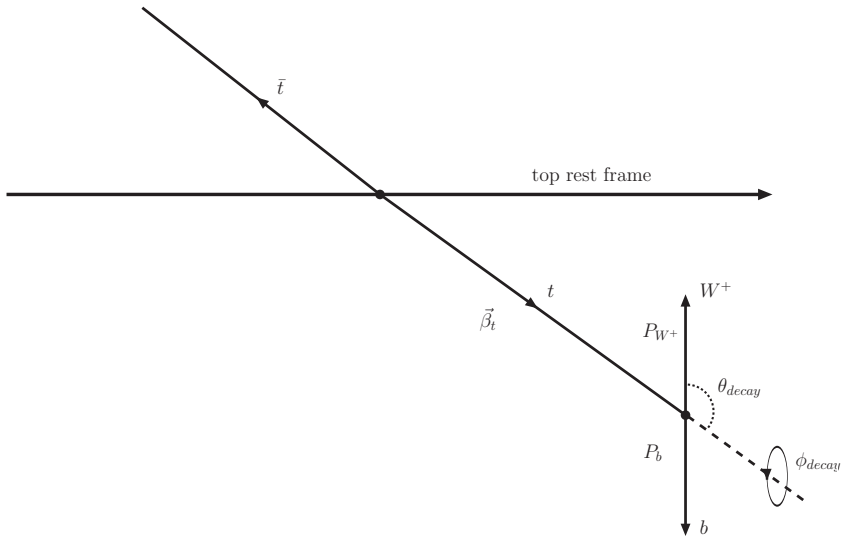

Figure 6.7: Diagram of the decay of the top in the top rest frame

Since we have formed the energy and momentum values for the decay products, we need to calculate the momentum vector. The decay is treated to be isotropic [2] which means that the density of events is proportional to the solid angle, and following the differential element of a solid angle, $d\Omega = d(\cos\theta) \cdot d\phi$, the generation will be uniformly distributed in $\cos\theta_{decay}$ and ϕ_{decay} angles of figure 6.7.

We can form the transverse and longitudinal components of any of the decay products as

$$P_T = P \cdot \sin\theta_{decay} \quad (6.26)$$
$$P_z = P \cdot \cos\theta_{decay} \quad (6.27)$$

and a full description of the decayed 4-vector by the 3-momentum as

$$P_x = P \cdot \cos\phi_{decay} \sin\theta_{decay} \quad (6.28)$$
$$P_y = P \cdot \sin\phi_{decay} \sin\theta_{decay} \quad (6.29)$$
$$P_z = P \cdot \cos\theta_{decay} \quad (6.30)$$

and E_W and E_b determined by eqs. 6.21 or 6.22.

The 4-vector now needs to be boosted by the momentum of the top by using a standard 4-vector boost. For this we need to define

$$E_t = \sqrt{M_t^2 + P_t^2} \quad (6.31)$$
$$\beta_t = P_t/E_t \quad (6.32)$$
$$\gamma_t = E_t/M_t \quad (6.33)$$

and the standard boost formulae

$$E = \gamma_t \cdot (E + \beta_t \cdot P_z) \quad (6.34)$$
$$P_z = \gamma_t \cdot (P_z + \beta_t \cdot E) \quad (6.35)$$

Following this recipe we can calculate the 4-vectors of the W^+ from the decay of the top quark as

$$E^{W^+} = \gamma_t \cdot (E_{W^+} + \beta_t \cdot P_{W^+} \cdot \cos(\theta_t^{decay})) \quad (6.36)$$
$$P_x^{W^+} = \sqrt{P_{W_+}^2 - P_{W^+}^2 \cdot \cos(\theta_t^{decay})^2} \cdot \cos(\phi_t^{decay}) \quad (6.37)$$
$$P_y^{W^+} = \sqrt{P_{W_+}^2 - P_{W^+}^2 \cdot \cos(\theta_t^{decay})^2} \cdot \sin(\phi_t^{decay}) \quad (6.38)$$
$$P_z^{W^+} = \gamma_t \cdot (P_{W^+} \cdot \cos(\theta_t^{decay})^2 + \beta_t \cdot E_{W^+}) \quad (6.39)$$

and the b-quark, generated back-to-back to the W^+ as

$$E^b = \gamma_t \cdot (E_b - \beta_t \cdot P_{W^+} \cdot \cos(\theta_t^{decay})) \quad (6.40)$$

$$
\begin{aligned}
P_x^b &= -P_x^{W^+} && (6.41)\\
P_y^b &= -P_y^{W^+} && (6.42)\\
P_z^b &= \gamma_t \cdot (-P_{W^+} \cdot \cos(\theta_t^{decay}) + \beta_t \cdot E_b) && (6.43)
\end{aligned}
$$

Similarly, for the decay of the $\overline{t}$ into a W^- and a $\bar{b}$-quark and using $\beta_{\bar{t}} = -\beta_t$, the 4-vectors for the W^- are

$$
\begin{aligned}
E^{W^-} &= \gamma_t \cdot (E_{W^-} - \beta_t \cdot P_{W^-} \cdot \cos(\theta_{\bar{t}}^{decay})) && (6.44)\\
P_x^{W^-} &= \sqrt{P_{W_-}^2 - P_{W^-}^2 \cdot \cos(\theta_{\bar{t}}^{decay})^2} \cdot \cos(\phi_{\bar{t}}^{decay}) && (6.45)\\
P_y^{W^-} &= \sqrt{P_{W_-}^2 - P_{W^-}^2 \cdot \cos(\theta_{\bar{t}}^{decay})^2} \cdot \sin(\phi_{\bar{t}}^{decay}) && (6.46)\\
P_z^{W^-} &= \gamma_t \cdot (P_{W^-} \cdot \cos(\theta_{\bar{t}}^{decay}) - \beta_t \cdot E_{W^-}) && (6.47)
\end{aligned}
$$

and for the $\bar{b}$-quark

$$
\begin{aligned}
E^{\bar{b}} &= \gamma_t \cdot (E_{\bar{b}} + \beta_t \cdot P_{W^-} \cdot \cos(\theta_{\bar{t}}^{decay})) && (6.48)\\
P_x^{\bar{b}} &= -P_x^{W^-} && (6.49)\\
P_y^{\bar{b}} &= -P_y^{W^-} && (6.50)\\
P_z^{\bar{b}} &= \gamma_t \cdot (-P_{W^-} \cdot \cos(\theta_{\bar{t}}^{decay}) - \beta_t \cdot E_{\bar{b}}) && (6.51)
\end{aligned}
$$

Finally, all 4-vectors are rotated by angles θ_t and ϕ_t in the spherical polar plane and are boosted by the β and γ of the centre-of-mass system of the collision.

For the rotation, ϕ_t is chosen uniformly in the $[0, 2\pi]$ interval while θ_t (more precisely $\cos\theta_t$) is chosen by the MC integrator according to the S-P wave interference term in the differential cross-section (see chapter 5). Then the rotation follows a standard 3-D rotation in spherical polar coordinates using

$$
\begin{pmatrix} x' \\ y' \\ z' \end{pmatrix} = R \cdot \begin{pmatrix} x \\ y \\ z \end{pmatrix} \qquad (6.52)
$$

with

$$
R = \begin{pmatrix}
\cos\phi\cos\theta\cos\psi - \sin\phi\sin\psi & -\sin\phi\cos\theta\cos\psi - \cos\phi\sin\psi & \sin\theta\cos\psi \\
\sin\phi\cos\psi + \cos\phi\cos\theta\sin\psi & -\sin\phi\cos\theta\sin\psi + \cos\phi\cos\psi & \sin\theta\sin\psi \\
-\cos\phi\sin\theta & \sin\theta\sin\phi & \cos\theta
\end{pmatrix} \qquad (6.53)
$$

and $\psi = 0$.

As the last step of the generation process, all the 4-vectors are boosted longitudinally in the lab frame so as to incorporate any energy asymmetry in the two colliding leptons. For the boost the standard expressions

$$\beta_{cme} = \frac{x_1 E_1 - x_2 E_2}{x_1 E_1 + x_2 E_2} \qquad \text{and} \qquad \gamma_{cme} = 1/\sqrt{1-\beta_{cme}^2} \tag{6.54}$$

and

$$\begin{aligned} E^{boosted} &= \gamma_{cme} \cdot (E + \beta_{cme} \cdot P_z) \\ P_z^{boosted} &= \gamma_{cme} \cdot (P_z + \beta_{cme} \cdot E) \end{aligned} \tag{6.55}$$

are used, such as to incorporate in the generation kinematics the beam effects from the luminosity spectrum energy loss distribution.

6.4.5 Parton Level Comparison with TOPPIK Calculations

To validate the predictions of `ttbarMC`, we must compare it with the explicit calculations of `TOPPIK`. To do this we choose to use the quantities of interest in the measurement of the $t\bar{t}$ threshold, namely the total cross-section $\sigma_{tot}^{t\bar{t}}$, the forward-backward assymetry $\mathrm{A_{FB}}$ and the peak position in the momentum distribution $\mathrm{P_{peak}}$. These three quantities will form the main observables in the threshold measurements but also they provide a good example for comparing the `TOPPIK` and `ttbarMC` calculations as they encode many aspects of the QCD calculations. The momentum distribution depends directly on the shape of the Green functions, $\mathrm{A_{FB}}$ depends on the relative amount of vector and vector/axial-vector current contributions to the differential cross-section and the total cross-section depends on the integral of the differential cross-section.

To perform the comparison, we need to generate events across the top threshold region and compute the values of $\mathrm{A_{FB}}$ and $\mathrm{P_{peak}}$ from the generated samples. The value of the total cross-section used in the generation is given directly by `ttbarMC` at the end of each run. To do this we generate 300k events in steps of 1 GeV in the range $\sqrt{s} = 2M_t \pm 8\,\mathrm{GeV} = 342 - 358\,\mathrm{GeV}$.

The plot of figure 6.8 shows good agreement between the predictions for the total cross-section as calculated from `TOPPIK` and `ttbarMC`.

This is further illustrated in the plots of figure 6.9, where we compare the predictions for $\mathrm{A_{FB}}$ and $\mathrm{P_{peak}}$ respectively. For the calculation of $\mathrm{A_{FB}}$ and $\mathrm{P_{peak}}$ from parton level events we use the methods described in section 7.1.3.

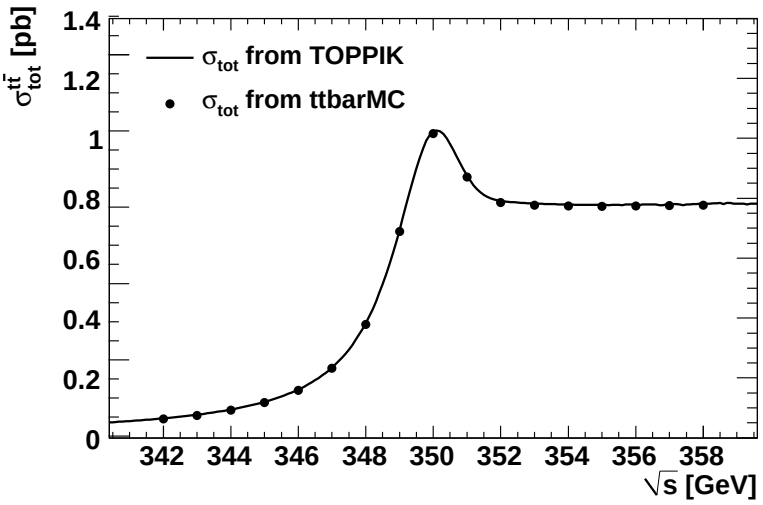

Figure 6.8: Total cross-section predictions from `TOPPIK` and `ttbarMC`.

The agreement between the two calculation methods shows that the implementation of the `TOPPIK` calculations in `ttbarMC` is done in a consistent manner, with the interpolation-based event generation giving the same predictions as the explicit NNLO QCD calculation, while performing the calculation at an event-by-event level.

6.5 `ttbarMC` Interface to Hadronization

So far, the `ttbarMC` event generator described in the previous sections produces parton level events. However, for realistic simulations of the $t\bar{t}$ production threshold, hadron level events are needed such that they can be passed to a detector simulation or compared to real data. For this reason, `ttbarMC` is interfaced with the general purpose hadronization machinary of `Pythia` in order to hadronize the parton level `ttbarMC` output into realistic detector level events.

6.5.1 $t\bar{t}$ Decay Channels

The Standard Model top quark decays almost exclusively into a b quark and a W boson via the weak interaction $t \to \mathrm{W}b$. The decay modes to strange and down quarks are suppressed by the unitarity requirement of the Cabibbo-Kobayashi-Maskawa (CKM) matrix describing the strength of the flavour changing weak interactions, resulting in the decay probability of a top quark to a b quark given by [2]

$$|V_{tb}| = 0.999100^{+0.000034}_{-0.000004} \tag{6.56}$$

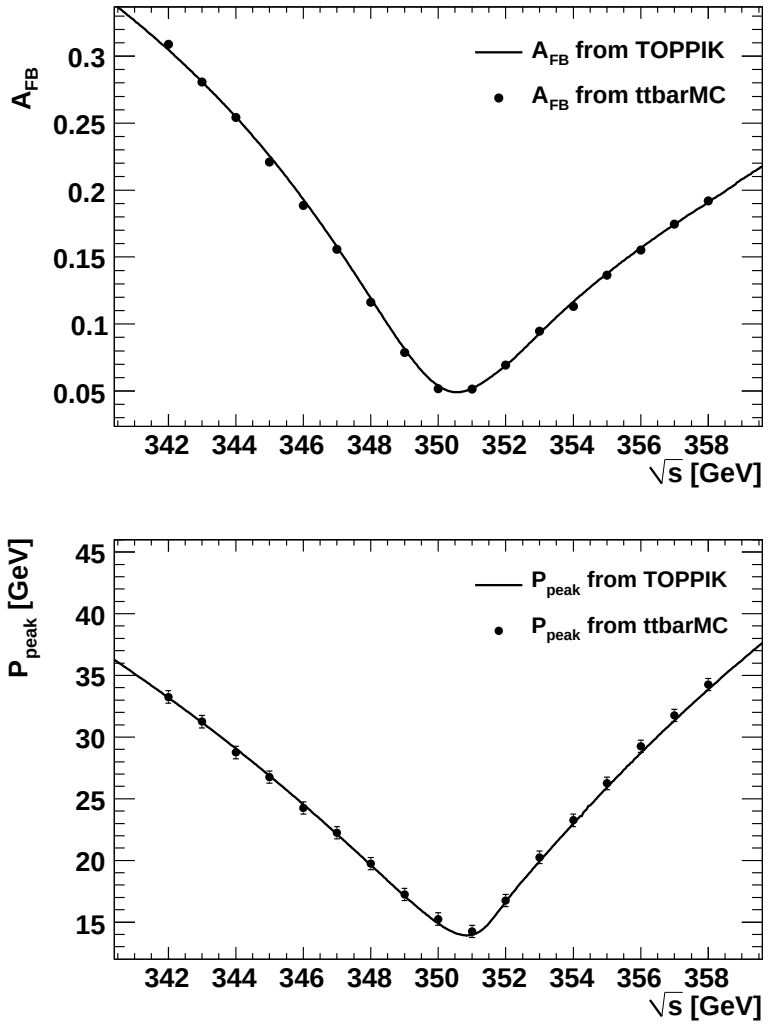

Figure 6.9: A_{FB} (top) and P_{peak} (bottom) predictions as computed by `TOPPIK` and via event generation with `ttbarMC`.

Therefore the decay products of a $t\bar{t}$ pair at threshold are almost exclusively two b quarks and two W bosons. The subsequent final state signatures are dictated by the decay modes of the W bosons.

The W boson can decay into either a lepton and neutrino ($l\bar{\nu}$) or a $q\bar{q}$ pair. Taking into account the three colour combinations of the W $\rightarrow q\bar{q}$ decay mode this leads to 9 different decay configurations. From this the W decays hadronically in 6 out of 9 cases (66.7%) and leptonically in 3 out of 9 cases (33.3%). The decay modes of a pair of W bosons, together with their branching ratios, are summarized in figure 6.10

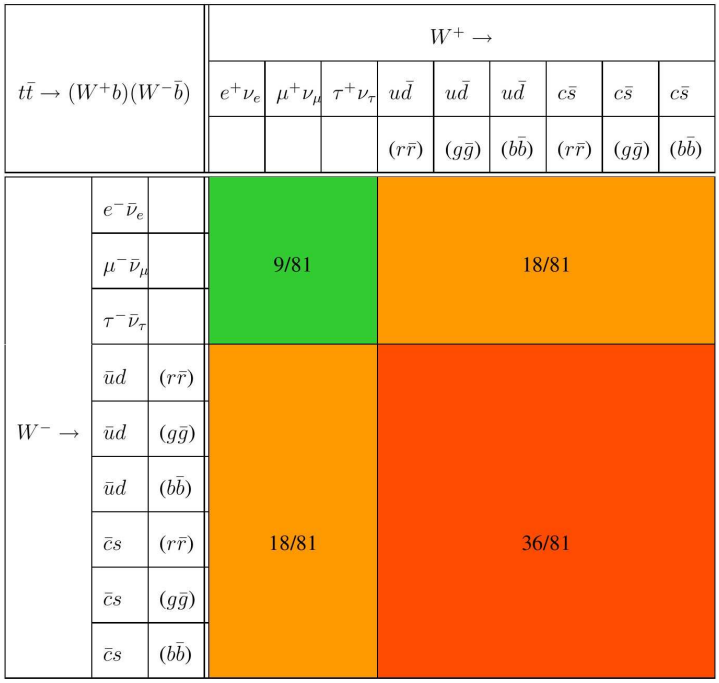

Figure 6.10: Possible decay modes of the two W bosons resulting from $t\bar{t}$ decays. The red box represents hadronic decays, the orange semileptonic decays and the green leptonic decays. Figure from [99].

In the case of the two W bosons from $t\bar{t}$ decays, both W bosons are going to decay into pairs of quarks 44.4% of the times (hadronic decay mode), one W is going to decay into quarks and the other into a lepton + neutrino 44.4% of the times (semileptonic decay mode), and both W bosons are going to decay into leptons 11.1% of the times (leptonic decay mode).

From this, the final state signatures of a $t\bar{t}$ event are :

- Hadronic: two b jets from the b quarks and four jets from the hadronic decays of the W bosons (44.4%)
- Semileptonic: two b jets from the b quarks, two jets from one hadronic W, and a charged lepton (44.4%)

- Leptonic: two b jets from the b quarks and two charged leptons (11.1%)

When excluding the decays of the W to τ leptons, the decay fractions for the semileptonic and leptonic decay modes become 29.6% and 4.9% respectively.

6.5.2 Interface to `Pythia`

The interface to the hadronization machinery of `Pythia` in the context of `ttbarMC` takes place in a similar manner to what is done to the `Pandora` generator by M. Peskin [66]. That is, a record of each generated event from `ttbarMC` is taken, containing the particle-id, four-momenta and parent-daughter relationships, and is passed to the `Pythia` event common block for decay using the `Pythia` machinery.

The b quarks resulting from the decay of the tops are string fragmented and decayed according the default `Pythia` string fragmentation procedure while the heavier W's are passed on to the `Pythia` subroutine `PYRESD` [94] which handles the decay of resonances (and generally heavy unstable particles), including treatement for the chains of succesive decays and parton showers.

The colour flow of the parton level decay products given to `Pythia` to correctly handle the decay colour chain is easily handled since the only coloured objects in each decay leg (i.e. t or $\bar{t}$) are the tops with the colour flowing to the daughter b quarks.

Finally, the hadron level events are output from `Pythia` using the standard `HEPEVT` common block procedures.

6.5.3 Hadron Level Events

The hadron level output of `ttbarMC` is controled by the `Pythia` hadronization machinery as described in the previous section. The generic hadronization procedure allows for the decay of the W bosons and b quarks according to the string fragmentation and hadronization models encoded in `Pythia`. The branching ratios used for choosing between the different decay modes of a $t\bar{t}$ pair (hadronic, semileptonic, leptonic) are also controlled by `Pythia` [5].

The plots of figure 6.11 show the expected energy distributions for the visible energy E_{vis} and transverse energy E_T of 20 k $t\bar{t}$ events as generated with `ttbarMC` and hadronized with the procedure described above. These are in agreement with previous studies looking at these distributions (e.g. [28]), and also with the expectations for

[5] `ttbarMC` also offers the flexibility to choose the decay modes of the two W's resulting from the decay of a $t\bar{t}$ pair.

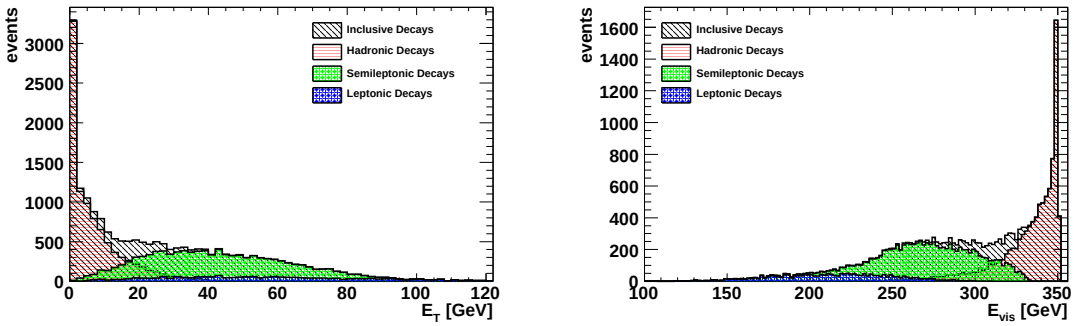

Figure 6.11: E_T (left) and E_{vis} (right) corresponding to 20 k $t\bar{t}$ events (all decay modes included).

the relative population of hadronic, semileptonic and leptonic decay modes according to their branching ratios as described in the previous sections.

Now looking at an example of a fully hadronic $t\bar{t}$ decay, the event topology, as shown in figure 6.12, would require six well separated jets in the calorimeter of a detector. The lego plot of figure 6.13 shows the energy distribution in a detector calorimeter for a six jet $t\bar{t}$ event, illustrating the six well separated energy clusters corresponding to the six jets of the event.

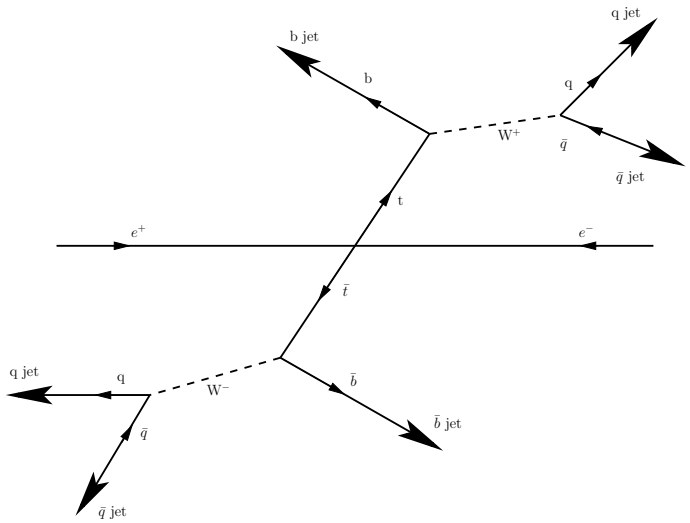

Figure 6.12: Generic event topology of a six jet $t\bar{t}$ event.

In a similar manner, it is verified that all the different decay modes as hadronized by `Pythia`, fulfil the requirements to be treated as detector level $t\bar{t}$ events.

It should be noted that all the quantities shown in this section are hadron level generator based, with no detector effects being applied.

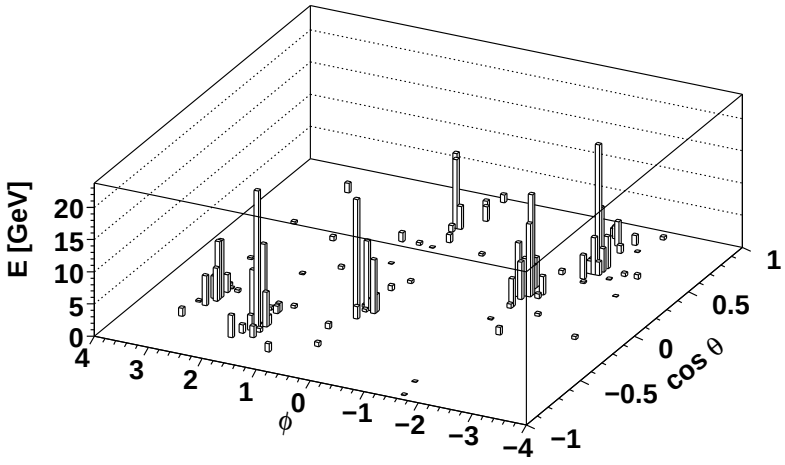

Figure 6.13: Lego plot of how a generic six jet $t\bar{t}$ event would be seen in the calorimeter of a detector.

6.6 Summary

In summary, this chapter described a new Monte Carlo event generator for $t\bar{t}$ production at threshold in e^+e^- collisions. In the beginning of the chapter, a brief introduction to the Monte Carlo method was given, focusing particularly in its uses in particle physics. Then, a review of the top threshold description of some of the most popular general purpose event generators was given, outlining their shortcomings and highliting the need for a more accurate description of the top threshold, based on the calculations described in chapter 5.

Next, a new fast fully differential event generator for $t\bar{t}$ production at threshold was presented, `ttbarMC`, which utilizes sophisticated interpolation techniques for fast generation of $t\bar{t}$ events. The design and layout of the new generator was explained, and a step-by-step description of the phase space integration and event generation kinematics was given, focusing on how one arrives from the quantities calculated by `TOPPIK` (see chapter 5) to parton level events. In addition, the process of explicitly including the effects of the luminosity spectrum in the generation process was also described.

The generation process was checked at the parton level by comparing the parton level distributions produced from the generator, with calculations from `TOPPIK`, demonstrating a good agreement between the theoretical distributions of `TOPPIK`, and the event generator based distributions produced by `ttbarMC`.

Finally, in the last section of this chapter, the interface of `ttbarMC` to the hadronization machinery of `Pythia` was described, and some sample distributions of hadron

level events were presented, illustrating that the generation process of `ttbarMC` is valid.

Chapter 7

Measurement of Top Quark Properties by a Threshold Scan

It has been long known that a linear collider offers the ideal environment for measurements of the top quark properties [79, 78]. In this chapter, the details of how the top quark properties can be measured at a linear collider via a threshold scan are discussed, by describing the different observables that can be used for the measurements, and the method that can be used to extract the top quark mass, width and the strong coupling constant from these observables.

In the later part of this chapter, the impact of the luminosity spectrum on the top quark mass measurement is examined, by using the top threshold simulation code that was described in the previous chapter, combined with the realistic ILC luminosity spectra from the study described in chapter 4, to arrive at an estimate of how the uncertainties in the knowledge of the luminosity spectrum can affect the top quark threshold scan measurements.

7.1 Observables and Multi-Parameter Fits

The most important top quark parameters to be measured at the ILC are the top quark mass M_t, its width Γ_t, and the strong coupling constant α_s. As discussed in chapter 5, the dependence of the top quark cross-section lineshape on these parameters provides an ideal observable for extracting information about these quantities. This can be seen explicitly in the plots of figures 5.1 and 5.2, where the location of the rise and peak position of the cross-section lineshape is directly proportional to the value of the top quark mass. Similarly, the width of the top quark Γ_t, and the strong coupling constant α_s, correspond to changes to the width and height of the resonance-like structure of the cross-section lineshape, thus enabling us to extract information from the lineshape about their values. A plot summarizing the behaviour of the cross-section lineshape according to variations in M_t, Γ_t and α_s can be seen in figure 7.1 (for a detailed account of this behaviour see section 5.3).

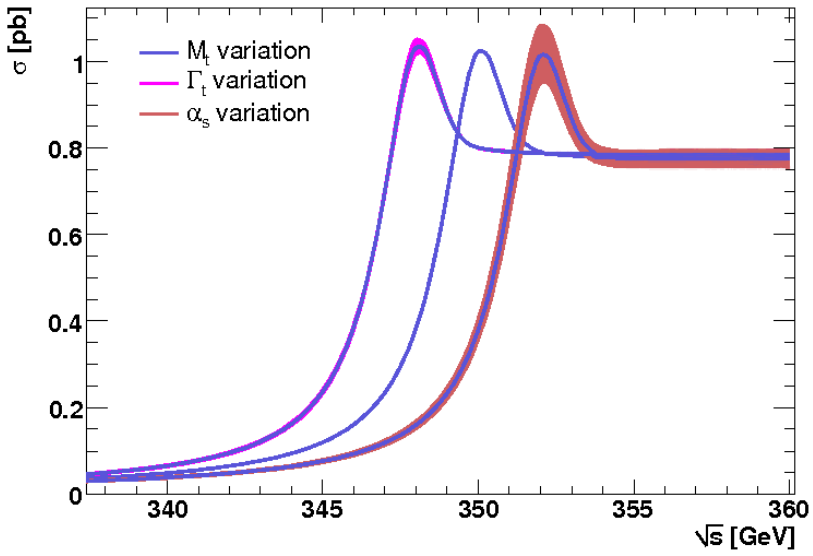

Figure 7.1: Plot illustrating the behaviour of the top threshold cross-section lineshape according to variations in the values of M_t, Γ_t and α_s. For a detailed account of this dependence see section 5.3.

In addition, other distributions such as the forward-backward asymmetry A_{FB} and the peak position of the top quark momentum distribution P_{peak} provide independent observables (to the total cross-section) with a dependence on the top quark parameters, which can be used in a threshold scan to obtain different correlations in the fit distributions hence providing an independent check in the extraction.

7.1.1 Threshold Scan

One of the key features that enables a linear collider to be able to make high precision measurements of the top quark properties is the use of a threshold scan as the measuring technique.

In a threshold scan, the top quark production threshold is scanned in energy, by taking data at various energy points across the expected energy range for the top quark production threshold (at the ILC $\sim 2M_t = 350$ GeV). Then the data are fitted with the theoretical model describing top quark production, in order to extract the top quark parameters best describing the data.

Since the top quark total cross-section lineshape is very sensitive to the top quark parameters, and especially the top quark mass, this further simplifies the measurement since the cross-section can be measured by the counting of colour singlet top quark events, and hence is, to a large extent, unaffected by detector systematics (such as jet energy resolution), which are the limiting factor in the precision reach of measurements in the continuum, as well as in hadron colliders (see section 2.5.2).

In what follows, a $9+1$ point threshold scan strategy is adopted, by which the top quark threshold is scanned at nine equidistant energy points, in steps of 1 GeV, with an extra scan point assumed below threshold for measurement of the backgrounds. It should be noted that this is an unoptimized scan strategy. Improvements in the measurement of the top quark parameters can be expected from an optimized scan strategy, where non equidistant scan points are used, with variable integrated luminosity per point, or with a variable number of scan points. This however is beyond the scope of this thesis, as it is highly dependent on the operational conditions of the accelerator, such as the available integrated luminosity for the top threshold scan, or the ease at which the energy of the accelerator can be tuned for the different scan points. Therefore the standard $9+1$ point threshold scan is adopted, as also used in [30, 31].

7.1.2 $\sigma_{tot}^{t\bar{t}}$ Lineshape

The simulation of the top threshold measurement using the $\sigma_{tot}^{t\bar{t}}$ lineshape is performed using the following procedure. The data are generated by the `ttbarMC` generator, using a full simulation of the luminosity spectrum as described in chapter 4. The luminosity spectrum effects are applied to the data as described in chapter 6. This leads to a full simulation of how parton level events should look like after the effects of the luminosity spectrum but without any detector effects applied. Since no detector simulation was performed, a detector efficiency for selecting top events of 41.2% was

used [30], and no account is taken for background events given the large anticipated signal to background ratio. From this procedure, a number of events for a given amount of luminosity per scan point are selected, including any effects from the luminosity spectrum. The statistical uncertainty on the data sample used for the analysis was the standard Gaussian uncertainty $\sqrt{N}$, where N is the number of the selected events.

The cross-section used in the fitting of the data points in order to determine the values of the top quark parameters is similarly simulated using the full luminosity spectrum, but this time the smearing method is used as in equation 5.35, with the cross-section being interpolated in a large range of the top parameters. This enables the rapid evaluation of the effective cross-section, which is essential for fitting the threshold. The agreement between the generated cross-section using the `ttbarMC` event generated, with that generated from `TOPPIK` with each of the three components of the luminosity spectrum progressively applied can be seen in 7.2.

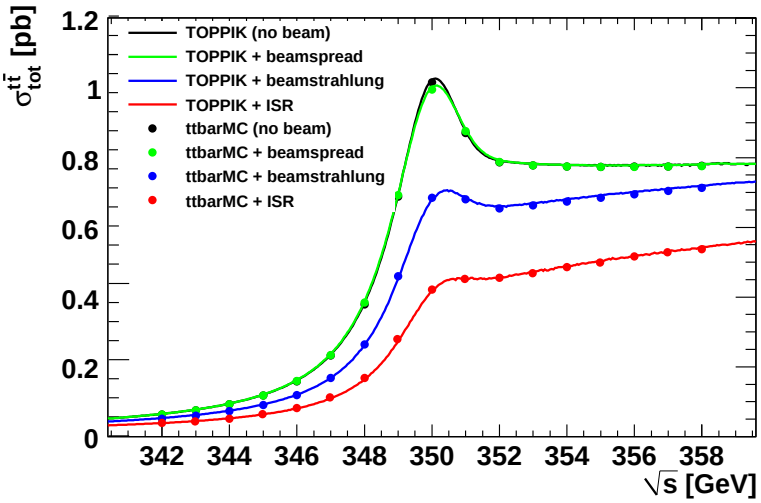

Figure 7.2: Plot of the total cross-section at the threshold region as calculated by `TOPPIK` (solid lines), and `ttbarMC` (data points) for the cases of no beam (black), beamspread (green), beamspread + beamstrahlung (blue), and beamspread + beamstrahlung + ISR (red).

To study the effect of the luminosity spectrum on the fit for the top quark parameters using the $\sigma^{t\bar{t}}_{tot}$ lineshape, the following method is used. The luminosity spectrum used in the evaluation of the 'data' cross-section is the 'true' luminosity spectrum, meaning the spectrum that was simulated and parametrized in chapter 4 from the `GuineaPig++` simulation of the bunch crossings. The 'fit' cross-section is then calculated using the 'measured' luminosity spectrum, meaning the luminosity spectrum including the systematic shifts from the measurement systematics described in chapter 4. This is illustrated in figure 7.3, where a diagram illustrating the two different

methods for the application of the 'data' and 'fit' luminosity spectra is shown.

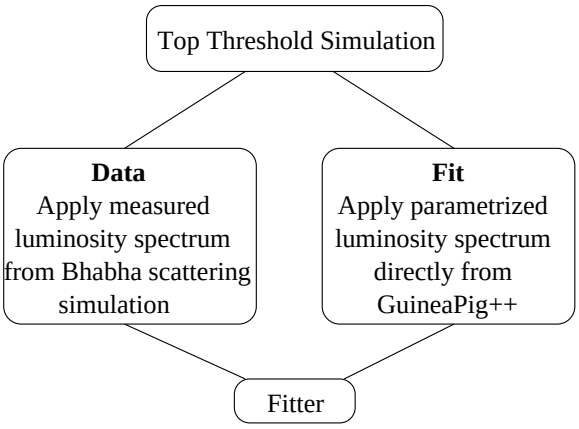

Figure 7.3: Diagram illustrating the luminosity spectrum application procedure on the top threshold for performing a realistic threshold scan simulation.

By fitting the 'measured' cross-section, which would be the cross-section with the measured luminosity spectrum, to the 'true' cross-section, represeting the cross-section with the actual value of the luminosity spectrum, the amount of systematic shift in the top parameters, as well as the correct statistical uncertainty from the fit can be obtained.

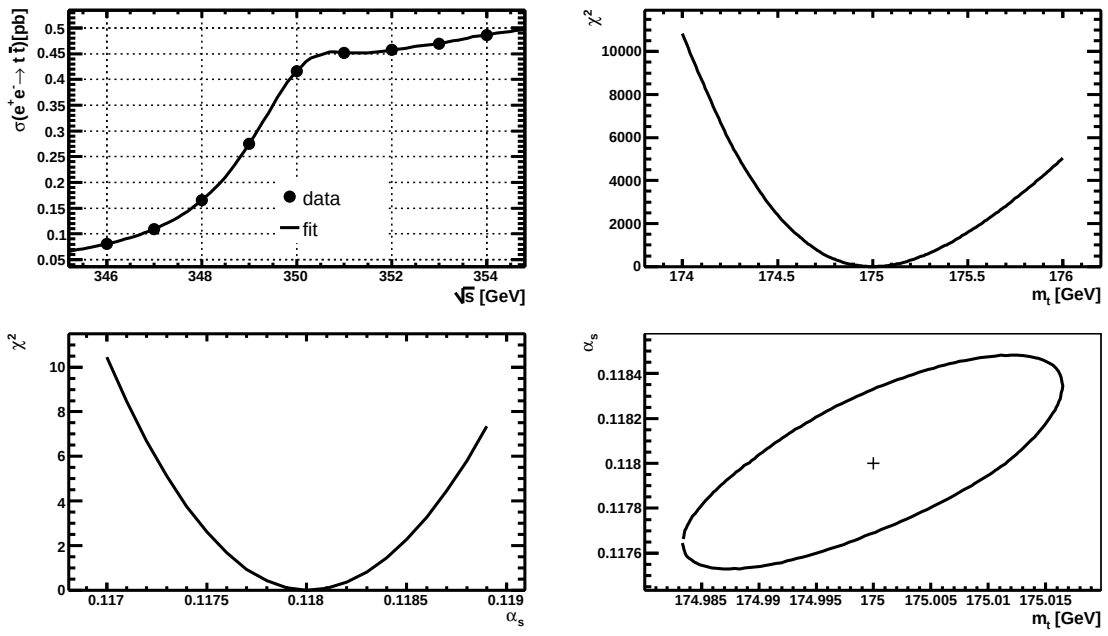

Figure 7.4: Example of a top threshold fit. Top left: example top threshold fit. Top right: χ^2 as a function of the top mass. Bottom left: χ^2 as a function of α_s. Bottom right: 95% confidence contour in the $M_t - \alpha_s$ plane.

The fitting of the top threshold is performed by using a standard two-dimensional

χ^2 fit with M_t and α_s as the free parameters, while keeping Γ_t constant in order to minimize the correlation of Γ_t and α_s in the fit function. This can be easily extended to a three dimensional fit by including Γ_t in the free parameters.

An example of such a fit can be seen in the top left panel of figure 7.4. The χ^2 is also shown as a function of M_t in the top right panel, and α_s in the bottom left panel, with the plot of the bottom right panel showing the correlation between these two parameters with the 95% confidence contour in the $M_t - \alpha_s$ plane.

7.1.3 P_{peak} and A_{FB}

As discussed above, the two other quantities that are useful as observables for the top quark threshold scan are the forward-backward asymmetry A_{FB} and the peak in the momentum distribution of the top quarks P_{peak}.

The forward-backward asymmetry (with respect to the colliding beams) is defined as the asymmetry in the number of events that enter the detector in the left/right hemisphere. So, mathematically A_{FB} is defined as

$$A_{\mathrm{FB}} = \frac{N_{\theta>90^\circ} - N_{\theta<90^\circ}}{N_{\theta>90^\circ} + N_{\theta<90^\circ}} \tag{7.1}$$

where $N_{\theta>90^\circ}$ is the number of final state particles entering the detector at $\theta > 90^\circ$ with respect to the colliding beam axis, and $N_{\theta<90^\circ}$ is the number of final state particles entering the detector in the opposite hemisphere, with the positron direction being the positive axis.

The plot of figure 7.5 shows the forward-backward asymmetry as calculated by `TOPPIK` for the case with no beam effects, together with the same quantity as calculated from parton level generated events using `ttbarMC` and the formula of eq. 7.1. Data points for generated events including the effects of beamstrahlung and ISR are also included in this plot. It can be seen in this plot that as expected, the luminosity spectrum does affect the shape of the distribution by tilting it at higher asymmetry values beneath threshold and lower asymmetry values above threshold.

This is easily explained by the fact that from the effect of the luminosity spectrum, more collisions from lower energies contribute in the effective cross-section, and hence appear in the A_{FB} distribution up to the threshold region. Since there is a minimum in the distribution at threhold, any events existing above threshold get a larger contribution than the minimum value at thresold due to the luminosity spectrum including events at lower energies, hence reducing the overall amount of the asymmetry at energies larger than the threshold.

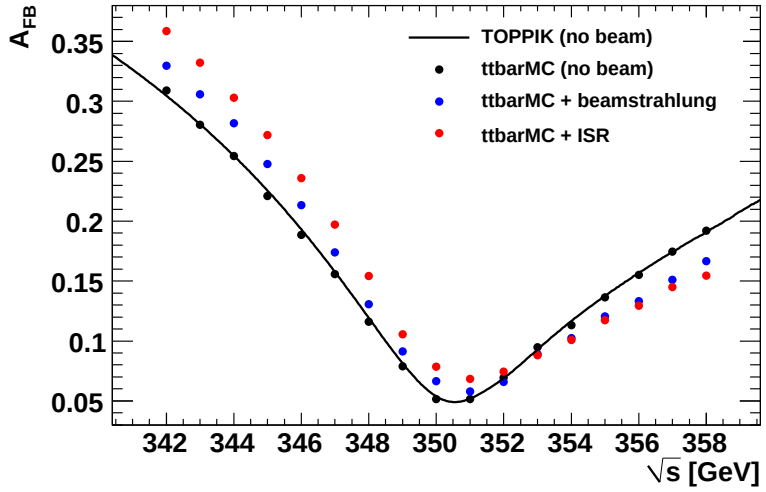

Figure 7.5: A_{FB} distribution at the threshold region as calculated by `TOPPIK` (solid line), and from events generated by `ttbarMC` (data points), for the cases of no beam effect, with beamstrahlung (blue) and with beamstrahlung and ISR (red).

The other useful distribution for the top threshold scan measurements is the distribution of the peak position of the momentum distribution of the top quarks. The dependence of this distribution on the top quark parameters is discussed in section 5.3.

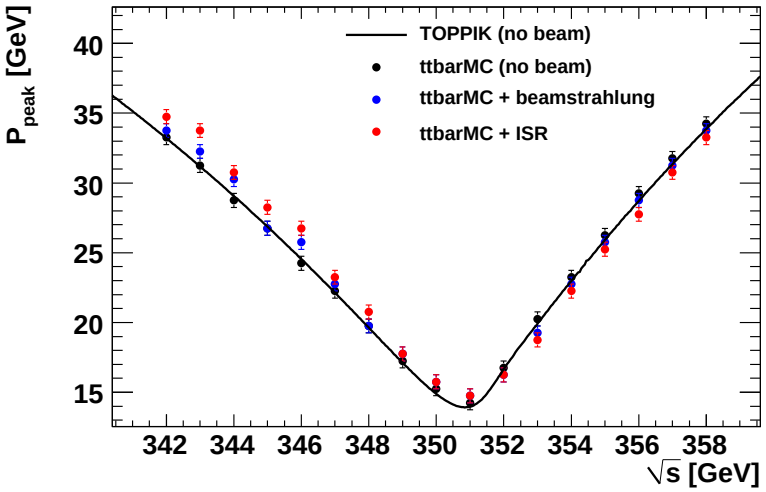

Figure 7.6: P_{peak} distribution at the threshold region as calculated by `TOPPIK` (solid line), and from events generated by `ttbarMC` (data points), for the cases of no beam effect, with beamstrahlung (blue) and with beamstrahlung and ISR (red).

The plot of figure 7.6 shows the P_{peak} at the threshold region as calculated by `TOPPIK` and from events generated by `ttbarMC`, in a similar manner to figure 7.5. The position of the peak in the momentum distribution is calculated by reconstructing

the momentum of the final state partons for each $t\bar{t}$ event, and getting the peak of their momentum distribution.

As can be seen from this plot, the effect of the luminosity spectrum on the P_{peak} distribution is similar to that of A_{FB}, albeit contributing a lesser extent.

From the above it can be seen that although the P_{peak} and A_{FB} distributions are useful observables at the top threshold, they are similarly affected by the luminosity spectrum as is the total cross-section. In addition, to fully study the effect of these distributions on the top quark threshold measurement, they need to be simulated through the stages of hadronization and detector reconstruction, as it is anticipated that they will change significantly when these effects are taken into account. For this reason they are not used in the subsequent analysis of the top quark threshold measurements. However, as demonstrated, all the machinery are now in place for the usage of these distributions in a future detector level study of the top quark production threshold.

7.2 Impact of the Luminosity Spectrum on the $t\bar{t}$ Threshold Measurements

In the previous section, the method for the simulation of the measurement of the top quark threshold was described, explaining the simulation and fitting process. In this section, this method is applied to the scenario of the different accelerator parameter settings that was studied in chapter 4, in order to estimate the effect of the different accelerator settings on the top threshold measurement.

For this study, the cases of chapter 4 for the Nominal, LowN and LowP accelerator settings are used, since the Nominal is the default ILC accelerator setting while the LowN and LowP represent the two extreme settings in terms of the luminosity spectrum measurement study presented in chapter 4, with the LowN parameter set representing the best case scenario for the measurement of the luminosity spectrum, and the LowP parameter set representing the worst case scenario.

The effect of the luminosity spectra produced by the different accelerator settings on the top threshold cross-section can be seen in figure 7.7, where the theoretical prediction for the cross-section is shown, together with the effective cross-section after the effects of the luminosity spectrum have been applied for each of the three accelerator settings.

As it can be seen in this plot, the main effect of the different luminosity spectra is to alter the amount of the effective threshold cross-section. The total cross-section

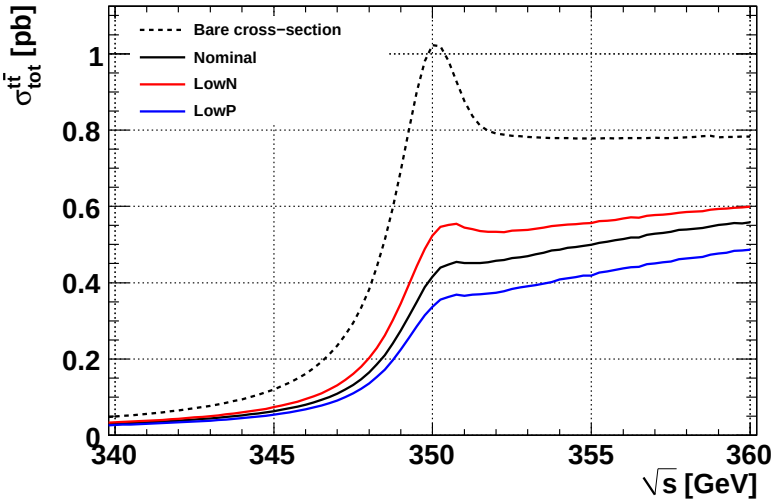

Figure 7.7: Top quark pair production cross-section at threshold region, with the dashed line representing the theoretical prediction for the cross-section, and the solid black, red and blue lines representing the cross-section after taking into account the effect of the luminosity spectrum for the three different accelerator settings, Nominal, LowN and LowP respectively.

in the LowP scenario is about 20% reduced compared to the Nominal while the cross-section in the LowN scenario is about 20% larger. In addition the threshold shape is also changed, with the resonant-like peak structure becoming less visible in the higher beamstrahlung scenarios. This is consistent with the expectation that luminosity spectra with larger amounts of beamstrahlung, such as the LowP case, have a wider distribution at lower-than-nominal energies and hence fewer collisions occur at the top threshold energies, generating a smaller number of $t\bar{t}$ events, thereby reducing the effective cross-section.

The effect of the different accelerator settings on the top threshold affects the threshold scan measurements in two ways. It changes the amount of the effective cross-section for a fixed amount of integrated luminosity per scan point, hence influencing the statistical uncertainty of the measurement, and also affects the systematic uncertainty through the luminosity spectrum associated uncertainty arising from the Bhabha scattering measurement described in chapter 4, creating systematic shifts on the luminosity spectrum parameters.

Both of these effects are studied in the following sections.

7.2.1 Statistical Uncertainty on M_t and α_s

To study the effect of the different luminosity spectra on the statistical uncertainty of the top quark mass measurement, a simulation of three threshold scans for the three different accelerator settings was performed.

In each case, a standard $9 + 1$ threshold scan was used, in the energy range of $346 - 354$ GeV, with the scan points taken at 1 GeV steps. To illustrate the effect that different integrated luminosities per scan point would have on the statistical uncertainty of the measurement of the top quark mass, a range of values from 1 fb^{-1} to 30 fb^{-1} of integrated luminosity per scan point was used. The resulting plot of the statistical uncertainty on M_t due to the different luminosity spectra versus the range of integrated luminosities per scan point can be seen in figure 7.8. It can be seen in this plot that the reduction in effective luminosity clearly increases the statistical uncertainty, and this becomes even more pronounced at the higher beamstrahlung scenario and at low integrated luminosities per scan point.

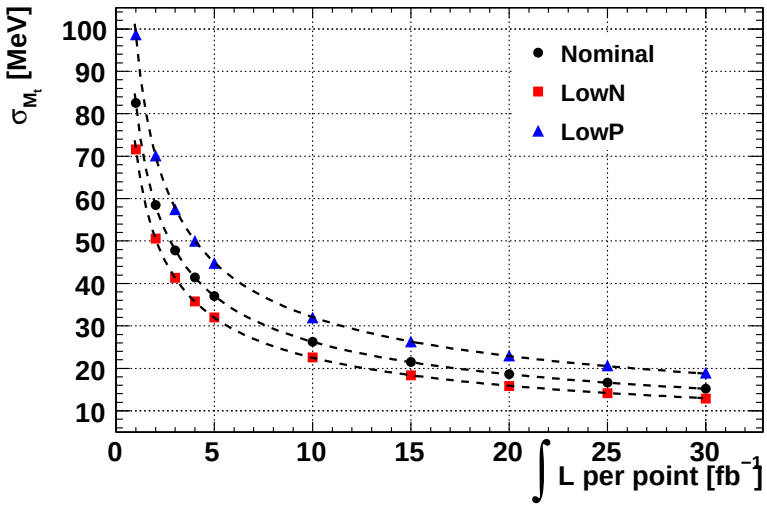

Figure 7.8: Uncertainty on M_t versus integrated luminosity per scan point for the different accelerator parameter sets.

It should be noted that it is possible to further reduce the statistical uncertainty on the threshold measurement for a fixed amount of integrated luminosity per scan point by the use of polarized beams. By assuming SM couplings, the cross-section can be enhanced by a factor of 1.4 relative to the unpolarized case if 80% electron polarization is assumed. Furthermore, if the positron beam is also polarized and by assuming 60% polarization, then the enhancement factor can become approximately 2.1, reducing the required integrated luminosity for the same target statistical precision by about 50% [100].

The plot of figure 7.9 shows the corresponding statistical uncertainty on the measurement of the strong coupling constant α_s for a variable amount of integrated luminosity per scan point. It can be seen in this plot that the different accelerator parameter settings and the amount of integrated luminosity per scan point affect the α_s measurement in a similar manner to that of M_t discussed above.

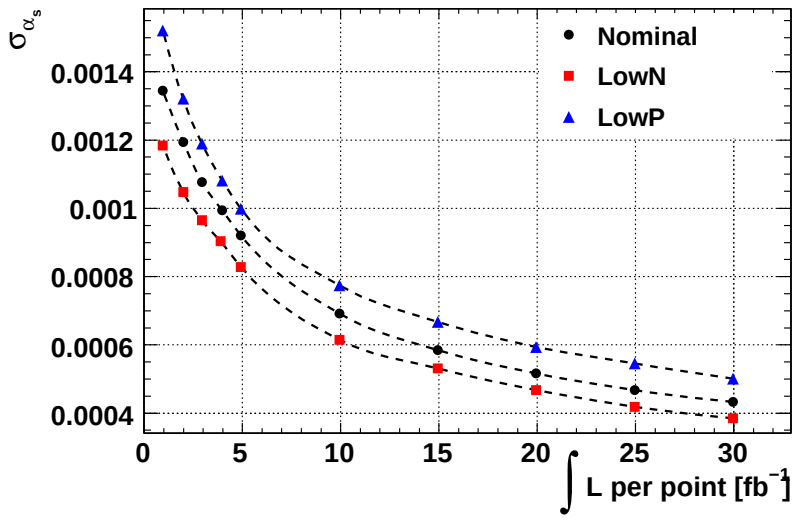

Figure 7.9: Uncertainty on α_s versus integrated luminosity per scan point for the different accelerator parameter sets.

The statistical uncertainty for the α_s measurement through a threshold scan can be compared to the uncertainty on the world average value which is $\Delta\alpha_s = 0.002$ [2][1]. From this it can be seen that in the worst case scenario of the LowP accelerator parameter set with 1 fb^{-1} per scan point, the statistical uncertainty of approximately ± 0.0015 approaches that of the world average of ± 0.002. In the more conservative case of the Nominal parameter set with 10 fb^{-1} per scan point, the statistical uncertainty amounts to about ± 0.0007, about 1/3 of the total uncertainty of the world average.

[1] Quoting the world average value of $\alpha_s(M_Z) = 0.1176 \pm 0.002$ from [2].

7.2.2 Systematic Shifts on M_t and α_s

As discussed in the above section, the statistical uncertainty on the determination of M_t from a threshold scan is minimized for the accelerator parameter set with the smallest amount of beamstrahlung. In addition to this statistical error, the uncertainty in the knowledge of the luminosity spectrum, arising from the luminosity spectrum measurement systematics discussed in chapter 4, is expected to contribute an additional systematic uncertainty to the measurement.

To study the effect of the luminosity spectrum associated systematic shifts in the top threshold scan, a simulation of the threshold measurements was perfomed using the 'measured' values for the luminosity spectrum as summarized in table 4.7. These parametrizations for the luminosity spectrum take into account the expected systematic shifts in the luminosity spectrum from its measurement using Bhabha events.

For the simulation of the 'data' cross-section, 10 fb^{-1} of integrated luminosity per scan point were generated using the luminosity spectrum parameters as summarized in table 4.2. The default top quark parameters of table 5.1 were used for the event generation. The 'fit' cross-section was then simulated using the 'measured' luminosity spectrum parameters of table 4.7, and by following the fit procedure that was described in section 7.1.2, the threshold scan was performed for the three different accelerator parameter sets.

The systematic shifts in the top quark mass arising from the fits of the top threshold are summarized in table 7.1.

Table 7.1: Systematic shifts in M_t due to the systematic uncertainty in the measurement of the luminosity spectrum, given for three different accelerator parameter settings.

Parameter	Nominal	LowN	LowP
M_t	175.010 GeV	174.992 GeV	175.059 GeV
ΔM_t	+ 10 MeV	– 8 MeV	+ 59 MeV

From table 7.1 it can be seen that the effect of more conservative cases for the luminosity spectrum of the Nominal and LowN accelerator parameter sets produce a systematic shift in the top quark mass of 10 and –8 MeV respectively. This is considered to be an acceptable systematic effect given the ILC ambition to perform at top quark mass measurement with an uncertainty in the range of 50–100 MeV. The worst case scenario of the LowP parameter set however produces a systematic shift of 59 MeV, which is already using most of the available budget for the ILC top

mass measurement uncertainty.

Similarly, the systematic shifts in the fit value of the strong coupling constant α_s are given in table 7.2.

Table 7.2: Systematic shifts in α_s due to the systematic uncertainty in the measurement of the luminosity spectrum, given for three different accelerator parameter settings.

Parameter	Nominal	LowN	LowP
α_s	0.11879	0.11754	0.11981
$\Delta\alpha_s$	+ 0.00079	– 0.00046	+ 0.00181

From the systematic shifts in the value of α_s that are summarized in table 7.2, it can be seen that the behaviour of the α_s measurement is similar to that of M_t, with the Nominal and LowN parameter sets producing relatively smaller systematic shifts than that of the LowP parameter set. In the case of α_s, the LowP parameter set produces a systematic shift in the measured value of $\Delta\alpha_s = +0.00181$, which is very close to the uncertainty of the world average value. This alone, combined with the statistical uncertainty would be enough to exceed the world average uncertainty, without taking into account any other possible sources of systematics.

In conclusion, from this study it is shown that the effect of the luminosity spectrum from the different accelerator sets on the top threshold measurement is considered acceptable in the low beamstrahlung scenarios of the Nominal and LowN accelerator parameter sets, while it becomes noticeably larger in the high beamstrahlung accelerator set of LowP, deeming this option as unfavourable for the top quark threshold.

It should be noted however, that while the systematic and statistical uncertainty arising from the LowP accelerator parameter set is noticably larger than its lower beamstahlung counterparts, the amount of uncertainty that it contributes to the measurement of the top quark mass is still more than an order of magnitude less than what is currently achievable at hadron colliders.

7.3 Summary

In this chapter, the principles behind the threshold scan measurement of the top quark properties at the ILC were discussed, by describing the details of how a threshold scan would be performed, and examining the different observables that can be used for the extraction of the top quark parameters.

Focusing on the total cross-section lineshape $\sigma^{t\bar{t}}_{tot}$, the procedure of the threshold scan using a 9+1 scan strategy was described, and an explanation of how the 'data' and 'fit' distributions arise in the simulation was given. An example χ^2 fit between the two was presented, illustrating that the method works for the extraction of the top quark parameters.

The distributions of the forward-backward asymmetry A_{FB} and the peak of the momentum distribution P_{peak} were discussed, illustrating the effects of the luminosity spectrum on them, and how they could be used in the measurement in a future study including a full detector simulation of hadron level events.

To study the impact of the luminosity spectrum, and its associated measurement uncertainty on the top threshold scan, three cases of luminosity spectra for different accelerator parameter sets were used, namely the Nominal, LowP and LowN parameter sets that were described in chapter 4.

The effect of the different parameter sets on the total cross-section was identified, and a study of the associated statistical and systematic uncertainty on the top threshold measurement was perfomed. It was found that as expected, the statistical uncertainty on the measured values of M_t and α_s increases as a function of the amount of beamstrahlung in the different accelerator parameter sets, with the LowN parameter set giving the smallest uncertainty and LowP giving the largest uncertainty. In addition, this study was performed for a variable value of the integrated luminosity per scan point of the threshold scan, quantifying the effect of the integrated luminosity per scan point on the statistical uncertainty of the measurement.

Finally, a study of the systematic shifts in the values of the measured top quark parameters was performed, arising from the uncertainty associated with the measurement of the luminosity spectrum as described in chapter 4. Again it was found that the Nominal and LowN accelerator parameter sets produce acceptable systematic shifts of 10 and –8 MeV respectively in the value of the top quark mass, while the high beamstrahlung scenario of the LowP case produces a shift of 59 MeV deeming this option as unfavourable for the top quark threshold scan. Similar results were produced for the measurement of the strong coupling constant α_s.

Chapter 8

Summary and Outlook

In this thesis a study of the top quark production threshold was presented, by focusing on the relationship between the top quark measurement at a future linear collider via a threshold scan, to the machine's luminosity spectrum, and the effects it can have on the threshold measurements.

The luminosity spectrum was studied in detail in chapter 4, by looking at how it arises, how it can be parametrized and then measured using Bhabha scattering events. A new method for its parametrization was developed, explicitly taking into account the effect of beamspread in the fit parameters of the spectrum. Then a study of the measurement of the luminosity spectrum was performed, by using a simulation of the Bhabha scattering process as the measurement method, and detailing all the effects and assumptions that are used in the measurement. Tools were developed for looking at systematic effects in the luminosity spectrum measurement arising from detector and beam-beam effects, by using a modified version of the simulation code `GuineaPig++`, where the Bhabha scattering events were incorporated in the `GuineaPig++` simulation of the bunch crossing in order to study the way that beam-beam effects affect the Bhabha scattering measurement. Finally, a simulation of the luminosity spectrum measurement for the different possible ILC accelerator parameter settings, as described in the RDR [27] was presented, and the effects of the different amounts of beamstrahlung in the different accelerator settings were identified.

It was found that due to the varying amounts of beamstrahlung in the luminosity spectra of the different accelerator parameter sets, the systematic shifts in their measured values vary from approximately 10 MeV of average beam energy shift in the case of the low beamstrahlung scenarios of the LowN and Nominal accelerator parameter sets, up to approximatelly 1275 MeV in the case of the high beamstrahlung scenario

of the LowP parameter set. This identified that the large shifts in the measured parameter of the luminosity spectrum in the LowP accelerator parameter set led to a large bias in the luminosity spectrum measurement and hence deem this accelerator setting as unfavourable when precision knowledge of the luminosity spectrum is required.

The next section of this thesis looked at the problem of the existing simulations of the top quark production threshold by identifing the need for a new fully differential Monte Carlo event generator for $t\bar{t}$ production. Current state-of-the-art calculations including NNLO QCD corrections were described, and a method for incorporating them in a new fast and fully differential event generator was identified, by the use of fast multidimensional interpolation techniques in order to achieve the necessary speed in the generation process for efficient Monte Carlo studies of the top threshold.

A detailed account of all the stages of the Monte Carlo generator was given, by describing the interpolation, phase space integration, generation kinematics and hadronization used in the event generation. The event generator is focused towards the correct inclusion of the luminosity spectrum in the generation process, both in the total cross-section but also in the angular and momentum distributions of the final state particles, in order to provide a precision tool for future detailed studies of the top quark threshold measurements.

Finally, in the final part of the thesis, the new event generator was used to simulate the top quark threshold, examining the effects of the luminosity spectrum on the threshold observables. A study of the statistical and systematic uncertainties on the top quark measurements was performed by looking at how the luminosity spectra for the ILC accelerator parameter sets influence the top quark measurements. It was found that both the statistical and the systematic uncertainties arising in the high beamstrahlung scenario of the LowP accelerator parameter set are considerably larger than the Nominal and LowN parameter sets, making the LowP parameter set unfavourable for the top threshold measurements.

In summary, this thesis contributed to the present status of studies of the top quark measurement in a future linear collider by the method of a threshold scan by :

- Studied the parametrization and simulation of the luminosity spectrum by using a new technique for the parametrization including the beam energy spread in the fit parameters. This enables for a more realistic description of the luminosity spectrum that was used in the simulations of chapter 4, and can also be used in future simulations where a parametrization of the luminosity spectrum is required.

- Performed parametrizations for the luminosity spectra for the different ILC RDR accelerator parameter sets.

- Included the new parametrization in the simulation of the luminosity spectrum using Bhabha scattering events, and provided a study of the measurement of the luminosity spectrum for all the different ILC accelerator parameter sets.

- Using a more realistic approach to the Bhabha scattering simulations, a study of the systematic effects that arise in the measurement of the luminosity spectrum from the beam dynamics that take place at the IP was performed, by using a modified version of the bunch crossing simulation code `GuineaPig++`, where the Bhabha events were passed through the bunch crossing simulation, and the systematic effects on the final state particles, and by extension the measured luminosity spectrum, were studied.

- Presented a fast and fully differential new Monte Carlo event generator for $t\bar{t}$ production at threshold, overcoming a long standing problem in the simulation of the top quark threshold measurement. This event generator takes into account an explicit description of the luminosity spectrum as detailed above, and will provide an essential tool in every future simulation of the top quark production threshold.

- Studied the effects of the luminosity spectrum on the top quark threshold measurements by the method of a threshold scan, and identified the relevant statistical and systematic uncertainties on the top measurements arising from the luminosity spectra of the different ILC accelerator parameter sets.

The future program for the research of the top quark production threshold at the ILC, based on the work and tools developed in this thesis, can be identified as taking this simulation to the next level by including a detector level study of both the luminosity spectrum measurement using Bhabha events, and the top threshold measurements using a threshold scan.

For the luminosity spectrum measurement study, the new parametrization, measurement technique, and `GuineaPig++` simulation of the beam-beam effects can be used directly in a detector level study, in order to provide a complete picture of the uncertainties associated with the measurement of the luminosity spectrum at the ILC or other future linear colliders.

For future studies of the top quark threshold measurements, the new Monte Carlo event generator `ttbarMC` can be used for the simulation of top quark production

and decay, enabling a detector level study of the top quark threshold measurement by using a realistic theoretical description of the top quark threshold, including the angular and momentum distributions of the top quarks, and a realistic description of the luminosity spectrum, and how it affects the threshold measurement.

List of Figures

2.1 Diagram [3] of the SM fermions (divided into the three generations) and bosons, with the Higgs particle being the only particle yet to be discovered. The masses of the neutrinos are upper limits. 13
2.2 Summary plot of the latest measured values (July 2008) and the world average for the top quark mass [20]. 18
2.3 One-loop radiative corrections to the W and Z boson masses due to the top quark. 19
2.4 Virtual Higgs boson loops contributing to the W and Z boson masses. . 20
2.5 *Left:* Contour plot of the dependence of the Higgs mass prediction on the measured values of the top quark and W boson mass. *Right:* Plot of the dependence of the top quark mass on the Higgs mass with the yellow area being excluded from direct searches at LEP, and the blue ellipse indicating the best fit to all electroweak data. Both from [20]. 20
2.6 Feynman diagrams contributing to the cancellation of the quadratic terms in the renormalization of the Higgs boson mass between a fermionic top quark loop and a bosonic stop quark loop. 21
2.7 Contour plot of the dependence of different SUSY models on the measured values of the top quark and W boson at current and future collider experiments. Updated from [22]. 22
2.8 Feynman diagram for $t\bar{t}$ production at a linear collider. 26
2.9 Energy dependence of the $t\bar{t}$ production cross-section in the threshold region (with no experimental effects applied). 26

3.1 Schematic diagram of the current baseline design for the ILC corresponding to a machine with 500 GeV centre-of-mass energy [40]. 29
3.2 A comparison of the four detector concepts, indicating the main differences and similarities between the different designs. Adapted from [52]. 37

4.1 Diagram showing the cross-section of a generic ILC detector, with the LumiCal in the forward region. 42
4.2 Schematic of the magnetic chicane for the ILC upstream energy spectrometer [58]. 44
4.3 The three components of the luminosity spectrum for a centre-of-mass energy of 350 GeV, including a BES of 0.1%. 47
4.4 The beamstrahlung spectra, as computed with `Guinea-Pig++`, for the four different accelerator parameter settings defined in the ILC RDR operational parameter plane [27] (summarised in table 4.1). All spectra include a 0.1% beam energy spread and each spectrum corresponds to the amount of beamstrahlung averaged over 10 `Guinea-Pig++` runs with identical initial conditions. 49
4.5 A sample fit of the function of eq. 4.17 to a `Guinea-Pig++` beamstrahlung spectrum including a Gaussian distributed beam energy spread with a σ of 0.1%. The histogram corresponds to the beamstrahlung spectrum for 10 `Guinea-Pig++` runs with identical initial conditions. 52
4.6 Plot showing a sample beamstrahlung spectrum as calculated from `Guinea-Pig++` overlayed with a generated spectrum based on the parameterization of the `Guinea-Pig++` simulation. 52
4.7 Lowest order Feynman diagrams for s- and t-channel Bhabha scattering. 53
4.8 Total Bhabha scattering cross-section as a function of centre-of-mass energy (left), and integrated scattering cross-section at $\sqrt{s}$= 350 GeV as a function of scattering angle (right). 54
4.9 Schematic diagram of Bhabha scattering with single photon radiation. The scattering angles are defined as θ_e and θ_p and the acollinearity angle as θ_A. 54
4.10 Final state distributions for scattering angles θ (top left) and ϕ (top right), and the scaled energy (bottom left) of Bhabha events generated at $\sqrt{s}$= 150, 250 and 350 GeV. The scaled energy E/E_{gen} is the energy of the final state particle divided by the beam energy used for the generation. . . . 57
4.11 The variation of the beamstrahlung spectrum with respect to the default for individual changes in the three a_i parameters. 58
4.12 The effect of beam energy spread around the peak of the spectrum due to the folding caused by the reconstruction assumption $\sqrt{s'} < \sqrt{s}$. 58
4.13 Minimized fit function (top left) and χ^2 minimization for the three beamstrahlung parameters. 60
4.14 Reconstructed versus true x, for the Nominal ILC parameters. 61

4.15 Polar angle resolution of the forward tracking system of the TESLA detector [76]. 62
4.16 Schematic of the interaction of two bunches with a Bhabha scattering event produced. The dotted lines indicate the ideal initial and final state particles and the solid lines their path underlining the (magnified) effect due to the presence of the bunches. 63
4.17 Plot of amount of deflection versus undeflected angles for different minimum Bhabha production angles. θ_2 is the scattering angle after deflection and θ_1 is before. 66
4.18 Distribution of the difference in the final state scattering angles due to the EM deflection effect for Bhabha events produced with a minimum angle of 7°. 66
4.19 Difference in final state θ with and without the initial state transverse boost as a function of the acollinearity. θ_{P_T} are angles with transverse boost and $\theta_{P_T=0}$ are without. 68
4.20 Distribution of the difference of the final state angles of Bhabha events due to the initial state transverse boost. 69
4.21 Transverse boost effect on the reconstructed x_{acol}. 69

5.1 Total cross-section for $t\bar{t}$ production at threshold for different values of the top quark mass. 84
5.2 Total cross-section for $t\bar{t}$ production at threshold for different values of the top quark width (left) and strong coupling constant (right). 85
5.3 Top quark momentum distribution at $\sqrt{s} = 349$ GeV for different values of M_t (solid line versus dashed line) and α_s (three dashed/solid lines correspond to three different α_s values). 85
5.4 P_{peak}(left) and A_{FB}(right) dependence on the top quark mass, the top quark width and the strong coupling constant (from top to bottom). 87
5.5 Total cross-section smeared by the three components of the luminosity spectrum (as in figure 4.3). 89

6.1 Total cross-section predictions from standard multi-purpose LO calculations from `Pythia`, `Herwig` and `Pandora` and NNLO QCD prediction from `TOPPIK`. 94
6.2 Schematic layout of `ttbarMC`. 97

6.3 The S-wave Green function is shown for different values of $\sqrt{s}$, with $|k_t|$ being the magnitude of the top quark's three momentum vector. The plot on the left shows the real part (solid) and magnitude (dashed) of the Green function while the plot on the right shows the imaginary part (solid) and phase (dashed) component. 99
6.4 Linear interpolation in-between grid points 99
6.5 Difference plots for the real and imaginary parts of the S-wave Green function for 300 different $\sqrt{s}$ uniformly distributed in the $\sqrt{s} = 2M_t \pm$ 8GeV range, as computed with `TOPPIK` and the interpolator. The RMS of the distributions is ~ 0.005. 100
6.6 Total cross-section predictions from `TOPPIK` and interpolation based calculations (left) and the fractional difference of the two calculations (right). 100
6.7 Diagram of the decay of the top in the top rest frame 106
6.8 Total cross-section predictions from `TOPPIK` and `ttbarMC`. 110
6.9 A_{FB} (top) and P_{peak} (bottom) predictions as computed by `TOPPIK` and via event generation with `ttbarMC`. 111
6.10 Possible decay modes of the two W bosons resulting from $t\bar{t}$ decays. The red box represents hadronic decays, the orange semileptonic decays and the green leptonic decays. Figure from [99]. 112
6.11 E_T (left) and E_{vis} (right) corresponding to 20 k $t\bar{t}$ events (all decay modes included). 114
6.12 Generic event topology of a six jet $t\bar{t}$ event. 114
6.13 Lego plot of how a generic six jet $t\bar{t}$ event would be seen in the calorimeter of a detector. 115

7.1 Plot illustrating the behaviour of the top threshold cross-section lineshape according to variations in the values of M_t, Γ_t and α_s. For a detailed account of this dependence see section 5.3. 118
7.2 Plot of the total cross-section at the threshold region as calculated by `TOPPIK` (solid lines), and `ttbarMC` (data points) for the cases of no beam (black), beamspread (green), beamspread + beamstrahlung (blue), and beamspread + beamstrahlung + ISR (red). 120
7.3 Diagram illustrating the luminosity spectrum application procedure on the top threshold for performing a realistic threshold scan simulation. . . . 121
7.4 Example of a top threshold fit. Top left: example top threshold fit. Top right: χ^2 as a function of the top mass. Bottom left: χ^2 as a function of α_s. Bottom right: 95% confidence contour in the $M_t - \alpha_s$ plane. 121

7.5 A_{FB} distribution at the threshold region as calculated by `TOPPIK` (solid line), and from events generated by `ttbarMC` (data points), for the cases of no beam effect, with beamstrahlung (blue) and with beamstrahlung and ISR (red). 123
7.6 P_{peak} distribution at the threshold region as calculated by `TOPPIK` (solid line), and from events generated by `ttbarMC` (data points), for the cases of no beam effect, with beamstrahlung (blue) and with beamstrahlung and ISR (red). 123
7.7 Top quark pair production cross-section at threshold region, with the dashed line representing the theoretical prediction for the cross-section, and the solid black, red and blue lines representing the cross-section after taking into account the effect of the luminosity spectrum for the three different accelerator settings, Nominal, LowN and LowP respectively. . . 125
7.8 Uncertainty on M_t versus integrated luminosity per scan point for the different accelerator parameter sets. 126
7.9 Uncertainty on α_s versus integrated luminosity per scan point for the different accelerator parameter sets. 127

List of Tables

3.1 Basic design parameters for the ILC with 500 GeV centre-of-mass energy [27]. 29
3.2 Beam and IP parameter plane for a 500GeV machine [27] 33

4.1 Beam and IP parameters for the different settings of the ILC RDR operational parameter plane [27] that are related to beamstrahlung. Based on accelerator parameters of table 3.2. 50
4.2 Beamstrahlung fit parameters, for the ILC RDR parameter plane spectra of figure 4.4. 51
4.3 Default fit parameters and associated statistical errors for a fit on a 1788 k Bhabha sample corresponding to 3 fb^{-1} of luminosity. The beamstrahlung spectrum used corresponds to the Nominal machine parameter set, with the other parameter sets giving similar results. 59
4.4 Systematic shift in beamstrahlung parameters due to smearing the 'measured' data sample with a Gaussian detector resolution of $\sigma = 0.03$ mrad. Default values and statistical errors are similar to table 4.3. 62
4.5 Extracted values and shifts of the beamstrahlung parameters due to the effect of microscopic beamstrahlung on the 'measured' data sample. The shifts are relative to the default values of table 4.4. 65
4.6 Extracted values and shifts of the beamstrahlung parameters due to the effect of EM deflections on the final state Bhabha particles. The shifts are relative to the default values of table 4.4. 67
4.7 Extracted values and shifts in the beamstrahlung parameters due to the effect of the transverse momentum components of the initial state e^+e^-. The shifts are relative to the default values of table 4.4. 70

5.1 Default `TOPPIK` input parameters used throughout this thesis (unless otherwise stated). 83

7.1 Systematic shifts in M_t due to the systematic uncertainty in the measurement of the luminosity spectrum, given for three different accelerator parameter settings. 128
7.2 Systematic shifts in α_s due to the systematic uncertainty in the measurement of the luminosity spectrum, given for three different accelerator parameter settings. 129

References

[1] S. Weinberg, *The Making of the Standard Model*, Eur. Phys. J. **C34**, 5 (2004), arXiv:hep-ph/0401010.

[2] Particle Data Group, C. Amsler et al, *Review of Particle Physics*, Phys. Lett. **B667**, 1 (2008).

[3] G. Kane, *The Dawn of Physics Beyond the Standard Model*, Scientific American, 68 (2003).

[4] Super-Kamiokande Collaboration, T. Kajita et al., *Atmospheric neutrino results from Super-Kamiokande and Kamiokande: Evidence for nu/mu oscillations*, Nucl. Phys. Proc. Suppl. **77**, 123 (1999), arXiv:hep-ex/9810001.

[5] MINOS Collaboration, P. A. Adamson et al., *Measurement of Neutrino Oscillations with the MINOS Detectors in the NuMI Beam*, Phys. Rev. Lett. **101**, 131802 (2008), arXiv:hep-ex/08062237.

[6] F. Halzen and A. D. Martin, *Quarks and Leptons: An Introductory Course in Modern Particle Physics* New York: Wiley, (1984).

[7] J. R. Ellis, M. K. Gaillard, and D. V. Nanopoulos, *A Phenomenological Profile of the Higgs Boson*, Nucl. Phys. **B106**, 292 (1976).

[8] LEP Working Group for Higgs Boson Searches, R. Barate et al., *Search for the standard model Higgs boson at LEP*, Phys. Lett. **B565**, 61 (2003), arXiv:hep-ex/0306033.

[9] C. Quigg, *The state of the Standard Model*, (1999), arXiv:hep-ph/0001145.

[10] LHC/LC Study Group, G. Weiglein et al., *Physics interplay of the LHC and the ILC*, Phys. Rept. **426**, 47 (2006), arXiv:hep-ph/0410364.

[11] N. V. Krasnikov, *The problem of hierarchy and a possible new physics at the scale of 1-TeV*, The First International Triangle Workshop: Standard Model and Beyond, from LEP to UNK and LHC, Dubna, USSR, 1-5 Oct 1990.

[12] J. H. Christenson, J. W. Cronin, V. L. Fitch, and R. Turlay, *Evidence for the 2 π Decay of the K_0^2 Meson*, Phys. Rev. Lett. **13**, 138 (1964).

[13] BaBar Collaboration, J. T. Boyd et al., *Direct CP violation and rare decays at BaBar*, Nucl. Phys. Proc. Suppl. **156**, 52 (2006).

[14] C. L. Bennett et al., *The Microwave Anisotropy Probe Mission*, The Astrophysical Journal **583**, 1 (2003), arXiv:astro-ph/0301158.

[15] G. Bertone, D. Hooper, and J. Silk, *Particle Dark Matter: Evidence, Candidates and Constraints*, Physics Reports **405**, 279 (2005).

[16] P. J. E. Peebles and B. Ratra, *The cosmological constant and dark energy*, Rev. Mod. Phys. **75**, 559 (2003).

[17] S. Dimopoulos and H. Georgi, *Softly Broken Supersymmetry and SU(5)*, Nucl. Phys. **B193**, 150 (1981).

[18] L. Alvarez-Gaume, J. Polchinski, and M. B. Wise, *Minimal Low-Energy Supergravity*, Nucl. Phys. **B221**, 495 (1983).

[19] Tevatron Electroweak Working Group, *Combination of CDF and D0 Results on the Mass of the Top Quark*, (2008), arXiv:hep-ex/08081089.

[20] LEP Electroweak Working Group, *Precision Electroweak Measurements and Constraints on the Standard Model*, (2008), arXiv:hep-ex/08114682.

[21] S. Willenbrock, *The standard model and the top quark*, (2002), arXiv:hep-ph/0211067.

[22] S. Heinemeyer, W. Hollik, D. Stockinger, A. M. Weber, and G. Weiglein, *Precise prediction for M(W) in the MSSM*, JHEP **08**, 052 (2006), arXiv:hep-ph/0604147.

[23] S. Heinemeyer and G. Weiglein, *Physics gain of a precise m(t) measurement*, (2005), arXiv:hep-ph/0508168.

[24] F. Richard, J. R. Schneider, D. Trines, and A. Wagner (editors), *TESLA Technical Design Report*, (2001), arXiv:hep-ph/0106314.

[25] NLC ZDR Design Group and NLC Physics Working Group, S. Kuhlman et al., *Physics and technology of the Next Linear Collider: A Report submitted to Snowmass '96*, (1996), arXiv:hep-ex/9605011.

[26] Asian Committee for Future Accelerators (ACFA), Japan High Energy Physics Commitee (JHEPC), High Energy Accelerator research Organisation (KEK), *GLC project: Linear collider for TeV physics*, KEK-REPORT-2003-7. (2003)

[27] J. Brau (editor) et al. *International Linear Collider Reference Design Report*, (2007), ILC-REPORT-2007-001.

[28] K. Fujii, T. Matsui, and Y. Sumino, *Physics at $t\bar{t}$ threshold in e+e− collisions*, Phys. Rev. D **50**, 4341 (1994).

[29] D. Peralta, R. Miquel, and M. Martinez, *Top mass measurement at the t anti-t threshold*, The 4th International Workshop on Linear Colliders (LCWS 99), Sitges, Barcelona, Spain, 28 Apr - 5 May 1999.

[30] M. Martinez and R. Miquel, *Multi-parameter fits to the t anti-t threshold observables at a future e+ e- linear collider*, Eur. Phys. J. **C27**, 49 (2003), arXiv:hep-ph/0207315.

[31] S. Boogert, *Luminosity spectra and the top threshold*, Talk given at LCWS '04, Paris, April 2004.

[32] E. V. Khramov, A. N. Tonoyan, V. A. Bednyakov, and N. A. Rusakovich, *Top quark from the Tevatron to LHC*, Phys. Part. Nucl. **39**, 74 (2008).

[33] S. V. Chekanov and V. L. Morgunov, *Selection and reconstruction of the top quarks in the all- hadronic decays at a linear collider*, Phys. Rev. **D67**, 074011 (2003), arXiv:hep-ex/0301014.

[34] S. V. Chekanov, *Uncertainties on the measurements of the top mass at a future e+ e- collider*, (2002), arXiv:hep-ph/0206264.

[35] V. A. Khoze and T. Sjostrand, *QCD interconnection studies at linear colliders*, Eur. Phys. J. direct **C2**, 1 (2000), arXiv:hep-ph/9912297.

[36] A. Hoang, et al., *Top-antitop pair production close to threshold: Synopsis of recent NNLO results*, Eur. Phys. J. direct **C2**, 1 (2000), arXiv:hep-ph/0001286.

[37] A. H. Hoang and T. Teubner, *Top-quark pair production close to threshold: Top-quark mass, width, and momentum distribution*, Phys. Rev. D **60**, 114027 (1999).

[38] ICFA: International Committee for Future Accelerators, `http://www.fnal.gov/directorate/icfa/`.

[39] ILC GDE: The ILC Global Design Efford Committee, `http://www.linearcollider.org/cms/?pid=1000014`.

[40] The ILC: By the numbers, `http://www.linearcollider.org/pdf/ilcbynumbers.pdf`.

[41] J. Mnich, *Detector for a Linear Collider*, Nucl. Phys. Proc. Suppl. **125**, 245 (2003).

[42] ALEPH Collaboration, D. Buskulic et al., *Performance of the ALEPH detector at LEP*, Nucl. Instrum. Meth. **A360**, 481 (1995).

[43] V. L. Morgunov, *Energy-flow method for multi-jet effective mass reconstruction in the highly granulated TESLA calorimeter*, Prepared for APS / DPF / DPB Summer Study on the Future of Particle Physics (Snowmass 2001), Snowmass, Colorado, 30 Jun - 21 Jul 2001.

[44] M. Thomson, *Particle flow calorimetry*, J. Phys. Conf. Ser. **110**, 092032 (2008).

[45] OPAL Collaboration, G. Abbiendi et al., *Scaling violations of quark and gluon jet fragmentation functions in e+ e- annihilations at* $\sqrt{s}$ *= 91.2-GeV and 183-GeV - 209-GeV*, Eur. Phys. J. **C37**, 25 (2004), arXiv:hep-ex/0404026.

[46] E. Devetak, *Determination of Wtb anomalous coupling at the ILC*, (2008), arXiv:hep-ex/08104831.

[47] ILC: International Large Detector, `http://www.ilcild.org`.

[48] LDC Large Detector Concept, `http://www.ilcldc.org`.

[49] GLD: Global Large Detector, `http://ilcphys.kek.jp/gld/`.

[50] SiD: Silicon Detector Design Study, `http://www-sid.slac.stanford.edu/`.

[51] 4th: The 4th detector concept, `http://www.4thconcept.org`.

[52] C. Lacosta, *Detectors for the ILC*, Talk given at the XXXV International Meeting On Fundamental Physics, Santiago de Compostela, Spain, May 2007.

[53] A. Streun, *Practical Guidelines for Lattice Design*, PSI Internal Note, SLS-TME-TA-1999-0014. (1999)

[54] A. W. Chao, and M. Tigner, *Handbook of Accelerator Physics and Engineering*, Singapore: World Scientific, (1999).

[55] D. Schulte, *Study of electromagnetic and hadronic background in the interaction region of the TESLA Collider*, PhD thesis, University of Hamburg, (1996), DESY-TESLA-97-08.

[56] OPAL Collaboration, G. Abbiendi et al., *Precision luminosity for Z0 line-shape measurements with a silicon-tungsten calorimeter*, Eur. Phys. J. **C14**, 373 (2000), arXiv:hep-ex/9910066.

[57] I. Sadeh, *The Luminosity Calorimeter*, Talk given at the ECFA 2008 Workshop.

[58] M. Slater et al., *Cavity BPM System Tests for the ILC Energy Spectrometer*, Nucl. Instrum. Meth. **A 592**, 201 (2008).

[59] S. Walston. et al., *Performance of a High Resolution Cavity Beam Position Monitor System*, Nucl. Instrum. Meth. **A 578**, 1 (2007).

[60] S. Boogert, M. Hildreth, D. Kfer, J. List, K. Mönig, K.C. Moffeit, G. Moortgat-Pick, S. Riemann, H.J. Schreiber, P. Schler, E. Torrence, M. Woods, *Polarimeters and Energy Spectrometers for the ILC Beam Delivery System*, (2009), arXiv:inst-det/09040122.

[61] N. Muchnoi, H. J. Schreiber, and M. Viti, *ILC Beam Energy Measurement by means of Laser Compton Backscattering*, (2008), arXiv:inst-det/08120925.

[62] K. Hiller, H. J. Schreiber, R. Makarov, E. Syresin, and B. Zalikhanov, *ILC beam energy measurement based on synchrotron radiation from a magnetic spectrometer*, Nucl. Instrum. Meth. **A580**, 1191 (2007).

[63] A. Ghalumyan, *Experiment Proposal for E_b Measurement using the Resonance Absorption Method* Talk at 2008 Workshop on Polarization and Beam Energy Measurements at the ILC. DESY Zeuthen, (2008)

[64] M. Skrzypek and S. Jadach, *Exact and approximate solutions for the electron nonsinglet structure function in QED*, Z. Phys. **C49**, 577 (1991).

[65] P. Chen, *Beamstrahlung and the QED, QCD backgrounds in linear colliders*, Presented at 9th International Workshop on Photon-Photon Collisions (PHOTON-PHOTON '92), San Diego, CA, 22-26 Mar 1992.

[66] M. E. Peskin, *Pandora: An object-oriented event generator for linear collider physics*, (1999), arXiv:hep-ph/9910519.

[67] E. A. Kuraev and V. S. Fadin, *On Radiative Corrections to e+ e- Single Photon Annihilation at High-Energy*, Sov. J. Nucl. Phys. **41**, 466 (1985).

[68] D. Schulte et al., *GUINEA PIG++ : An Upgraded Version of the Linear Collider Beam Beam Interaction Simulation Code GUINEA PIG*, Particle Accelerator Conference PAC07 25-29 Jun 2007, Albuquerque, New Mexico.

[69] T. Ohl, *CIRCE version 1.0: Beam spectra for simulating linear collider physics*, Comput. Phys. Commun. **101**, 269 (1997), arXiv:hep-ph/9607454.

[70] W. Verkerke and D. Kirkby, *The RooFit toolkit for data modeling*, (2003), arXiv:physics/0306116.

[71] B. Gough, *GNU Scientific Library Reference Manual - 2nd Edition*, Network Theory Ltd., (2003).

[72] M. Frary and D. Miller, *Monitoring the Luminosity Spectrum*, DESY 92-123A 379-391. (1992)

[73] S. Jadach, W. Placzek, and B. F. L. Ward, *BHWIDE 1.00: O(alpha) YFS exponentiated Monte Carlo for Bhabha scattering at wide angles for LEP1/SLC and LEP2*, Phys. Lett. **B390**, 298 (1997), arXiv:hep-ph/9608412.

[74] T. Behnke, S. Bertolucci, R. D. Heuer, and R. Settles (editors), *TESLA: The superconducting electron positron linear collider with an integrated X-ray laser laboratory. Technical design report. Pt. 4: A detector for TESLA*, DESY-01-011. (2001)

[75] The ILD Detector Concept, `http://www.ilcild.org/`.

[76] K. Mönig, *Measurement of the differential luminosity using Bhabha events in the forward tracking region at TESLA*, LC-PHSM-2000-060. (2000)

[77] C. Rimbault, P. Bambade, K. Monig, and D. Schulte, *Impact of beam-beam effects on precision luminosity measurements at the ILC*, JINST **2**, P09001 (2007).

[78] M. J. Strassler and M. E. Peskin, *Threshold production of heavy top quarks: QCD and the Higgs boson*, Phys. Rev. D **43**, 1500 (1991).

[79] V. S. Fadin and V. A. Khoze, *Threshold Behavior of Heavy Top Production in e+ e- Collisions*, JETP Lett. **46**, 525 (1987).

[80] M. Jezabek, J. H. Kuhn, and T. Teubner, *Momentum distributions in t anti-t production and decay near threshold*, Z. Phys. **C56**, 653 (1992).

[81] A. H. Hoang, A. V. Manohar, I. W. Stewart, and T. Teubner, *Renormalization-Group Improved Calculation of Top-Quark Production Near Threshold*, Phys. Rev. Lett. **86**, 1951 (2001).

[82] A. H. Hoang, A. V. Manohar, I. W. Stewart, and T. Teubner, *Threshold $t\bar{t}$ cross section at next-to-next-to-leading logarithmic order*, Phys. Rev. D **65**, 014014 (2001).

[83] W. Caswell and G. Lepage, Phys. Lett. **B167**, 437 (1986).

[84] G.T. Bodwin, E. Braaten and G. Lepage, Phys. Rev. **D51**, 1125 (1995).

[85] A. S. Kronfeld, *The perturbative pole mass in QCD*, Phys. Rev. **D58**, 051501 (1998), arXiv:hep-ph/9805215.

[86] R. Tarrach, *The Renormalization of FF*, Nucl. Phys. **B196**, 45 (1982).

[87] N. Gray, D. J. Broadhurst, W. Grafe, and K. Schilcher, *Three Loop Relation of Quark (modified) MS and Pole Masses*, Z. Phys. **C48**, 673 (1990).

[88] K. G. Chetyrkin and M. Steinhauser, *The relation between the MS-bar and the on-shell quark mass at order $\alpha(s)^3$*, Nucl. Phys. **B573**, 617 (2000), arXivhep-ph/9911434.

[89] K. Melnikov and T. v. Ritbergen, *The three-loop relation between the MS-bar and the pole quark masses*, Phys. Lett. **B482**, 99 (2000), arXiv:hep-ph/9912391.

[90] F. James, *Monte Carlo theory and practice*, Rep. Prog. Phys. **43**, 1146 (1980).

[91] M. Seymour, *Predictions for Higgs and Electroweak Boson Production*, PhD thesis, University of Cambridge, RALT-142. (1992).

[92] D. Knuth, *The Art of Computer Programming*, Volume 2, Reading, Mass.: Addison-Wesley, (1969).

[93] M. Matsumoto and T. Nishimura, *Mersenne Twistor: A 623-diminsionally equidistributed uniform pseudorandom number generator*, ACM Transactions on Modeling and Computer Simulation **8**, 3 (1998).

[94] T. Sjostrand, S. Mrenna, and P. Skands, *PYTHIA 6.4 physics and manual*, JHEP **05**, 026 (2006), arXiv:hep-ph/0603175.

[95] G. Corcella et al., *HERWIG 6.5 release note*, (2002), arXiv:hep-ph/0210213.

[96] S. Jadach and P. Sawicki, *mFOAM-1.02: A compact version of the cellular event generator FOAM*, Comput. Phys. Commun. **177**, 441 (2007), arXiv:physics/0506084.

[97] B. F. L. Ward, S. Jadach, and Z. Was, Precision calculation for e+ e- → 2f: The KK MC project, Nucl. Phys. Proc. Suppl. **116**, 73 (2003), arXiv:hep-ph/0211132.

[98] R. Brun and F. Rademakers, *ROOT: An object oriented data analysis framework*, Nucl. Instrum. Meth. **A389**, 81 (1997).

[99] S. Kasselmann, *Top Quark Mass Measurement in the Lepton+Jets Channel using Full Simulation of the CMS Detector*, PhD thesis, RWTH Aachen, (2007),

[100] R. Harlander, M. Jezabek, J. H. Kuhn, and M. Peter, *Top quark polarization in polarized e+ e- annihilation near threshold*, Z. Phys. **C73**, 477 (1997), arXiv:hep-ph/9604328.